IceCube-Gen2 - The Next Generation Neutrino Observatory at the South Pole: Contributions to ICRC 2015

Collaboration, TI-G; Aartsen, MG; Abraham, K; Ackermann, M; Adams, J; Aguilar, JA; Ahlers, M; Ahrens, M; Altmann, D; Anderson, T; Ansseau, I; Anton, G; Archinger, M; Arguelles, C; Arlen, TC; Auffenberg, J; Axani, S; Bai, X; Bartos, I; Barwick, SW; Baum, V; Bay, R; Beatty, JJ; Tjus, JB; Becker, K-H; Beiser, E; BenZvi, S; Berghaus, P; Berley, D; Bernardini, E; Bernhard, A; Besson, DZ; Binder, G; Bindig, D; Bissok, M; Blaufuss, E; Blumenthal, J; Boersma, DJ; Bohm, C; Börner, M; Bos, F; Bose, D; Böser, S; Botner, O; Braun, J; Brayeur, L; Bretz, H-P; Buzinsky, N; Casey, J; Casier, M; Cheung, E; Chirkin, D; Christov, A; Clark, K; Classen, L; Coenders, S; Collin, GH; Conrad, JM; Cowen, DF; Silva, AHC; Daughhetee, J; Davis, JC; Day, M; André, JPAMD; Clercq, CD; Rosendo, EDP; Dembinski, H; Ridder, SD; Desiati, P; Vries, KDD; Wasseige, GD; With, MD; DeYoung, T; Diaz-Vélez, JC; Lorenzo, VD; Dumm, JP; Dunkman, M; Eagan, R; Eberhardt, B; Ehrhardt, T; Eichmann, B; Euler, S; Evans, JJ; Evenson, PA; Fadiran, O; Fahey, S; Fazely, AR; Fedynitch, A; Feintzeig, J; Felde, J; Filimonov, K; Finley, C; Fischer-Wasels, T; Flis, S; Fösig, C-C; Fuchs, T; Gaisser, TK; Gaior, R; Gallagher, J; Gerhardt, L; Ghorbani, K; Gier, D; Gladstone, L; Glagla, M; Glüsenkamp, T; Goldschmidt, A; Golup, G; Gonzalez, JG; Góra, D; Grant, D; Groh, JC; Groß, A; Ha, C; Haack, C; Ismail, AH; Hallgren, A; Halzen, F; Hansmann, B; Hanson, K; Haugen, J; Hebecker, D; Heereman, D; Helbing, K; Hellauer, R; Hellwig, D; Hickford, S; Hignight, J; Hill, GC; Hoffman, KD; Hoffmann, R; Holzapfel, K; Homeier, A; Hoshina, K; Huang, F; Huber, M; Huelsnitz, W; Hulth, PO; Hultqvist, K; In, S; Ishihara, A; Jacobi, E; Japaridze, GS; Jero, K; Jones, BJP; Jurkovic, M; Kalekin, O; Kaminsky, B; Kappes, A; Karg, T; Karle, A; Katori, T; Katz, U; Kauer, M; Keivani, A; Kelley, JL; Kemp, J; Kheirandish, A; Kiryluk, J; Kläs, J; Klein, SR; Kohnen, G; Koirala, R; Kolanoski, H; Konietz, R; Koob, A; Köpke, L; Kopper, C; Kopper, S; Koskinen, DJ; Kowalski, M; Krauss, CB; Krings, K; Kroll, G; Kroll, M; Kunnen, J; Kurahashi, N; Kuwabara, T; Labare, M; Lanfranchi, JL; Larson, MJ; Lesiak-Bzdak, M; Leuermann, M; Leuner, J; LoSecco, J; Lu, L; Lünemann, J; Madsen, J; Maggi, G; Mahn, KBM; Marka, S; Marka, Z; Maruyama, R; Mase, K; Matis, HS; Maunu, R; McNally, F; Meagher, K; Medici, M; Meli, A; Menne, T; Merino, G; Meures, T; Miarecki, S; Middell, E; Middlemas, E; Mohrmann, L; Montaruli, T; Moore, RW; Morse, R; Nahnhauer, R; Naumann, U; Neer, G; Niederhausen, H; Nowicki, SC; Nygren, DR; Obertacke, A; Olivas, A; Omairat, A; O'Murchadha, A; Palazzo, A; Palczewski, T; Pandya, H; Paul, L; Pepper, JA; Heros, CPDL; Petersen, TC; Pfendner, C; Pieloth, D; Pinat, E; Pinfold, JL; Posselt, J; Price, PB; Przybylski, GT; Pütz, J; Quinnan, M; Raab, C; Rädel, L; Rameez, M; Rawlins, K; Reimann, R; Relich, M; Resconi, E; Rhode, W; Richman, M; Richter, S; Riedel, B; Robertson, S; Rongen, M; Rott, C; Ruhe, T; Ryckbosch, D; Saba, SM; Sabbatini, L; Sander, H-G; Sandrock, A; Sandroos, J; Sandstrom, P; Sarkar, S; Schatto, K; Scheriau, F; Schimp, M; Schmidt, T; Schmitz, M; Schoenen, S; Schöneberg, S; Schönwald, A; Schulte, L; Seckel,

PROCEEDINGS OF SCIENCE

IceCube-Gen2 – The Next Generation Neutrino Observatory at the South Pole

Contributions to ICRC 2015

The IceCube-Gen2 Collaboration

Contents

The 34th International Cosmic Ray Conference,
30 July- 6 August, 2015
The Hague, The Netherlands

IceCube-Gen2 Collaboration Member List

M. G. Aartsen[2], K. Abraham[35], M. Ackermann[55], J. Adams[16], J. A. Aguilar[12], M. Ahlers[31], M. Ahrens[45], D. Altmann[24], T. Anderson[52], I. Ansseau[12], G. Anton[24], M. Archinger[32], C. Arguelles[31], T. C. Arlen[52], J. Auffenberg[1], S. Axani[23], X. Bai[43], I. Bartos[39], S. W. Barwick[27], V. Baum[32], R. Bay[7], J. J. Beatty[18,19], J. Becker Tjus[10], K.-H. Becker[54], E. Beiser[31], S. BenZvi[31], P. Berghaus[55], D. Berley[17], E. Bernardini[55], A. Bernhard[35], D. Z. Besson[28], G. Binder[8,7], D. Bindig[54], M. Bissok[1], E. Blaufuss[17], J. Blumenthal[1], D. J. Boersma[53], C. Bohm[45], M. Börner[21], F. Bos[10], D. Bose[47], S. Böser[32], O. Botner[53], J. Braun[31], L. Brayeur[13], H.-P. Bretz[55], N. Buzinsky[23], J. Casey[5], M. Casier[13], E. Cheung[17], D. Chirkin[31], A. Christov[25], K. Clark[49], L. Classen[24], S. Coenders[35], G. H. Collin[14], J. M. Conrad[14], D. F. Cowen[52,51], A. H. Cruz Silva[55], J. Daughhetee[5], J. C. Davis[18], M. Day[31], J. P. A. M. de André[22], C. De Clercq[13], E. del Pino Rosendo[32], H. Dembinski[37], S. De Ridder[26], P. Desiati[31], K. D. de Vries[13], G. de Wasseige[13], M. de With[9], T. DeYoung[22], J. C. Díaz-Vélez[31], V. di Lorenzo[32], J. P. Dumm[45], M. Dunkman[52], R. Eagan[52], B. Eberhardt[32], T. Ehrhardt[32], B. Eichmann[10], S. Euler[53], J. J. Evans[33], P. A. Evenson[37], O. Fadiran[31], S. Fahey[31], A. R. Fazely[6], A. Fedynitch[10], J. Feintzeig[31], J. Felde[17], K. Filimonov[7], C. Finley[45], T. Fischer-Wasels[54], S. Flis[45], C.-C. Fösig[32], T. Fuchs[21], T. K. Gaisser[37], R. Gaior[15], J. Gallagher[30], L. Gerhardt[8,7], K. Ghorbani[31], D. Gier[1], L. Gladstone[31], M. Glagla[1], T. Glüsenkamp[55], A. Goldschmidt[8], G. Golup[13], J. G. Gonzalez[37], D. Góra[55], D. Grant[23], J. C. Groh[52], A. Groß[35], C. Ha[8,7], C. Haack[1], A. Haj Ismail[26], A. Hallgren[53], F. Halzen[31], B. Hansmann[1], K. Hanson[31], J. Haugen[31], D. Hebecker[9], D. Heereman[12], K. Helbing[54], R. Hellauer[17], D. Hellwig[1], S. Hickford[54], J. Hignight[22], G. C. Hill[2], K. D. Hoffman[17], R. Hoffmann[54], K. Holzapfel[35], A. Homeier[11], K. Hoshina[31,48], F. Huang[52], M. Huber[35], W. Huelsnitz[17], P. O. Hulth[45], K. Hultqvist[45], S. In[47], A. Ishihara[15], E. Jacobi[55], G. S. Japaridze[4], K. Jero[31], B. J. P. Jones[14], M. Jurkovic[35], O. Kalekin[24], B. Kaminsky[55], A. Kappes[24], T. Karg[55], A. Karle[31], T. Katori[29], U. Katz[24], M. Kauer[31,38], A. Keivani[52], J. L. Kelley[31], J. Kemp[1], A. Kheirandish[31], J. Kiryluk[46], J. Kläs[54], S. R. Klein[8,7], G. Kohnen[34], R. Koirala[37], H. Kolanoski[9], R. Konietz[1], A. Koob[1], L. Köpke[32], C. Kopper[23], S. Kopper[54], D. J. Koskinen[20], M. Kowalski[9,55], C. B. Krauss[23], K. Krings[35], G. Kroll[32], M. Kroll[10], J. Kunnen[13], N. Kurahashi[42], T. Kuwabara[15], M. Labare[26], J. L. Lanfranchi[52], M. J. Larson[20], M. Lesiak-Bzdak[46], M. Leuermann[1], J. Leuner[1], J. LoSecco[40], L. Lu[15], J. Lünemann[13], J. Madsen[44], G. Maggi[13], K. B. M. Mahn[22], S. Marka[39], Z. Marka[39], R. Maruyama[38], K. Mase[15], H. S. Matis[8], R. Maunu[17], F. McNally[31], K. Meagher[12], M. Medici[20], A. Meli[26], T. Menne[21], G. Merino[31], T. Meures[12], S. Miarecki[8,7], E. Middell[55], E. Middlemas[31], L. Mohrmann[55], T. Montaruli[25], R. W. Moore[23], R. Morse[31], R. Nahnhauer[55], U. Naumann[54], G. Neer[22], H. Niederhausen[46], S. C. Nowicki[23], D. R. Nygren[8], A. Obertacke[54], A. Olivas[17], A. Omairat[54], A. O'Murchadha[12], A. Palazzo[36], T. Palczewski[50], H. Pandya[37], L. Paul[1], J. A. Pepper[50], C. Pérez de los Heros[53], T. C. Petersen[20], C. Pfendner[18], D. Pieloth[21], E. Pinat[12], J. L. Pinfold[23], J. Posselt[54], P. B. Price[7], G. T. Przybylski[8], J. Pütz[1], M. Quinnan[52], C. Raab[12], L. Rädel[1], M. Rameez[25], K. Rawlins[3], R. Reimann[1], M. Relich[15], E. Resconi[35], W. Rhode[21], M. Richman[42], S. Richter[31], B. Riedel[23], S. Robertson[2], M. Rongen[1], C. Rott[47], T. Ruhe[21], D. Ryckbosch[26], S. M. Saba[10], L. Sabbatini[31], H.-G. Sander[32], A. Sandrock[21], J. Sandroos[32], P. Sandstrom[31], S. Sarkar[20,41], K. Schatto[32], F. Scheriau[21], M. Schimp[1], T. Schmidt[17], M. Schmitz[21], S. Schoenen[1], S. Schöneberg[10], A. Schönwald[55], L. Schulte[11], D. Seckel[37], S. Seunarine[44], M. H. Shaevitz[39], R. Shanidze[55], M. W. E. Smith[52], D. Soldin[54], S. Söldner-Rembold[33], M. Song[17], G. M. Spiczak[44], C. Spiering[55], M. Stahlberg[1], M. Stamatikos[18,a],

T. Stanev[37], N. A. Stanisha[52], A. Stasik[55], T. Stezelberger[8], R. G. Stokstad[8], A. Stößl[55], R. Ström[53], N. L. Strotjohann[55], G. W. Sullivan[17], M. Sutherland[18], H. Taavola[53], I. Taboada[5], A. Taketa[48], H. K. M. Tanaka[48], S. Ter-Antonyan[6], A. Terliuk[55], G. Tešić[52], S. Tilav[37], P. A. Toale[50], M. N. Tobin[31], S. Toscano[13], D. Tosi[31], M. Tselengidou[24], A. Turcati[35], E. Unger[53], M. Usner[55], S. Vallecorsa[25], J. Vandenbroucke[31], N. van Eijndhoven[13], S. Vanheule[26], J. van Santen[31], J. Veenkamp[35], M. Vehring[1], M. Voge[11], M. Vraeghe[26], C. Walck[45], A. Wallace[2], M. Wallraff[1], N. Wandkowsky[31], Ch. Weaver[23], C. Wendt[31], S. Westerhoff[31], B. J. Whelan[2], N. Whitehorn[31], C. Wichary[1], K. Wiebe[32], C. H. Wiebusch[1], L. Wille[31], D. R. Williams[50], H. Wissing[17], M. Wolf[45], T. R. Wood[23], K. Woschnagg[7], S. Wren[33], D. L. Xu[50], X. W. Xu[6], Y. Xu[46], J. P. Yanez[55], G. Yodh[27], S. Yoshida[15], M. Zoll[45]

[1]III. Physikalisches Institut, RWTH Aachen University, D-52056 Aachen, Germany
[2]Department of Physics, University of Adelaide, Adelaide, 5005, Australia
[3]Dept. of Physics and Astronomy, University of Alaska Anchorage, 3211 Providence Dr., Anchorage, AK 99508, USA
[4]CTSPS, Clark-Atlanta University, Atlanta, GA 30314, USA
[5]School of Physics and Center for Relativistic Astrophysics, Georgia Institute of Technology, Atlanta, GA 30332, USA
[6]Dept. of Physics, Southern University, Baton Rouge, LA 70813, USA
[7]Dept. of Physics, University of California, Berkeley, CA 94720, USA
[8]Lawrence Berkeley National Laboratory, Berkeley, CA 94720, USA
[9]Institut für Physik, Humboldt-Universität zu Berlin, D-12489 Berlin, Germany
[10]Fakultät für Physik & Astronomie, Ruhr-Universität Bochum, D-44780 Bochum, Germany
[11]Physikalisches Institut, Universität Bonn, Nussallee 12, D-53115 Bonn, Germany
[12]Université Libre de Bruxelles, Science Faculty CP230, B-1050 Brussels, Belgium
[13]Vrije Universiteit Brussel, Dienst ELEM, B-1050 Brussels, Belgium
[14]Dept. of Physics, Massachusetts Institute of Technology, Cambridge, MA 02139, USA
[15]Dept. of Physics, Chiba University, Chiba 263-8522, Japan
[16]Dept. of Physics and Astronomy, University of Canterbury, Private Bag 4800, Christchurch, New Zealand
[17]Dept. of Physics, University of Maryland, College Park, MD 20742, USA
[18]Dept. of Physics and Center for Cosmology and Astro-Particle Physics, Ohio State University, Columbus, OH 43210, USA
[19]Dept. of Astronomy, Ohio State University, Columbus, OH 43210, USA
[20]Niels Bohr Institute, University of Copenhagen, DK-2100 Copenhagen, Denmark
[21]Dept. of Physics, TU Dortmund University, D-44221 Dortmund, Germany
[22]Dept. of Physics and Astronomy, Michigan State University, East Lansing, MI 48824, USA
[23]Dept. of Physics, University of Alberta, Edmonton, Alberta, Canada T6G 2E1
[24]Erlangen Centre for Astroparticle Physics, Friedrich-Alexander-Universität Erlangen-Nürnberg, D-91058 Erlangen, Germany
[25]Département de physique nucléaire et corpusculaire, Université de Genève, CH-1211 Genève, Switzerland
[26]Dept. of Physics and Astronomy, University of Gent, B-9000 Gent, Belgium
[27]Dept. of Physics and Astronomy, University of California, Irvine, CA 92697, USA
[28]Dept. of Physics and Astronomy, University of Kansas, Lawrence, KS 66045, USA

[29]School of Physics and Astronomy, Queen Mary University of London, London E1 4NS, United Kingdom
[30]Dept. of Astronomy, University of Wisconsin, Madison, WI 53706, USA
[31]Dept. of Physics and Wisconsin IceCube Particle Astrophysics Center, University of Wisconsin, Madison, WI 53706, USA
[32]Institute of Physics, University of Mainz, Staudinger Weg 7, D-55099 Mainz, Germany
[33]School of Physics and Astronomy, The University of Manchester, Oxford Road, Manchester, M13 9PL, United Kingdom
[34]Université de Mons, 7000 Mons, Belgium
[35]Technische Universität München, D-85748 Garching, Germany
[36]Max-Planck-Institut für Physik (Werner Heisenberg Institut), Föhringer Ring 6, D-80805 München, Germany
[37]Bartol Research Institute and Dept. of Physics and Astronomy, University of Delaware, Newark, DE 19716, USA
[38]Dept. of Physics, Yale University, New Haven, CT 06520, USA
[39]Columbia Astrophysics and Nevis Laboratories, Columbia University, New York, NY 10027, USA
[40]Dept. of Physics, University of Notre Dame du Lac, 225 Nieuwland Science Hall, Notre Dame, IN 46556-5670, USA
[41]Dept. of Physics, University of Oxford, 1 Keble Road, Oxford OX1 3NP, UK
[42]Dept. of Physics, Drexel University, 3141 Chestnut Street, Philadelphia, PA 19104, USA
[43]Physics Department, South Dakota School of Mines and Technology, Rapid City, SD 57701, USA
[44]Dept. of Physics, University of Wisconsin, River Falls, WI 54022, USA
[45]Oskar Klein Centre and Dept. of Physics, Stockholm University, SE-10691 Stockholm, Sweden
[46]Dept. of Physics and Astronomy, Stony Brook University, Stony Brook, NY 11794-3800, USA
[47]Dept. of Physics, Sungkyunkwan University, Suwon 440-746, Korea
[48]Earthquake Research Institute, University of Tokyo, Bunkyo, Tokyo 113-0032, Japan
[49]Dept. of Physics, University of Toronto, Toronto, Ontario, Canada, M5S 1A7
[50]Dept. of Physics and Astronomy, University of Alabama, Tuscaloosa, AL 35487, USA
[51]Dept. of Astronomy and Astrophysics, Pennsylvania State University, University Park, PA 16802, USA
[52]Dept. of Physics, Pennsylvania State University, University Park, PA 16802, USA
[53]Dept. of Physics and Astronomy, Uppsala University, Box 516, S-75120 Uppsala, Sweden
[54]Dept. of Physics, University of Wuppertal, D-42119 Wuppertal, Germany
[55]DESY, D-15735 Zeuthen, Germany
[a]NASA Goddard Space Flight Center, Greenbelt, MD 20771, USA

Acknowledgment: We acknowledge the support from the following agencies: U.S. National Science Foundation-Office of Polar Programs, U.S. National Science Foundation-Physics Division, University of Wisconsin Alumni Research Foundation, the Grid Laboratory Of Wisconsin (GLOW) grid infrastructure at the University of Wisconsin - Madison, the Open Science Grid (OSG) grid infrastructure; U.S. Department of Energy, and National Energy Research Scientific Computing Center, the Louisiana Optical Network Initiative (LONI) grid computing resources; Natural Sciences and Engineering Research Council of Canada, WestGrid and Compute/Calcul Canada; Swedish Research Council, Swedish Polar Research Secretariat, Swedish National Infrastructure for Computing (SNIC), and Knut and Alice Wallenberg Foundation, Sweden; German Ministry for Education and Research (BMBF), Deutsche Forschungsgemeinschaft (DFG), Helmholtz Alliance for Astroparticle Physics (HAP), Research Department of Plasmas with Complex Interactions (Bochum), Germany; Fund for Scientific Research (FNRS-FWO), FWO Odysseus programme, Flanders Institute to encourage scientific and technological research in industry (IWT), Belgian Federal Science Policy Office (Belspo); University of Oxford, United Kingdom; Marsden Fund, New Zealand; Australian Research Council; Japan Society for Promotion of Science (JSPS); the Swiss National Science Foundation (SNSF), Switzerland; National Research Foundation of Korea (NRF); Danish National Research Foundation, Denmark (DNRF)

PROCEEDINGS OF SCIENCE

Cosmic Ray Science Potential for an Extended Surface array at the IceCube Observatory

The IceCube-Gen2 Collaboration[1],

[1] *http://icecube.wisc.edu/collaboration/authors/icrc15_gen2*

E-mail: seckel@bartol.udel.edu

IceTop is the 1 km^2 surface array of the IceCube Neutrino Observatory. Measurements of ground level particles by IceTop have been used for high resolution measurements of the cosmic ray spectrum for energies of 2-500 PeV. Composition has been studied by considering coincident measurements of TeV muon bundles in the 2 km deep IceCube neutrino detector. Including IceTop data for GeV muons may reduce uncertainties inherent to hadronic interaction models; however, all three parts of this program are somewhat limited by the size of IceTop. We explore the potential for *IceCube-Gen2* with surface components (*IceTop-2*, "veto") to improve the cosmic ray science program. The increased area would permit a factor of ~ 3 increase in energy range for the spectral measurement, a factor of 50 increase in coincident data, and enable lateral and production depth muon measurements for every event.

Corresponding authors: David Seckel[1]*,

[1] *Department of Physics and Astonomy, University of Delaware, Newark DE 19716, USA*

The 34th International Cosmic Ray Conference,
30 July- 6 August, 2015
The Hague, The Netherlands

*Speaker.

IceCube [1], IceTop [2], and cosmic rays. Although best known for its contributions to neutrino physics, IceCube is also a significant cosmic ray observatory. IceCube has produced a high resolution cosmic ray energy spectrum [3, 4] based on data purely from IceTop, the surface array directly above the main in-ice neutrino detector (Fig. 1). By including in-ice data characterizing the muon bundles associated with coincident air shower events, IceCube is providing a unique composition measurement [3, 5] between the knee and the ankle of the cosmic ray spectrum. We are studying the ability to separate the surface response into electromagnetic (*em*) and muonic components [6, 7], which we will use to produce an independent proxy for the mass of the cosmic ray primary responsible for an air shower. These analyses feed into a community effort to understand cosmic rays in the range $10^{16} - 10^{18}$ eV, where there is expected to be a transition from galactic to extragalactic origins [8]. All three efforts are somewhat limited by the 1 km^2 extent of the IceTop array, and so the upper end of the transition is not well covered, especially with regards to composition.

At the same time, IceCube has completed one of its main science goals by demonstrating the existence of an astrophysical neutrino flux [9, 10]. This result is one of the driving considerations for *IceCube-Gen2* [11, 12], a second generation detector at South Pole. Gen2 is planned on the same principles as IceCube but with roughly an order of magnitude better sensitivity for achieving key science goals related to the high energy astrophysical neutrino flux. This increase derives primarily from larger area and an enhanced surface veto [13, 14] to increase the significance of astrophysical neutrino events relative to a background of air shower induced muons and neutrinos.

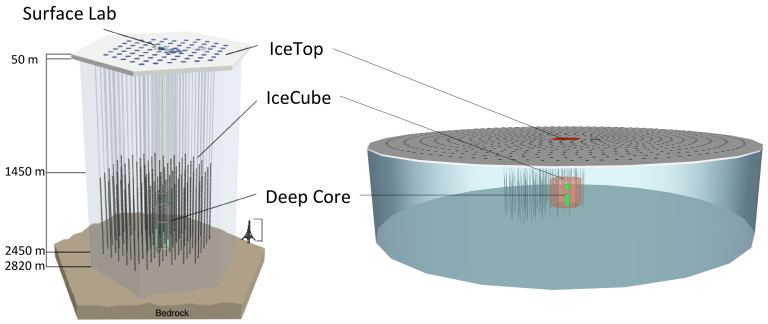

Figure 1: Left: IceCube neutrino observatory. Right: *IceCube-Gen2* with extended version of surface veto.

The increase in area and a dedicated veto array provide an opportunity to improve existing analyses at the higher energies. A nominal plan is to deploy at each string a surface station capable of good timing and charge measurements with high dynamic range to provide a quality reconstruction of the size and geometry of the air shower event. As part of Gen2 this would permit extending both the surface only analysis and the coincident in-ice/surface analysis to above 1 EeV in energy. The improvement in the coincident analysis is most significant, roughly a factor of 50 by simple geometry considerations. In addition, a veto array could permit an unprecedented measurement of the peripheral muons in an air shower, complementing the combined in-ice/surface measurement of cosmic ray composition.

IceCube cosmic ray science program. IceCube's cosmic ray program includes two distinct determinations of the all-particle cosmic ray energy spectrum, both based on 3 years of data. The first,

utilizing just IceTop data, is shown in Fig. 2 along with data from other experiments [15] spanning the energy range from the knee to above the ankle. It is notable that the IceTop result is a relatively high resolution spectrum compared to other experiments at energies below ~ 300 PeV, reflecting superior statistics. The gray band showing systematic uncertainty mostly affects the overall normalization (see [3, 4]). The IceTop result shows clearly that the region from the knee to the ankle cannot be described by a simple power law. At higher energies, there is some tension between Auger and TA, but present IceTop statistics are not sufficient to provide any insight. In fact, there are 18 events with energies above $10^{9.1}$ GeV which are not shown due to an increase in systematic uncertainty as large showers saturate a significant fraction of the array, even on kilometer scales.

The IceTop only analysis assumes a specific energy dependent composition in deriving the spectrum, and that assumption is included in the systematic uncertainties. The second (coincident) analysis relaxes this assumption and uses in-ice data to infer composition. Muon bundles produced in the air shower event penetrate to the in-ice array. Since heavier nuclei produce more muons, the in-ice signal is a proxy for the mass of the cosmic ray primary. The analysis utilizes a neural net to produce a weight for each event to arise from one of four nuclear mass groups. By combining the weights from all particles, a composition is determined as a function of primary energy. The result is shown in Fig. 3. In each panel the all-particle spectrum is shown in black above the partial spectrum for a particular mass group. The all-particle energy spectrum is in good agreement with that derived from IceTop alone. The light species dominate at the knee, and composition gets heavier with increasing energy, but detailed interpretation is pending a fuller discussion of systematics, including calibration of the response to in-ice muon bundles and variations due to different hadronic interaction models [3]. The coincident analysis has a restricted energy range compared to the IceTop only analysis, with statistics limited by the coincident geometry which reduces the sky coverage from $\Omega_{top} = 1.26$ sr to $\Omega_{co} \sim 0.15$ sr.

In principle, IceTop can also be used to measure the muon content of air showers [6, 7]; however, it is difficult to observe individual muons in the inner part of the air shower where the *em* part of the shower is intense. At energies above a few PeV, the inner 300 m is not available to muon counting. At higher energies, one must go further out, but a shower which passes the containment cuts is never more than 900 m from the furthest IceTop station. There may be few observable muons with which to build a lateral distribution function (LDF) and characterize the event.

The IceCube cosmic ray program includes several more specialized analyses which would benefit from *IceCube-Gen2*. a) Searching for γ-rays is an extreme form of composition study. Air showers with abnormally low muon content are γ-ray candidates. These may be found within the coincident geometry [16], or as events where the surface muon content is low. Selection criteria may be optimized to look for a diffuse flux, or a source defined by a cluster in sky position and/or time. b) Neutrons are another neutral component of the cosmic ray spectrum, relying on an excess of clustered events for detection [17]. c) Both IceTop and IceCube(in-ice) are used to study anisotropy in different ranges of energy and declination [18, 19, 20].

Improvements with *IceCube-Gen2*. For the present discussion, it is convenient to adopt a baseline configuration for *IceCube-Gen2* that includes an in-ice array and two surface components, which we will refer to as "the veto" and *IceTop-2* (IT2). The in-ice array is nominally taken to be 7 km^2 in area - middle of the range considered in [12]. The veto is designed to enhance Gen2 per-

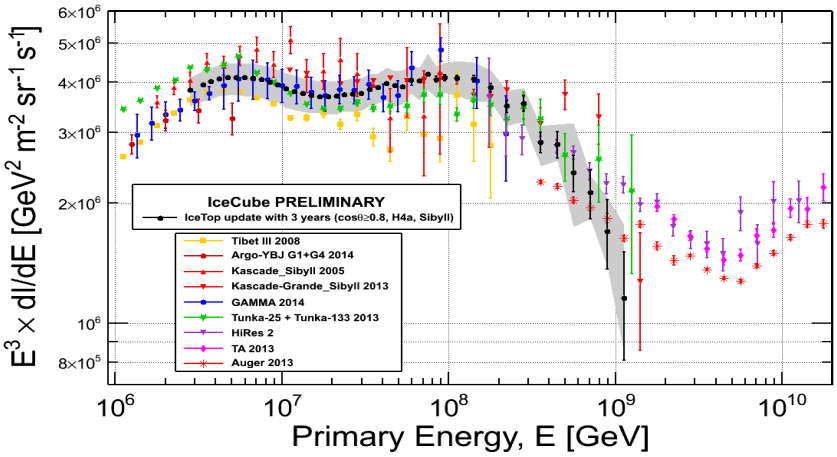

Figure 2: Cosmic ray all-particle energy spectrum using 3 years of IceTop data. Error bars show statistics, gray band shows systematic uncertainty.

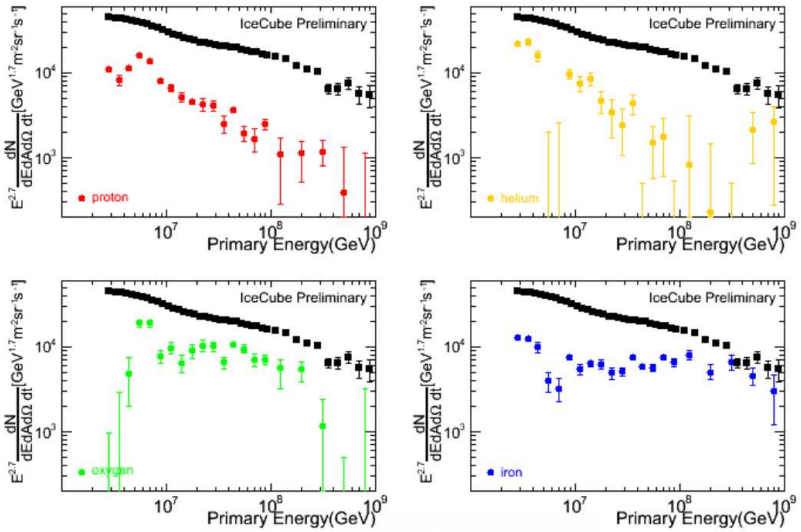

Figure 3: Coincident 3 year spectrum by mass, with all-particles in black. (statistical uncertainties only)

formance with respect to high energy neutrino science. Here, the baseline veto design is taken to be a dense array of particle detectors deployed over the in-ice footprint, although other approaches may be viable [13]. Reasons for this choice are summarized below. Cost efficiency and design goals for the veto may affect its value for measuring properties of extensive air showers. Accordingly, *IceTop-2* would sample the ground level footprint of an air shower with timing and charge resolution sufficient to enable good reconstruction of the size and geometry of the air shower. The baseline for IT2 is to place a station at the head of each string, but we do not specify the instrumentation other than to assume that it can produce reconstructions comparable to those produced by the current IceTop, just at higher energies commensurate with larger spacing between stations.

Improvements due to *IceTop-2*. The improvements are primarily a consequence of increased

size. For current IceTop, the surface only analysis includes a fiducial area of $A = 0.62$ km^2, somewhat smaller than the actual instrumented area of 0.83 km^2, driven largely by the need to reconstruct the core location of the air shower. For the Gen2 estimates we will use a fiducial area of 6 km^2, noting that we expect the edge effects to be reduced and that including data from the veto will improve efficiency. For the surface only analysis, we anticipate an order of magnitude better statistics. Referring to Fig. 2, we expect the scatter of points around 300 PeV to either be smoothed, or to resolve into clear features. Above an EeV, 100 events/yr (10$\times$ IceTop) will accumulate to provide a meaningful overlap with Auger and TA.

The improvements for the coincident analysis are more dramatic. For estimation, we assume the same containment cut for both surface and in-ice arrays. For IceCube, the coincident solid angle is $\Omega_{co} \simeq A/d^2 = 0.15$ sr, where $d = 2$ km is the depth to the center of the in-ice array. This yields an aperture of $\langle A\Omega \rangle = 0.09$ km^2 sr, which can be compared to $\langle A\Omega \rangle = 0.70$ km^2 sr for the surface only analysis, and a ratio of events surviving all cuts of about $N_{top} : N_{co} :: 8 : 1$. For Gen2, the aperture for two disks with $A = 6$ km^2, separated by 2 km, is $\langle A\Omega \rangle = 4.9$ km^2 sr, conservatively ~ 50 times that for current IceCube. It seems likely that galactic and extragalactic sources will have different compositions, either due to intrinsic injection or differential propagation, so increased coincident data informing on the changing composition will be of very high value. Other analyses which rely on coincident data (e.g. γ-ray search) will also benefit from increased sky coverage, including the eastern portion of the galactic plane.

In addition to the overall aperture and statistics, the increase in area from IceTop to IT2 should also improve the efficiency of analysis. At the upper end of IceTop's energy range the electromagnetic footprint saturates large fractions of the detector, increasing the systematic uncertainty and decreasing the effective area. The *em* blanket also obscures muons, making a two component analysis difficult at the highest energies. These effects will be mitigated by the larger area of IT2.

Planning a surface veto for Gen2. The fundamental challenge for IceCube and *IceCube-Gen2* is to detect astrophysical neutrinos against a background of muons and neutrinos produced as a result of cosmic ray interactions in the atmosphere. Upward atmospheric muons are shielded by the Earth, but upward atmospheric neutrinos are an irreducible background for astrophysical neutrinos from the northern sky. The downward case is challenging since the flux of downward atmospheric muons must be eliminated, even at energies of order 100 TeV [13]. However, if all cosmic ray events can be tagged, there is potential to be free not just of muons, but also atmospheric neutrinos. Further, the ice above the in-ice array may be used as a target volume, increasing the rate of track-like events, which have extra value in searches for point sources of astrophysical neutrinos [13].

We consider two veto strategies built around detecting ground level particles. The first focuses on sky coverage, seeking to cover a large fraction of the galaxy including the galactic center. This implies extending the veto to some 6 km, with overall area of 100 km^2. Assuming a minimal tagging threshold of a few PeV, such a veto would detect cosmic rays with energies above 10 PeV. If detections were of sufficient quality all the arguments of the previous paragraphs would apply. A spectrum built only from surface observations would gain by another order of magnitude. Since the in-ice array would remain fixed, the coincident analysis would have a modest gain due to an increase in solid angle as the field of view was extended from zenith angle of 35 deg to 60 deg.

The alternative is to deploy a very dense array over the footprint of Gen2, capable of tagging

cosmic rays with a passing rate of $10^{-4} - 10^{-6}$ [21]. Preliminary estimates are that this could be achieved by an array with a filling factor of 10^{-3}, e.g. roughly 7,000 m^2 of scintillator paddles deployed over the baseline 7 km^2. (For comparison, AMIGA (the Auger in-fill) employs 2000 m^2 of shielded muon counters to provide a filling factor of $\sim 10^{-4}$ [22].) Although sensitive to *em* secondaries, the Gen2 design would be focused on muon detection to ensure veto capability at high inclinations, and to provide stable operation in the presence of snow accumulation on decadal time scales. This alternative is intriguing for cosmic ray science, as it presents the possibility of collecting hundreds of "peripheral" muons, contributing to the composition studies by Gen2.

Contribution of veto array to studies of cosmic ray composition. A counter for muons within an extensive air shower must isolate the muon signal from the electromagnetic part of the shower, either by shielding the muon counter, or by separating the muons from the *em* part of the shower in space and/or time. To this end, we define two interior regions for the muon LDF: a core with lateral separation $r_\perp < 320$ m common to all showers and an "umbra" where the muons are "shadowed" by *em* signals. The core sets the spacing of the veto array, but we define the peripheral muons to be those outside the umbra. The radius of the umbra depends on details of detector design, as well as energy and inclination of the air showers. If the veto elements include shielding, the umbra would have small radius allowing more muons to be counted. If the veto is sensitive to low energy electrons and γs, then the radius of the umbra is increased and surface muon yield decreases. In [6] the muon LDF is studied for IceTop, establishing that the umbra for quasi-vertical showers and IceTop tanks increases from 250 m to 600 m as primary energy increases from 3 to 30 PeV. We are studying the degree of shielding required for a scintillator array to maintain an umbra at 600m, so that $\sim \frac{1}{3}$ the muons can be used to study the hadronic nature of each air shower.

Fig. 4 shows the potential to use these peripheral muons to supplement composition studies, assuming that size and geometry of the air shower are reconstructed in IT2. In the left panel, the muon production is shown for a sample of simulated p and Fe showers. The simplest proxy for separating p and Fe is to count the total number of peripheral muons, multiply by the fractional coverage and compute an expected number of counts. At 30 PeV this corresponds to p/Fe $\simeq 50/80$. Even with fluctuations this provides reasonable separation. In the right panel, a set of 1000 pseudo-observations of 30 PeV events is shown. For each event, shower size is smeared by 15%, setting IT2 resolution to that achieved by IceTop [4]. The expected number of muons with $r_\perp > 600$ m is then sampled to yield a simulated count which is shown on the y-axis. The x-axis shows a comparable quantity for the in-ice bundle. We count all muons with energy $E_\mu > 340/\cos\theta$ GeV, and then scatter that with a width of $\Delta Log_{10}[N_\mu] = 0.1$, simulating the performance of IceCube bundle resolution [23]. At 30 PeV, the potential for the surface veto to separate p/Fe is comparable to that already demonstrated for in-ice muons. By using both measures, p/Fe separation may be improved and the main uncertainties of the combined analysis (in-ice calibration and hadronic interaction models) may be addressed.

The left panel of Fig. 4 also suggests that muon production depth [24] may be used to inform on nucleon mass. The solid histograms show the true production depth as reported by CORSIKA. The unfilled histograms (labeled "Reco") show a simple estimate of depth derived from a proxy for the emission height $h = r_\perp^2/(2c\delta t)$ and an atmospheric density profile. Here δt is the arrival delay of the muon relative to a planar shower front. Realizing a good muon production profile

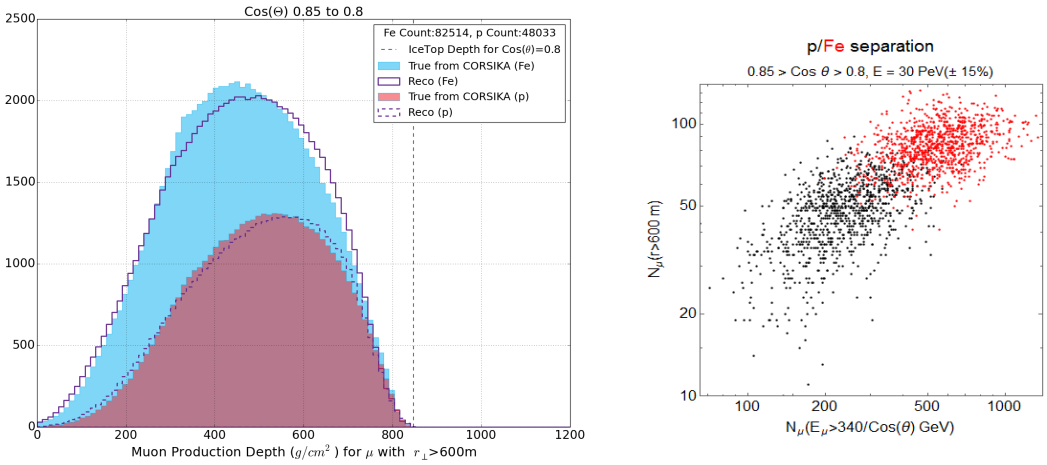

Figure 4: Potential for veto to contribute to composition studies (see text). Left: Average muon counts v X_μ, for 25 p/Fe showers at 30 PeV. Right: p/Fe separation showing both in-ice (x) and surface muons (y).

places requirements on a) the quality of IT2 reconstructed core positions, and b) the timing of muon signals from individual elements of the veto. Not only are earlier muons separated from the main part of the electromagnetic shower, but depth of muon production ($X_{max,\mu}, \langle X_\mu \rangle$) provides some separation between p and Fe. The very early part of the shower ($X < 200$ g/cm^2) is enriched for Fe showers relative to proton, and provides comparable separation to just using the bulk number of peripheral muons. Ultimately, with of order 100 muons to work with, we expect to fit the muon production depth to describe both the number of muons and the rise time of the muon signal, which will independently contribute to a mass resolution on a shower by shower basis.

Summary. IceCube executes a cosmic ray physics program with precision measurements of spectrum from 2-500 PeV and preliminary measurements of composition from 3-300 PeV. The program is limited by the size of IceTop, especially with regard to in-ice and/or surface muon measurements which are critical for measuring composition. *IceCube-Gen2* will present a 5-10 times larger footprint and $\sim$ 50 x larger coincident aperture. Two surface components are considered. *IceTop-2* would enable continuing the cosmic ray program with the larger aperture, significantly improving spectrum and composition measurements in the expected transition region of the cosmic ray spectrum. Gen2 would also include a veto to enhance the high energy neutrino science. A veto focused on sky coverage would increase the instrumentation footprint of Gen2 to 100 km^2, potentially improving the cosmic ray program as well. A veto focused on energy threshold would increase the density of instrumentation, employing 5,000-10,000 m^2 of particle detectors to veto air showers down to a few hundred TeV. Such a veto would plausibly produce counts of 50 or more peripheral muons for air showers with $E > 30$ PeV, providing another handle on composition in the region expected for a transition from galactic to extra-galactic cosmic rays.

References

[1] **IceCube** Collaboration, A. Achterberg et al., Astropart.Phys. 26 (2006) 155.

[2] **IceCube** Collaboration, R. Abbasi et al., arXiv:1207.6326 (2012).

[3] **IceCube** Collaboration, T. Feusels, K. Rawlins et al., *Latest Results on Cosmic Ray Spectrum and Composition from Three Years of IceTop and IceCube*, #334 these proceedings (2015).

[4] **IceCube** Collaboration, M. G. Aartsen et al., Phys. Rev. D 88, 042004, (2013).

[5] T. Feusels, Ph.D. thesis, University of Gent (2013).

[6] **IceCube** Collaboration, H. Dembinski, J.G. Gonzalez et al., *Surface Muons in IceTop*, #267 these proceedings (2015).

[7] **IceCube** Collaboration, J.G. Gonzalez et al., *Studying Cosmic Ray Composition with IceTop using Muon and Electromagnetic Lateral Distributions*, #338 these proceedings (2015).

[8] A. Haungs, *Cosmic Rays from the Knee to the Ankle"*, Physics Procedia 61 (2015) 425.

[9] **IceCube** Collaboration, M.G. Aartsen et al., Phys. Rev. Lett. 113, 101101 (2014).

[10] **IceCube** Collaboration, M.G. Aartsen et al., arXiv:1507.04005 (2015).

[11] **IceCube** Collaboration, M.G. Aartsen et al., arXiv:1412.5106 (2014).

[12] **IceCube-Gen2** Collaboration, E. Blaufus, C. Kopper, C. Haack et al., *The IceCube-Gen2 High Energy Array*, #1146 these proceedings (2015).

[13] **IceCube-Gen2** Collaboration, J. Auffenberg et al., *Motivations and Techniques for a Surface Detector to Veto Air Showers for Neutrino Astronomy with IceCube in the Southern Sky*, #1156 these proceedings (2015).

[14] **IceCube-Gen2** Collaboration, S. Euler, J.G. Gonzalez et al., *Simulation Studies for a Surface Veto Array to Identify Astrophysical Neutrinos at the South Pole*, #1070 these proceedings (2015).

[15] Data compilation from S. Tilav (tilav@udel.edu): (Tibet-III) M. Amenomori et al., Ap. J. 678, 1165 (2008), (ARGO-YBJ) VULCANO Workshop, arXiv:1408.6739v1 (2014), (Kascade) T. Antoni et al., Astropart. Phys. 24, 1 (2005), (Kascade-Grande) Advances in Space Research 53, 10, 1456, (2014), (GAMMA) Samvel Ter-Antonyan, Phy. Rev. D 89, 123003 (2014), (Tunka) V.V. Prosin et al., Nuc. Instr. & Meth. A756, 94 (2014), (HiRes 2)R.U. Abbasi et al. (HiRes Collaboration), Phys. Rev. Lett. 100 (2008) 101101, T. Abu-Zayyad et al. (TA) Astroparticle Physics 48, 16 (2013), A. Schulz et al. (Auger), Proc. 33rd ICRC, Rio de Janeiro, Brazil (2013), arXiv:1307.5059.

[16] **IceCube** Collaboration, M. G. Aartsen et al., Phys. Rev. D 87, no. 6, 062002 (2013)

[17] **IceCube** Collaboration, M. Sutherland et al., *Search for High Energy Neutron Point Sources in IceTop*, #250 these proceedings (2015).

[18] **IceCube** Collaboration, R. Abbasi et al., ApJ 746, 33 (2012).

[19] **IceCube** Collaboration, M. G. Aartsen et al., ApJ 765, 55 (2013).

[20] **IceCube** Collaboration, F.T. McNally, P. Desiatti, S. Westerhoff et al., *Anisotropy in Cosmic Ray Arrival Directions Using IceCube and IceTop*, #274 these proceedings (2015).

[21] **IceCube** Collaboration, K. Jero, D. Tosi et al., *IceTop as Veto for IceCube*, #1086 these proceedings (2015).

[22] **Auger** Collaboration, M.C. Medina et al., Nucl. Instrum. Meth. A566 (2006).

[23] **IceCube** Collaboration, M.G. Aartsen et al., submitted to Astropart. Phys., arXiv:1506.07981 (2015).

[24] **Auger** Collaboration, A. Aab et al., Phys. Rev. D 90, 012012 (2014).

PROCEEDINGS OF SCIENCE

Simulation Studies for a Surface Veto Array to Identify Astrophysical Neutrinos at the South Pole

The IceCube-Gen2 Collaboration[†]

[†]*http://icecube.wisc.edu/collaboration/authors/icrc15_gen2*

E-mail: sebastian.euler@icecube.wisc.edu, jgonzalez@icecube.wisc.edu, bsr25@uclive.ac.nz

Motivated by the discovery of high-energy astrophysical neutrinos with IceCube, we study the prospects for improved measurements of neutrinos of astrophysical origin with a surface array combined with IceCube or a next generation neutrino detector at the South Pole. Backgrounds in astrophysical neutrino searches are reduced by tagging muons and neutrinos of atmospheric origin by detecting the accompanying air shower. We consider various air shower array configurations, including different array layouts and detector station sizes, and study their air shower detection efficiency. We will report on the various approaches we have used to understand the capabilities of such arrays.

Corresponding authors: S. Euler[*1], J. Gonzalez[2], B. Roberts[3]

[1] *Dept. of Physics and Astronomy, Uppsala University, Uppsala, Sweden*

[2] *Bartol Research Institute, University of Delaware, USA*

[3] *Dept. of Physics and Astronomy, University of Canterbury, Christchurch, New Zealand*

The 34th International Cosmic Ray Conference,
30 July- 6 August, 2015
The Hague, The Netherlands

[*]Speaker.

1. Introduction

A crucial technique in the IceCube discovery of astrophysical neutrinos [2] was to use the outer layers of the detector as an active veto against penetrating muons. This approach, however, effectively reduces the fiducial volume of the detector by about 50%, and requires an additional cut on the observed charge, corresponding to an energy threshold of 30 TeV. An alternative possibility would be a dedicated veto array on the ice surface, tagging atmospheric muons by detecting the accompanying air shower. This approach would make it possible to use the full detector as target material, and in searches for muon neutrinos even the ice above the detector, since high-energy muons can reach the detector after being created several kilometers away. In fact, IceTop, the surface component of the IceCube Neutrino Observatory [3], is used as a veto array in several analyses [4, 5, 6], although its limited size covers only a small solid angle of the upper hemisphere (see Fig. 1). The prospects for a larger array are particularly interesting in the context of the planned extension IceCube-Gen2 [7]. If possible, a surface veto should be large enough to allow the observation of the Galactic Center and have an energy threshold that is low enough to study the astrophysical neutrino flux at lower energies than to date. A summary of motivations and techniques for such a surface array can be found in [8].

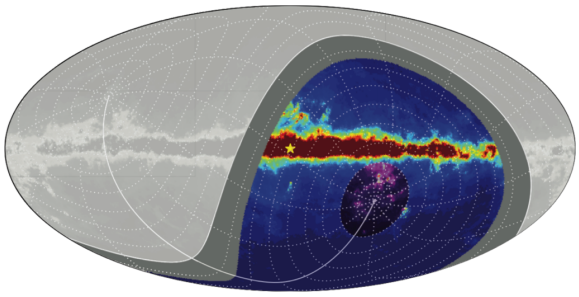

Figure 1: Skymap in galactic coordinates of a GALPROP π^0 1.1 TeV simulation. The colored area shows the approximate region of the sky covered by the veto arrays studied in this work, the purple region indicates coverage with the IceTop array. The yellow star marks the Galactic Center, the dark gray band the remaining region above the horizon that is not covered by the surface veto. Plot taken from [1].

The performance of a prospective array and its optimal geometry have to be estimated by simulations. Ideally, a full simulation should be generated, covering all aspects from the interaction of the cosmic ray in the atmosphere to the detector response including a simulation of the electronics. Such a full simulation is however very resource-intensive and cannot be done with high statistics for a large number of configurations, as desired in a design study.

Therefore, we follow two complementary approaches in parallel. We have developed a fast Monte Carlo simulation based on lateral distribution functions (section 2). This simulation uses only average shower properties, even though for a highly efficient veto exceptional showers become important. Nonetheless, with this approach we obtain a reasonable estimate of the performance of a large number of different array configurations within a short time. These simulations can guide the design process.

The parallel approach is a simulation chain based on detailed simulations of extensive air showers using CORSIKA [9], which includes simulating their interaction with various detector array configurations (section 3). While this approach is more resource-intensive, it allows the study of rare air showers. Examples are showers in which the primary cosmic ray interacts very deep in the atmosphere, or production of highly energetic muons in exotic processes. In this case

the footprint of the air shower, and therefore the detection probability on the surface, can be very small while still producing muons that reach IceCube. This approach enables the study other exotic processes that could produce a background.

2. LDF-based Monte Carlo simulation

2.1 Lateral Distribution Functions

The basis of the simulation described here are lateral distribution functions – empirical parameterizations of air showers – which describe the particle density in an air shower as a function of the lateral distance to the shower core.

An important aspect of a detector at the South Pole is that with time it will be gradually buried by drifting snow. The IceTop array observes attenuation of the electromagnetic component of the air showers, getting stronger with time [3]. A future surface veto array must therefore be either efficient enough to rely on the muonic component only, or constructed such that it is not buried by snow (e.g. on stilts above the surface). Therefore, we use separate formulations for the density of electrons and muons, taken from [10]. Their sum is equivalent to the classic formulation by Greisen [11]. Fig. 2a shows the individual functions for muons and electrons and their sum, together with the Greisen curve for a 300 TeV shower at the altitude of the South Pole (2835 m). It should be noted that the parametrizations used are quite old and will be superseded by more recent results from IceTop [12, 13] in the future.

While this approach could in principle also be applied to heavier primaries, the results presented here assume pure proton primaries. On the other hand, the approach by construction ignores variations in the shower development. Rare showers, where for example a large fraction of the primary energy is transferred to a single muon, cannot be simulated with this setup. Such events become important for a high-efficiency veto, and more detailed simulations are needed (see section 3).

2.2 Detection efficiency

To obtain the air shower detection efficiency for a given array geometry, the LDFs are evaluated at the positions of the simulated detector stations. From the particle density, a Poissonian probability to see a "hit" in each station is calculated, taking into account the station's surface area. Fig. 2b shows the footprint of a simulated 300 TeV shower with a zenith angle of 8° on the IceTop detector. With increasing shower inclination, the thickness of the detectors becomes important: the sensitive area of thin detectors (e.g. scintillator panels) is much smaller for very inclined showers than for vertical ones. More spherical detectors (e.g. water/ice Cherenkov tanks) have a more uniform sensitivity. This effect is also taken into account in the simulation.[1]

For a given energy and zenith angle, many similar showers are simulated. To emulate the conditions of a dedicated veto array and to save computation time, zenith angle and radial position are chosen in conjunction, such that high-energy muons from the shower pass through IceCube.

[1] This disadvantage of scintillation detectors can be partly compensated by tilting the panels increasingly with radius. This technique restores the apparent size for inclined showers, at least for detector stations close to the shower axis, but is currently not taken into account in the simulation.

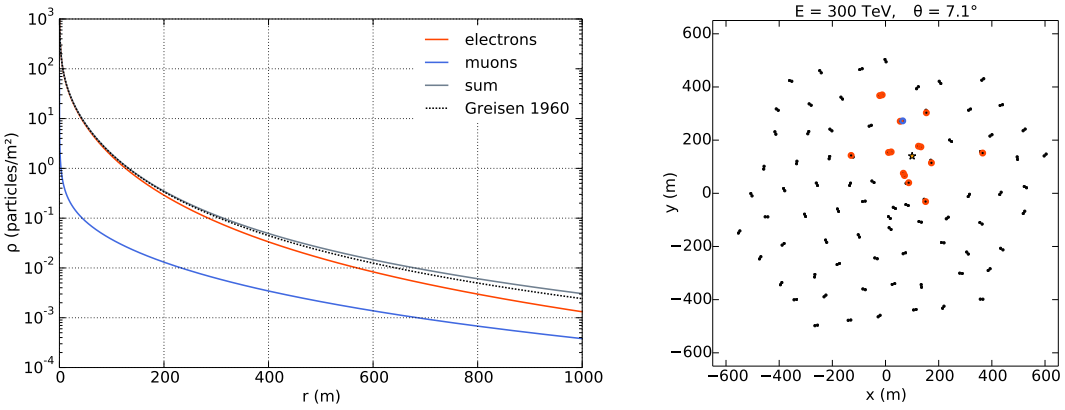

(a) Lateral Distribution Functions

(b) Simulated example shower

Figure 2: LDFs used in this study and the simulated footprint of a 300 TeV shower on the IceTop array. The tank marked in blue has registered a muon, tanks in red have detected the electromagnetic part of the shower. The orange star marks the surface position of the shower core.

For each shower, the whole array is considered "triggered" if at least one station has seen a hit. The detection efficiency is then the ratio of triggered showers to all simulated showers.

2.3 Geometries

Three example geometries are studied in detail here. The first (Fig. 3) is an extension of the existing IceTop array, called *IceVeto* [1]. It consists of IceTop in the center and 943 additional detector stations, each of the same size as one original IceTop tank. The new detectors are arranged in concentric rings around IceTop. In order to achieve a detection efficiency that does not depend strongly on the inclination of the air shower, while using as few tanks as possible, the distance between the rings increases with radius, while the distance between tanks along the same ring stays approximately the same. The array has a maximum radius of 6.7 km, corresponding to a zenith angle as seen from IceCube of $\theta \approx 75°$, and thus covers the elevation of the Galactic Center at $\theta = 61°$.

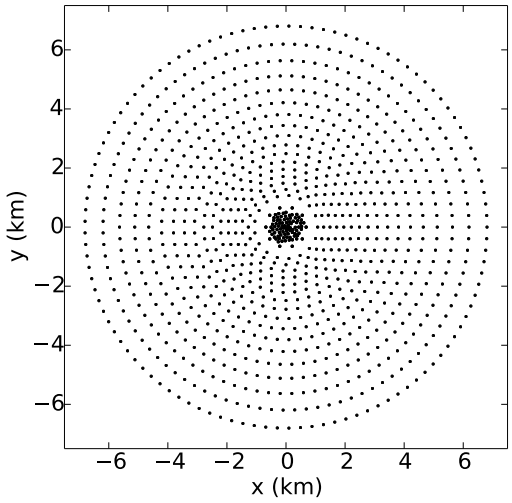

Figure 3: The IceVeto geometry.

The other two geometries are simpler designs. In these cases, the array covers a square area with a side of 14 km, such that for IceCube or a next-generation detector in the center, the array is again large enough to cover the elevation of the Galactic Center. The individual stations are

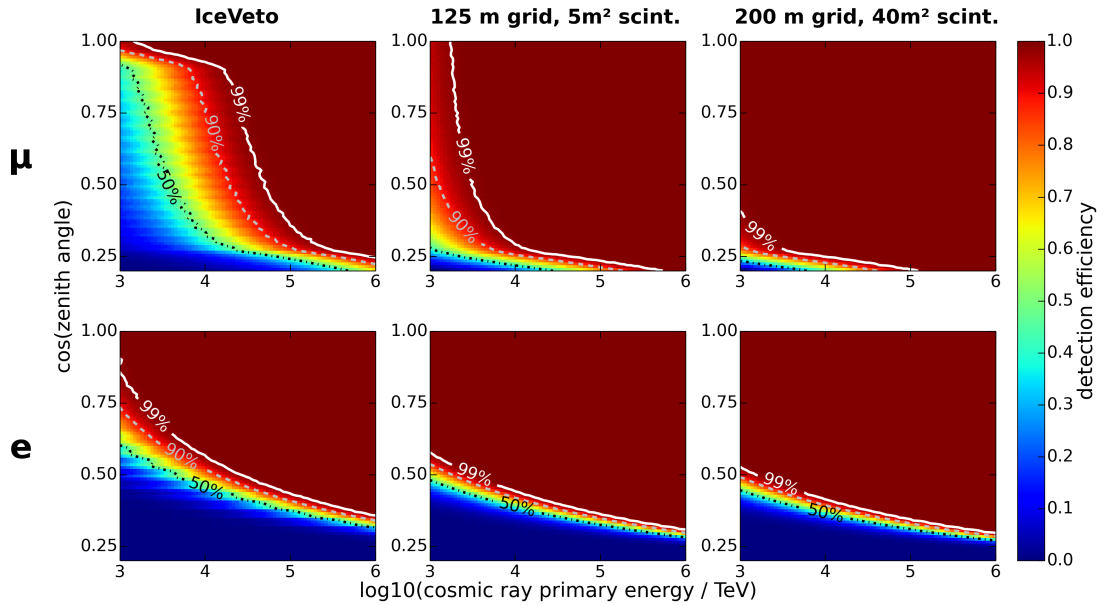

Figure 4: Detection efficiencies for IceVeto (left), the 125 m grid geometry (middle), and the 200 m grid geometry (right), separate for muons (top) and the electromagnetic shower component (bottom). The lines indicate detection efficiencies of 99% (white, solid), 90% (gray, dashed), and 50% (black, dot-dashed).

arranged on a regular rectangular grid. Two different combinations of detector area and station spacing are studied. The first variant has a dense grid with a spacing of 125 m, resulting in a total number of roughly 12 500 stations. Each station consists of a 5 m^2 scintillator panel of 1 cm thickness. An important parameter of a surface array is the *fill factor*, the ratio of sensitive area to total surface area. This design achieves a fill factor of 3.2×10^{-4}. The IceVeto geometry, for comparison, has a total fill factor of about 2×10^{-5}, albeit with a radially varying density. The second grid variant has a larger spacing of 200 m, resulting in 4900 stations, but assumes extremely large scintillator panels with an area of 40 m^2 to achieve a fill factor of 1×10^{-3}.

2.4 Results

The detection efficiency is calculated at 6000 test points on a grid of primary energies between 1 PeV and 1 EeV ($3.0 < \log(E_{prim}/\mathrm{TeV}) < 6.0$) and zenith angles between 0° and 78° ($1.0 > \cos(\theta) > 0.2$). For each point in this parameter space, 10 000 air showers were simulated. Fig. 4 shows the resulting detection efficiency maps as function of zenith angle and primary proton energy, together with the contour lines of 99%, 90%, and 50% detection efficiency.

For all geometries, the detection efficiencies for the electromagnetic part are larger than the muonic ones for very vertical showers, but show the characteristic fall-off towards larger zenith angles, where the large atmospheric depth causes the electromagnetic part of the shower to die out, and only the muons remain. The kink visible in the muon distributions at $\cos(\theta) \approx 0.27$ appears because for larger zenith angles the shower core positions are outside the array and only the outer parts of the showers hit the instrumented area. Similarly, the stripes in the IceVeto detection efficiencies are caused by the shower positions coinciding with the concentric rings of detector stations.

The IceVeto detection efficiencies exhibit another kink at very small zenith angles ($\cos(\theta) \approx 0.95$); this is where IceTop with its denser instrumentation becomes responsible for the shower detection. Overall, the IceVeto geometry becomes efficient from muons at primary energies above 10 PeV. The higher instrumentation density of the 125 m grid detector shifts the whole distribution towards lower energies by about one order of magnitude, and only the 200 m grid detector with its fill factor of $1000\,\mathrm{m}^2\,\mathrm{km}^{-2}$ is more than 99% efficient over almost the whole parameter space studied. If high detection efficiencies at energies below 1 PeV are desired, a dense intrumentation is needed.

3. CORSIKA-based MonteCarlo Simulation

As discussed in the introduction, one advantage of a detailed simulation of air showers and detector response is the possibility to study rare phenomena. With a proton-air interaction length of about $70\,\mathrm{g\,cm}^2$, a fraction of 10^{-3} primary protons survive to a depth of $490\,\mathrm{g\,cm}^2$. Compare that to the roughly $690\,\mathrm{g\,cm}^2$ vertical depth of South Pole. Deep showers develop in a significantly denser atmosphere than average showers and hit the ice within a few interaction lengths of the first interaction. This reduces the probability that high-energy pions decay, and modifies the number and energy spectrum of the muons in the air shower. Conversely, primaries that interact high in the atmosphere develop on a less dense medium than average. Understanding the effects of these shower-to-shower fluctuations requires a detailed simulation of the cascading process.

In this study, 23 000 proton-induced air showers were simulated with energies between 10 TeV and 5 PeV and zenith angles less than 65°. We used CORSIKA with the Sibyll 2.1 high-energy interaction model [14]. The simulation included a simplified model of the detector response with various detector array configurations. We have considered an array of scintillation detectors, each one consisting of one 1 cm thick polypropylene scintillator panel of varying surface area laid flat on to the surface of the ice. The signal recorded at each scintillation detector is proportional to the energy loss in the detector according to Bethe's formula. The signal is expressed in units of *Vertical Equivalent Muon* (VEM), defined as the signal deposited by a 3 GeV muon crossing the detector vertically. With this convention, the threshold for recording a signal was set to 0.3 VEM. The flexibility of our setup will allow us to replace this simulation by a more detailed one in the future. In order to understand the effect of deep air showers, we simulated a small set of 2000 quasi-vertical ($\theta < 20°$) proton-induced showers where the primary was forced to interact at points evenly distributed in depth between 0 and $500\,\mathrm{g\,cm}^2$.

3.1 Results

The air shower detection efficiency can also be expressed as a *passing fraction*, the fraction of air showers that do not trigger the veto array. This is shown in Figs. 5a and 5b in the case of four representative configurations and for vertical/inclined air showers. Using a simple scaling model, one expects the veto threshold to be proportional to the square of the array spacing and inversely proportional to the scintillator surface area. In other words, the *fill factor* described above. This implies that there is a trade-off between detector size and array spacing, but this is true only if the array spacing is comparable to the typical air shower footprint size. This can be seen in Fig. 5a, where decreasing array spacing and scintillator area while keeping the total fill factor constant produces a decrease in the passing fraction (light/dark blue points in Fig.5a). This is related to

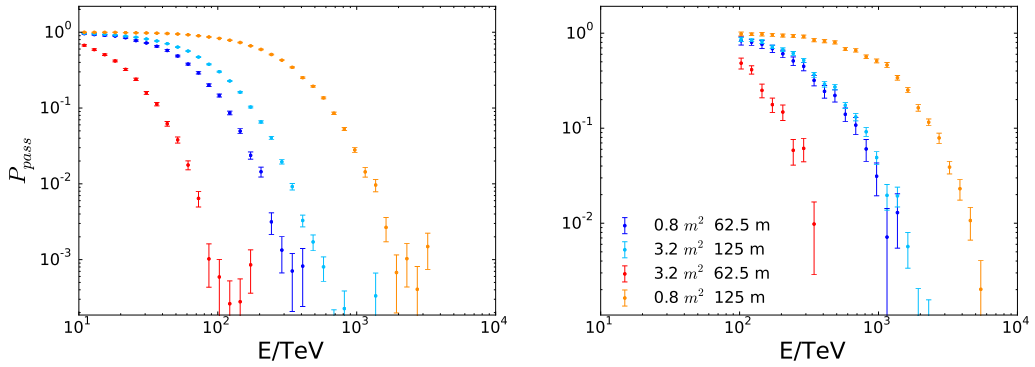

(a) $\theta < 25°$ (b) 53°– 56°.

Figure 5: *Passing fraction* of *quasi-vertical* air showers ($\theta < 25°$) and of showers arriving between 53° and 56°. We show array configurations that have a spacing of 62.5 m or 125 m and a scintillator surface area of 0.8 m^2 or 3.2 m^2. The light and dark blue sets of points are configurations with equal fill factor, the change in detector spacing being offset by a change in scintillator area. The fill factors for these configurations are 9.5×10^{-4}, 2.4×10^{-4} and 5.9×10^{-5}. For a discussion see text.

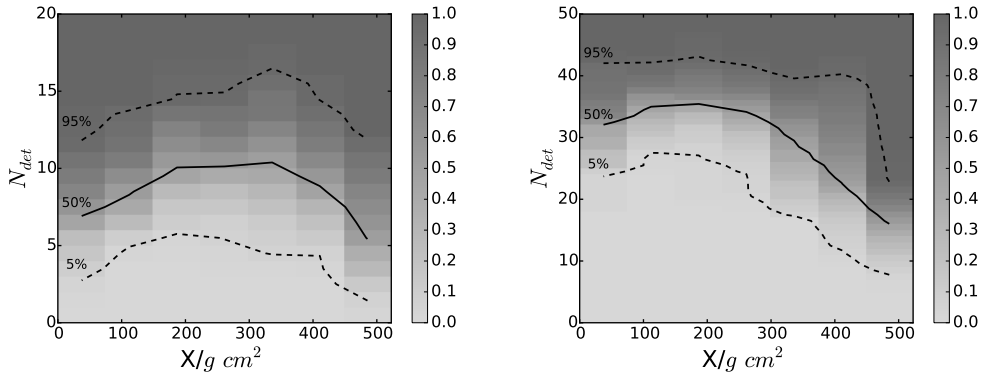

(a) 100 TeV (b) 800 TeV

Figure 6: Fraction of air showers with number of detectors with signal smaller than N_{det}, as a function of the depth of first interaction of the primary cosmic ray X. The lines correspond to the 5%, 50% and 95% quantiles. Two primary energies are displayed: 100 TeV (left) and 800 TeV (right). Both correspond to 3.2 m^2 scintillators in a regular triangular array with 62.5 m spacing.

the fact that the detection is dominated by the electromagnetic component of the air shower. By contrast, in Fig. 5b, where the air showers are dominated by the muon component, with a wider extent, the scaling holds.

The effect of the point of first interaction can be seen in Figs. 6a and 6b. The highest point of the curve corresponds to events in which the shower maximum lies at the surface. One can clearly see that deeper and shallower showers have a lower number of detectors registering a signal. At 800 TeV, the fraction of showers not detected by the veto are mostly produced at large depths, while at 100 TeV some of them are produced at small depths. This is for quasi-vertical air showers,

but one expects a similar behavior for inclined air showers.

The passing fraction was estimated down to values around 10^{-3}, as seen in Fig. 5. In order to probe smaller values, more efficient ways of generating simulated datasets are needed. The passing fraction is determined mostly by the primary point of first interaction, as shown in Fig. 6. It is also affected by the subsequent development of the air shower. We are working on algorithms that exploit this fact in order to efficiently simulate showers that have a small probability to be detected by the surface veto.

4. Summary

There are qualitatively two distinct *regimes* for a surface veto: vertical ($\cos(\theta) \gtrapprox 0.5$) and inclined ($\cos(\theta) \lessapprox 0.5$) (Fig. 4). Focusing on one or the other leads to different detector design decisions. In the vertical case, the threshold is determined by the sensitivity to the electromagnetic component of the air shower, and it depends on the snow accumulation. In this case, thresholds as low as 100 TeV seem to be attainable with a fill factor of 10^{-3}, and reasonable array spacing and size (5). In the inclined case, the threshold depends on the sensitivity to muons and it is larger by about a factor of 4 at 55°. In both cases a detailed study must be done in order to estimate the energy at which the detectors reach a passing fraction of 10^{-4} to 10^{-6}. A detailed simulation of air showers and the in-ice detector response are needed to understand the effect of rare events.

References

[1] **IceCube** Collaboration, *IceVeto: An Extension of IceTop to Veto Horizontal Air Showers*, in *Proc. of the 33rd ICRC #374, Rio de Janeiro, Brasil*, 2013. arXiv:1309.7010.

[2] **IceCube** Collaboration, M. G. Aartsen et al., *Science* **342** (2013) 1242856, [arXiv:1311.5238].

[3] **IceCube** Collaboration, R. Abbasi et al., *Nucl.Instrum.Meth.* **A700** (2013) 188–220, [arXiv:1207.6326].

[4] **IceCube** Collaboration, *A search for extremely high energy neutrinos in 6 years of IceCube data*, #463 in these proceedings.

[5] **IceCube** Collaboration, *Results of neutrino point source searches with 2008-2014 IceCube data above* 10 TeV, #187 in these proceedings.

[6] **IceCube** Collaboration, *IceTop as Veto for IceCube*, #807 in these proceedings.

[7] **IceCube** Collaboration, *The IceCube-Gen2 High Energy Array*, #741 in these proceedings.

[8] **IceCube** Collaboration, *Motivations and Techniques for a Surface Detector to Veto Air Showers for Neutrino Astronomy withIceCube in the Southern Sky*, #959 in these proceedings.

[9] D. Heck, G. Schatz, T. Thouw, J. Knapp, and J. N. Capdevielle, *FZKA-6019* (1998).

[10] T. K. Gaisser, *Cosmic Rays and Particle Physics*. Cambridge University Press, 1991.

[11] K. Greisen, *Ann.Rev.Nucl.Sci* **10** (1960) 63–108.

[12] **IceCube** Collaboration, *Surface Muons in IceTop*, #363 in these proceedings.

[13] **IceCube** Collaboration, *Studying Cosmic Ray Composition with IceTop using Muon and Electromagnetic Lateral Distributions*, #806 in these proceedings.

[14] E. J. Ahn, R. Engel, T. K. Gaisser, P. Lipari and T. Stanev, Phys. Rev. D **80** (2009) 094003

PROCEEDINGS OF SCIENCE

A Precision Optical Calibration Module for IceCube-Gen2

The IceCube-Gen2 Collaboration[†]

[†] *http://icecube.wisc.edu/collaboration/authors/icrc15_gen2*

E-mail: kai.krings@icecube.wisc.edu

A next generation of IceCube is under design including the Precision IceCube Next Generation Upgrade (PINGU) for the neutrino mass ordering and an extended array for astrophysical neutrino sources. A new level of precision is needed in order to guarantee improved performance with respect to IceCube. An improved calibration system will enable a better understanding of the ice and will therefore significantly reduce systematic effects. We present a new instrument called the Precision Optical Calibration Module (POCAM). By keeping the outer topology identical to that of the IceCube Digital Optical Module (DOM), cost-effective construction and deployment is ensured. The design of the POCAM is based on the principle of an inverted integrating sphere. An appropriately placed LED in combination with a diffusing layer on the inside of the sphere results in a nearly homogeneous light emission from the apertures in the spherical housing. The output of the LED is monitored *in-situ* to high precision, ensuring control over the output from the apertures. The POCAM has been simulated and tested in the framework of Geant4. A prototype POCAM is under construction. We report on the status of the POCAM R&D.

Corresponding authors: K. Krings*[1], K. Abraham[1], K. Holzapfel[1], M. Jurkovič[1], E. Resconi[1], J. Veenkamp[1]

[1] *Physik-Department, Technische Universität München, James-Franck-Str., D-85748 Garching, Germany*

The 34th International Cosmic Ray Conference,
30 July- 6 August, 2015
The Hague, The Netherlands

*Speaker.

1. Introduction

For the next generation of IceCube (*IceCube-Gen2*) [1], two different detectors are under study: the Precision IceCube Next Generation Upgrade (PINGU) [2] for the determination of the neutrino mass ordering through a precise measurement of atmospheric neutrino oscillations and a high-energy array [3] instrumenting about 10 km^3 volume of Antarctic ice for high-statistics observations of astrophysical neutrino sources. Both share a common Digital Optical Module (DOM) design, which includes a calibration system similar to IceCube: each DOM is equipped with 12 LEDs, pointing radially outward from the DOM. The calibration system will be used to measure the optical ice properties and the DOMs' timing, sensitivity, positions, and orientations. For IceCube, it has provided the level of precision required for the present detector operation. On the other hand, it lacks an *in-situ* monitoring of the emitted light pulses. LED variation over time as well as LED-by-LED variations limit the precision presently obtained in IceCube. We propose here a self-calibrated, homogeneous, pulsed, and multi-wavelength calibration module: the Precision Optical Calibration Module (POCAM). With the POCAM, measurements of the energy scale and resolution will be performed to the percent precision level, and an even more precise understanding of the optical properties of the Antarctic ice and DOM sensitivity will be provided.

2. POCAM performance goals

The POCAM, shown in Fig. 1, is a calibration device, which will be located on the communication/power cable alongside the DOMs. The POCAM's main goal is a homogeneous and fast illumination of a large part of the instrumented ice volume by providing an isotropic pulsed light source. Fast illumination refers to high-peaked light pulses with short decay times.

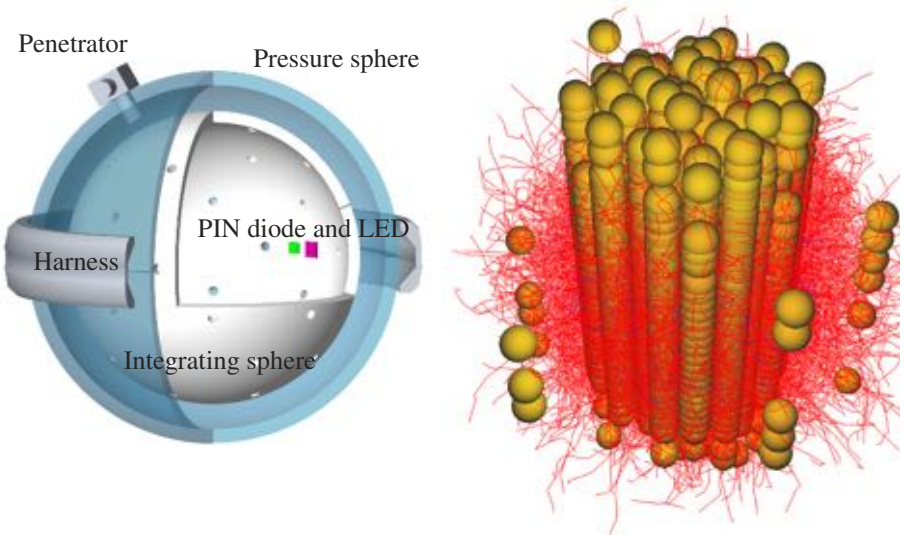

Figure 1: Left: POCAM as a 48 multi-port integrating sphere with a diameter of 24 cm placed in an IceCube pressure sphere. Right: first microsecond of the photon propagation of an idealized isotropic POCAM flash inside PINGU.

Assuming an ideal POCAM, no saturation in the DOMs, and a suitable dynamic range, we want to verify the detector's energy scale and energy resolution[1] at the level of a few percent and measure the absorption and scattering lengths of the Antarctic ice at a level of better than 10 %. The equivalent energy range covered by the POCAM is between a few GeV and some TeV, in the specific case of PINGU. More intense light pulses can be built for a high-energy optimized POCAM. Because the PINGU baseline geometry has a symmetry in the azimuth direction and an up-down asymmetry due to the DOMs' asymmetric construction, we aim for a homogeneous ice illumination on the order of 1 % and 10 % in azimuth and zenith directions, respectively.

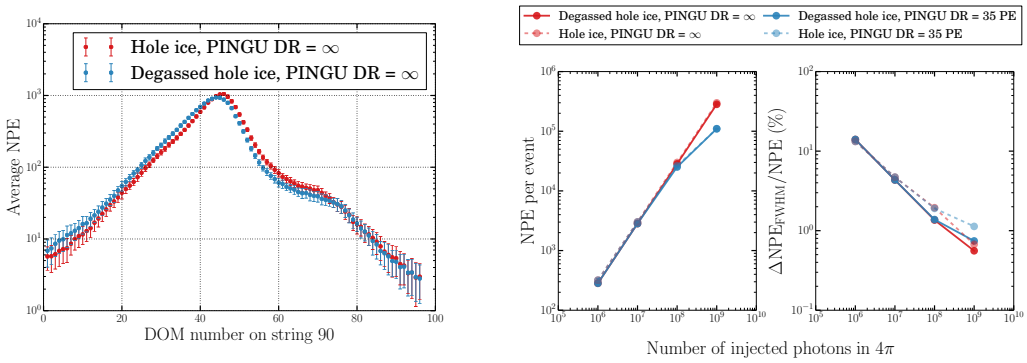

Figure 2: Left: response of DOMs on string 90 to POCAM flashes from the middle of string 88 with 10^9 photons per pulse. Middle: detector response to POCAM flasher pulses of different brightnesses. Right: energy resolution as function of the POCAM brightness. PINGU's dynamic range (DR) was either assumed to be unlimited or restricted to a maximum number of collected photoelectrons (PE) per DOM of 35 PE.

An important design parameter is the light intensity necessary to address the energy scale verification and energy resolution. To answer this question, we have simulated the propagation of individual photons with $\lambda = 405\,\text{nm}$ (IceCube's standard flasher LED) in the Antarctic ice, emitted by an idealized POCAM as an isotropic point-like light source. The photons were propagated from the light source to the individual optical modules of both the existing IceCube and the planned PINGU detectors. For the simulation, we have used the current PINGU baseline geometry [4]. The light source has been placed in the middle of a central PINGU string. We have simulated a light emission with an ideal delta-like time profile yielding between 10^6 and 10^9 photons per pulse. This light intensity is equivalent to a cascade-like physics event with deposited energy between 6 GeV and 6 TeV, respectively. For the light propagation through the Antarctic ice, we have used IceCube's SPICE-Lea [5] ice model in two variations. The first variation labeled as *hole ice* corresponds to the current IceCube refrozen drill hole ice with increased scattering. In the second version, the planned improvement in the drilling technology is taken into account, which should lead to reduced light scattering in newly frozen ice. The latter version is labeled as *degassed hole ice*. The scattering of light in the hole ice affects the amount of light registered by a DOM coming from a particular direction and thus influences the DOMs' angular response. Indeed, this effect is visible in the simulation of light collection for DOMs on string 90, which is the closest neighbouring string to the light source (see Fig. 2, left). The limited dynamic range of the PINGU readout electronics will affect the reconstruction of bright POCAM flashes and thus impact the energy scale verification

[1] Here, energy resolution is defined as $\Delta\text{NPE}_{\text{FWHM}}/\text{NPE}$, where NPE is the number of photoelectrons.

and resolution. To estimate the limiting brightness, we have limited the maximum collected charge to 35 photoelectrons. Such a hard limit is a rather conservative modelling of PINGU's electronics saturation but can be considered as a worst-case scenario. As shown in the middle plot of Fig. 2, in this configuration saturation starts to play a role at flasher brightnesses above 10^8 photons per pulse. In the investigated flasher brightness range, the energy resolution drops from 14 % (10^6 photons per pulse) down to ~1 % (10^8 photons per pulse) (see Fig. 2, right).

3. POCAM components

The POCAM is composed of a light source that has to be intense and fast enough for our purpose here: an *in-situ* light monitoring system that will guarantee a precise knowledge of the light emitted in the ice, a diffusing sphere to generate homogeneous illumination from a discrete light source, and a housing that will allow safe deployment and operation of the POCAM in the deep ice. A matrix of monochromatic fast-switched (few nanoseconds) LEDs with different wavelengths from 370 to 500 nm will be used as a light source. The LEDs are driven by the Kapustinsky circuit [6], which has become popular in astroparticle physics experiments for time and amplitude calibration, including neutrino telescopes (e.g. [7, 8]). This driver is capable of driving LEDs with pulses of few ns FWHM, and the LED provides light pulses with up to 10^9 photons per pulse. This photon yield corresponds to an electromagnetic shower with an energy of ~6 TeV. The light intensity can be controlled only by the applied supply voltage ($V_{CC} < 24$ V). A fast solid state detector such as photodiodes or silicon photomultipliers are implemented in the POCAM in order to continuously *in-situ* monitor the light emitted with a precision of about 1 %. The emitting sphere is composed of an integrating sphere operated in an inverted mode respect the standard one. The highly reflective polytetrafluoroethylene (PTFE) internal layer is used to diffuse the photons from the light source. Multiple ports are then constructed to create a possibly diffused light source. As an alternative to the multi-port setup, a semi-transparent diffusing sphere is also under investigation. To study the performance of the two diffusing sphere options and to optimize the geometry of the POCAM, a dedicated Geant4 [9] simulation has been developed. First results are reported in Sec. 4. The well-tested IceCube pressure sphere is used for the housing of the POCAM. This choice reduces the homogeneity of the POCAM via the presence of the penetrator, the waistband/harness at the equator of the glass sphere, and the cable shadowing, but eases the integration of the POCAM into the standard deployment operations. Presently, a (semi-)transparent waistband and a thinner harness are under study. Moreover, all shadowing influence the measurement at short distances, e.g. at the closest DOMs to the POCAM, but their impact is highly reduced as the distance from the POCAM increases due to photon scattering in ice.

4. POCAM performance study

To optimize the POCAM, a dedicated Geant4 [9] simulation has been implemented. We report here preliminary results of the performance studies done for the multi-port as well as for the semi-transparent layer setup.

4.1 Multi-port setup

As a first step, the POCAM diffusing sphere has been implemented as a multi-port integrating sphere, placed inside the IceCube pressure sphere as shown in Fig. 1. Both volumes are filled with air. The focused light output of the LED, attached to the integrating sphere's inner layer and facing the opposite direction, is diffused inside the integrating sphere after several reflections on the inner diffusing layer and released into the surrounding ice after passing one of the multiple ports in the integrating sphere and the outer pressure sphere. Light homogeneity and timing were investigated by varying the integrating sphere diameter, the number of ports, and the port position and size. The outer pressure sphere has a fixed diameter of 33 cm, and all photons quantities were stored with respect to a reference detection sphere with a diameter of 40 cm. Absorption in both the integrating sphere and the pressure sphere as well as shadowing by the waistband/harness and the penetrator were taken into account. Not studied so far are the influence of the main cable, electronic components inside the POCAM, the hanging assembly, and the port shape. In the simulation, the integrating sphere's thickness has been idealized to be 1 mm. Each port is shaped as a spherical sector with an opening angle α. IceCube's standard 405 nm LED was simulated with a Gaussian wavelength, a uniform cosine-law angular, and a rectangular timing distribution. Wavelength standard deviation, opening angle, and pulse width were adjusted to 10 nm, 10°, and 10 ns, respectively. PTFE with a reflectivity of about 99 %, provided by manufacturers[2], was chosen as the material for the integrating sphere. Values for the pressure sphere's absorption length were taken from IceCube laboratory measurements. The pressure sphere's refractive index of 1.48 was fixed.

Config.	D/cm	n	α/°	T	A	Inhomogeneity		
						$\theta < 60°$	$60° \leq \theta \leq 120°$	$\theta > 120°$
C1	24	768	1	1.46 %	61.0 %	11.9 %	18.5 %	11.6 %
C2	6	768	1	1.46 %	74.4 %	14.7 %	56.4 %	10.3 %
C3	24	768	2	5.85 %	37.3 %	12.9 %	18.9 %	12.1 %
C4	24	192	2	1.46 %	57.7 %	12.3 %	17.8 %	11.6 %
C5	24	–	–	–	50.3 %	12.4 %	14.5 %	12.4 %

Table 1: POCAM configurations: integrating sphere diameter D, number of ports n, port opening angle α, effective photon transparency T, photon absorption A, and inhomogeneity for three different zenith angle zones. Configuration *C5* corresponds to the semi-transparent setup described in section 4.2.

Four different POCAM multi-port configurations listed in Tab. 1 were investigated. The baseline geometry consists of an integrating sphere with a diameter of 24 cm and 768 equidistantly distributed equal ports with an opening angle of 1°, which results in an effective transparency of the integrating sphere to photons of 1.46 %. Effective photon transparency T and photon absorption A are defined as

$$T = n \cdot \frac{\Delta\Omega_{\text{port}}}{4\pi} = n \cdot \frac{1-\cos(\alpha/2)}{2}, \quad A = 1 - \frac{N}{N_0}, \tag{4.1}$$

where n is the number of ports, $\Delta\Omega_{\text{port}}$ the solid angle of one port, α the port opening angle, N the number of photons emitted from the POCAM, and N_0 the number of photons emitted from the LED. In order to avoid too many non-reflected photons, T was restricted to a maximum value of

[2] SphereOptics Zenith Polymer®

about 5 %. The inhomogeneity of the POCAM's photon emission is defined as the ratio of σ and $\bar{N}$, where

$$\sigma = \sqrt{\frac{1}{n_k - 1} \sum_{k \in \Delta\Omega} (N_k - \bar{N})^2}, \quad \bar{N} = \frac{1}{n_k} \sum_{k \in \Delta\Omega} N_k. \tag{4.2}$$

Here, N_k are the emitted photon counts per bin k lying in the solid angle region $\Delta\Omega$ and n_k the number of bins. The inhomogeneity was calculated for the solid angle regions representing the harness shadow and for the regions above and below. Fig. 3 shows the corresponding distributions of the photon emission direction for all POCAM configurations.

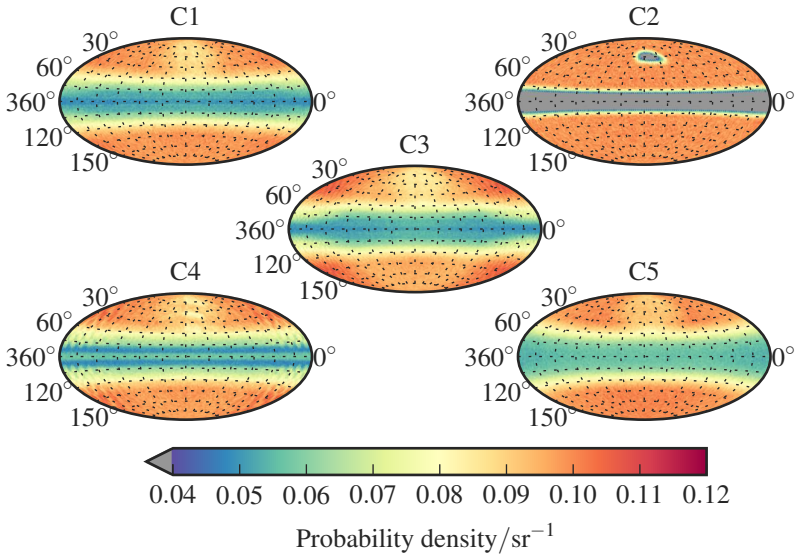

Figure 3: Photon emission direction. In this representation, the LED and penetrator positions are at $\phi = 0°, \theta = 90°$ and $\phi = 180°, \theta = 30°$, respectively. The harness is between $\theta = 79°$ and $\theta = 101°$. Configuration *C5* corresponds to the semi-transparent setup described in section 4.2.

The inhomogeneities due to the shadows of harness and penetrator are clearly visible for zenith angles between 60° to 120° and for azimuth angles below 30° or above 300° in the northern hemisphere, respectively. The shadows get smaller but more pronounced if the size of the integrating sphere is reduced. Except one outlier for configuration *C2* (see Tab. 1), all inhomogeneities are on the order of 10 to 20 %. On average, the baseline configuration gives the best homogeneity. If decreasing the number of ports or increasing the port size, an imprint of the port positions becomes visible as a third source of inhomogeneities due to photons entering the ice without being reflected on the inner diffusing layer or only once. With an integrating sphere diameter of 6 cm for configuration *C2*, almost no photons are emitted horizontally from the POCAM, which explains the large inhomogeneity value of 56.4 %. A different conclusion for the most homogeneous configuration can be drawn, if the shadow regions due to harness and penetrator are not taken into account. Fig. 4 shows the average photon emission direction in azimuth direction for different zenith angle bands. Taking eq. 4.2, configuration *C2* has the smallest deviations in the azimuth direction, which is on the order of 2 %. However, the deviations in the zenith direction are still significantly larger than our requirement of less than 10 %. Thus, the POCAM geometry needs to be further optimized.

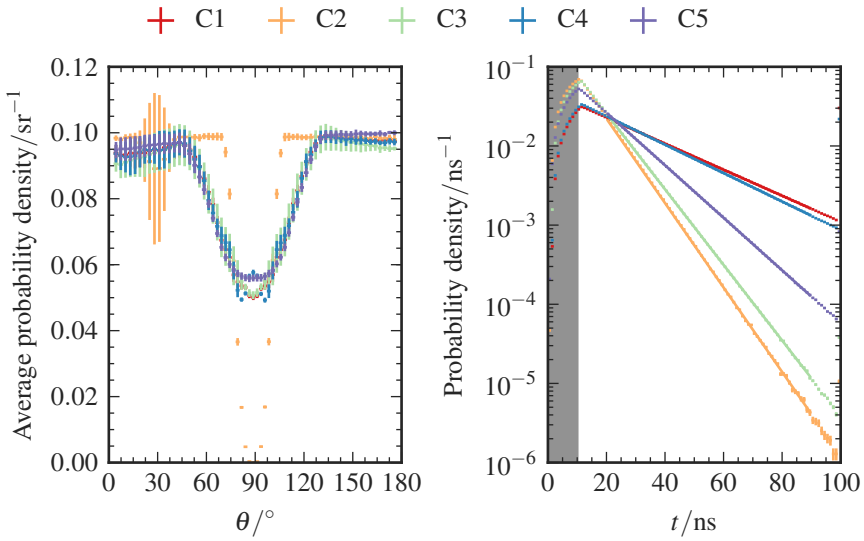

Figure 4: Left: average photon emission direction in azimuth direction for different zenith angle bands. The error bars show the standard deviation. Right: emission time profile. The shaded area refers to the rectangular LED time profile with a width of 10 ns. An exponential distribution is fitted to each time profile for $t > 20$ ns and shown as a solid line.

In Fig. 4, the time profile of configurations *C1* to *C4* are shown. The spectrum is mostly influenced by the effective photon transparency. For a larger ratio of $\Delta\Omega_{\text{port}}/4\pi$, more photons leave the POCAM early. The rising part of the time spectrum is strongly dependent on the emission profile of the LED. The position of the peak is independent of the chosen configuration. Nevertheless, the peak is slightly higher for both configuration *C2* and *C3*. The time distribution falls exponentially after the peak. The decay times are $\tau_1 = 26.4$ ns, $\tau_2 = 8.1$ ns, $\tau_3 = 9.1$ ns, and $\tau_4 = 24.2$ ns. A fraction of the photons leave the integrating sphere earlier, resulting in a higher peak and a shorter decay time τ.

4.2 Semi-transparent setup

The semi-transparency and diffusivity are simulated by defining probabilities for the photon to be either diffusely reflected, diffusively transmitted, or absorbed every time its path coincides with the integrating sphere: P_{refl}, P_{trans}, and $P_{\text{abs}} = 1 - P_{\text{refl}} - P_{\text{trans}}$. To establish diffuse transmission, slight modification to Geant4 have been made. The used probabilities are based on data provided by manufacturers[2]. The probability of diffuse transmission can serve as an analogue to eq. (4.1). As a first result, we present a simulation of a semi-transparent PTFE integrating sphere with $D = 24$ cm, $P_{\text{refl}} = 0.960$, and $P_{\text{trans}} = 0.025$. This simulation produces inhomogeneities listed in Tab. 1 for configuration *C5*. In Fig. 4, the azimuth direction for different zenith angle bands are shown, together with the time profile. The time profile's exponential part has a decay time of $\tau = 13.1$ ns. The time profile of the multi-port baseline configuration is shown for comparison. These simulations show that a semi-transparent PTFE integrating sphere offers advantages over the multi-port configurations. In this configuration, single-reflected photons are as likely as in the port configuration, but independent of the location. The pattern of inhomogeneities is clearly visible for

configuration *C3* and *C4* (see Fig. 3). For configuration *C1* and *C2*, this pattern is present, but less visible. In the semi-transparent PTFE configuration, this pattern is spread out, principally leading to a higher level of homogeneity. This effect is visible in the zenith angle bands (see Fig. 4, left), where the transition from shadow to non-shadow is continuous, whereas it is stepwise for the multi-port configurations. In spite of the clear advantages of a semi-transparent PTFE configuration over the multi-port configurations, conclusive statements would be premature because PTFE is difficult to simulate [10].

5. Conclusions and outlook

We have presented here first ideas and investigations of a new Precision Optical Calibration Module (POCAM). A few POCAM modules deployed uniformly in *IceCube-Gen2* at different depths will help to verify the energy scale and resolution of the future arrays and to determine the optical properties of the South Pole ice with a superior precision compared to present values. With the dedicated POCAM simulation in Geant4, we are able to draw first conclusions on the design of the POCAM geometry: the POCAM configuration consisting of an integrating sphere with a diameter of 6 cm and 768 equidistantly distributed ports with an opening angle of 1° gives the most homogeneous photon emission with inhomogeneities on the order of 2 % in the azimuth direction, which is close to the level of precision we want to achieve; the 6 cm integrating sphere results in a timing with fast rising edges, which are suitable to trigger the continuous pulse monitoring, and decay times below 10 ns; and the POCAM configuration as a semi-transparent diffusing sphere gives also positive results showing a photon emission which is not restricted to discrete locations. The homogeneity in the zenith direction has still to be improved in order to reach a precision of less than 10 %. However, this requirement may be relaxed if photon scattering in the ice is taken into account. Following these first encouraging achievements, we plan to complete the design study and to enter the prototyping phase soon.

References

[1] **IceCube-Gen2** Collaboration, M. Aartsen et al., arXiv:1412.5106.

[2] **IceCube-PINGU** Collaboration, M. Aartsen et al., arXiv:1401.2046.

[3] **IceCube-Gen2** Collaboration, E. Blaufuss et al., *PoS(ICRC2015)1146 these proceedings* (2015).

[4] **IceCube-Gen2** Collaboration, K. Clark et al., *PoS(ICRC2015)1174 these proceedings* (2015).

[5] **IceCube** Collaboration, D. Chirkin, *Evidence of optical anisotropy of the South Pole ice*, in *Proceedings of the 33rd International Cosmic Ray Conference*, 2013. arXiv:1309.7010.

[6] J. Kapustinsky et al., *Nucl. Instrum. Meth.* **A241** (1985), no. 2–3 612–613.

[7] **ANTARES** Collaboration, M. Ageron et al., *Nucl. Instrum. Meth.* **A578** (2007) 498–509, [astro-ph/0703355].

[8] F. Ritter et al., *Nucl. Instrum. Meth.* **A617** (2010), no. 1–3 420–421.

[9] **GEANT4** Collaboration, S. Agostinelli et al., *Nucl. Instrum. Meth.* **A506** (2003) 250–303.

[10] A. K. Soper et al., *Journal of Physics: Condensed Matter* **25** (2013), no. 45 454219.

PROCEEDINGS OF SCIENCE

A dual-PMT optical module (D-Egg) for IceCube-Gen2

The IceCube-Gen2 Collaboration[†], **H. Ijiri**[1]

[†] *http://icecube.wisc.edu/collaboration/authors/icrc15_gen2*

[1] *Department of Physics, Chiba University, Chiba 263-8522, Japan*

E-mail: lu.lu@icecube.wisc.edu

The upgrade of the IceCube neutrino observatory (IceCube-Gen2) enhances the detection capability of neutrinos with a few hundred TeV energies or greater by the increased instrumented volume in the glacier ice. Enhancement of the optical sensor performance in detecting ultraviolet photons can be a key factor for IceCube-Gen2 to achieve a higher sensitivity as more Cherenkov photons are expected in the short wavelengths. We have developed an optical module housing two 8″ photomultiplier tubes (PMTs) in an UV transparent, oval-shaped glass housing. The two high-QE PMTs are installed in a way facing both up and down so that the resultant angular acceptance is more uniform. This uniformity of optical acceptance further improves the detection of downward-going events and background veto efficiency compared to the current IceCube optical sensors. In addition, the improvements on UV transmittance of the glass housing and the inner gel lead to an improvement of the photon detection efficiency by a factor of four at wavelengths shorter than 340 nm.

Here, the initial performance of the first prototype module of D-Egg is reported. We also present simulation studies of the IceCube-Gen2 performance with the new dual-PMT modules.

Corresponding authors: L. Lu[*1], A. Ishihara[1], S. Yoshida[1]

[1] *Department of Physics, Chiba University, Chiba 263-8522, Japan*

The 34th International Cosmic Ray Conference,
30 July- 6 August, 2015
The Hague, The Netherlands

[*] Speaker.

The high-energy extension of the IceCube experiment aims at improving the sensitivity for the detection of neutrinos with few hundreds of TeVs and energies beyond. To achieve this, a larger instrumented volume is needed and the spacing between strings will be increased [1]. To improve the efficiency for detecting Cherenkov photons, one can use new types of glass-housings that are more UV-transparent. In addition, the direction information of photons might help with vetoing atmospheric muon backgrounds. The design of the new detector, D-Egg (Dual optical sensors in an Ellipsoid Glass for Gen2), has been optimised to increase the detection efficiency for UV photons and angular acceptance at a minimum additional cost. The advances of D-Egg make it also an excellent candidate to be the light sensors of the low-energy upgrade, PINGU [2], which focuses on precise measurements of low-energy neutrinos in the ice.

The concept of the D-Egg in more details is introduced in Section 1. In Section 2, the new optical module is simulated using GEANT4 [3] and the angular sensitivity is compared to the current IceCube. Measurements of the properties of D-Egg in the lab are also discussed. Next in Section 3, the gain of performance when using D-Egg is illustrated by simulating muons in the ice.

1. The concept of D-Egg

The current Digital Optical Module (DOM) in IceCube carries one $10''$ PMT (Hamamatsu R7081-2) looking down to the ice [4]. It has been proven to be reliable and with satisfactory performance. The D-Egg carries two $8''$ PMTs (Hamamatsu R5912-100) with one looking up and one looking down as shown in Figure 1.

One unique feature of D-Egg is that the depth of the glass varies along the latitude, being thickest at its equator and thinnest at the pole. The design of the thickness were carefully optimised for both requirements from optical performance and mechanical strength, which are usually contradicted to each other. The mechanical tolerance has been verified in the pressure vessel with P = 70 MPa, which is higher than the greatest pressure observed so far during the freeze-in process of the current IceCube. The diameter of D-Egg is 300 mm, which is 30.2 mm smaller than the current IceCube DOM and will reduce the drilling cost. The electronics and digital readout are modified based on the designs of the Gen2 baseline DOM [5].

Figure 1: The shape of D-Egg. The height of the glass is 534 mm and the diameter at the equator is 300 mm.

Another important characteristic of D-Egg is the enhancement of the efficiency for detecting UV photons. The emission spectrum of the Cherenkov radiation can be described by $1/\lambda^2$, therefore it is key for detectors to have high acceptance in the UV range. The absorption length of photons of different wavelengths varies with depth due to different optical properties of the ice layers. In the deepest clean ice, the absorption length of 380 nm photons is $\sim$ 200 m while it is only $\sim$ 40 m in the dust

layer. At the depth of ~ 400 m above the dust layer, the absorption length of photons of $\lambda \sim 350$ nm is 135 m, which is only 15 m shorter than photons of $\lambda \sim 400$ nm.

For the current IceCube DOM, the glass used to house the PMT absorbs 40% of photons with 350 nm. An improved type of glass has been chosen for housing D-Egg. By removing the iron contamination in the glass and reducing the thickness by 0.27 cm, over 95% photons of 350 nm pass through the glass vertically at the pole. A new type of gel has been used and the thickness remains the same with the current DOM. The transmittance is shown in Figure 2(a).

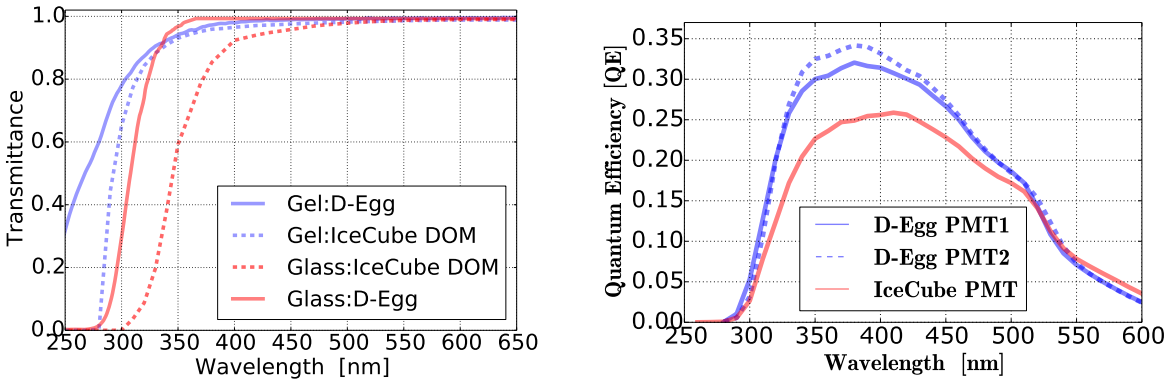

(a) (b)

Figure 2: (a) Transmittance of glass and gel for photons with different wavelengths for the current IceCube DOM and D-Egg. (b) The comparison of Quantum Efficiency (QE) of the current IceCube 10″ and the D-Egg 8″ PMT. The curves are from Hamamatsu measurements [6] without corrections for collection efficiency or charge response. It has also been proposed to use the high QE PMTs which are currently taking data in the DeepCore [7] for the next generation of IceCube. The DeepCore PMTs have similar QE with the 8″ PMTs in D-Egg.

The quantum efficiencies of the 8″ PMTs are higher especially at the UV range, as shown in Figure 2(b). At wavelength $\lambda = 380$ nm, QE is improved from 25% to $\sim 33\%$. The combined effect of using the new glass and PMT significantly enhance the detection of UV photons. In the next section, simulations of the photon propagation in the glass, gel and PMT are performed and the quantum efficiency of the detector is compared with measurements made in the lab.

2. Detector simulations and lab measurements

The geometry and optical properties of D-Egg have been implemented in GEANT4. Photons of wavelengths 300 nm to 650 nm were simulated in circular beams. The beams are rotated from the bottom to the top of the DOM and have a diameter of 0.534 m, which is the same as the height of D-Egg. The characteristics of the new PMTs measured in the lab, such as the charge response and the uniformity of the collection efficiency are included in the PMT simulations.

The effective area for all wavelengths and zenith angles for the IceCube DOM and D-Egg is shown in Figure 3. It is calculated as the ratio of the number of photoelectrons generated by the PMT over the number of incident photons. It is clear that the IceCube DOM is mostly sensitive to photons from below the DOM with zenith angle $\theta \geq 90^\circ$. On the other hand D-Egg has nearly

isotropic angular acceptance. At 340 nm, the effective area of D-Egg integrated over all angles is ~ 4 times the effective area of the spherical DOM.

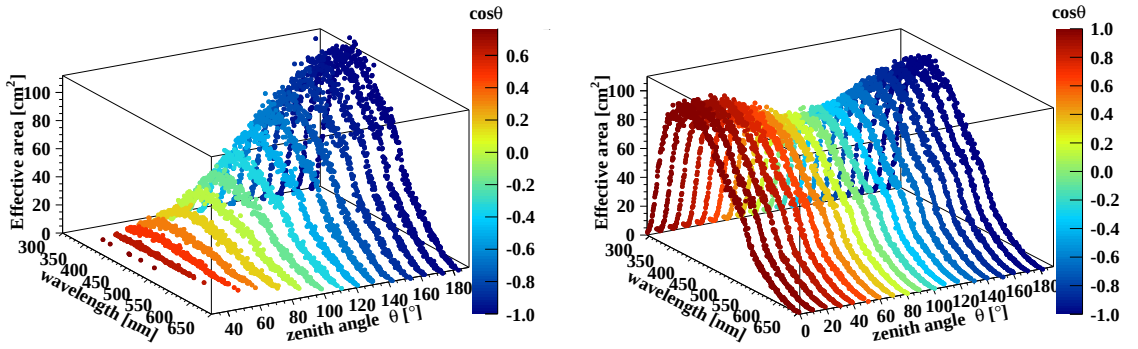

(a) (b)

Figure 3: The effective area of the current IceCube spherical DOM (a) and D-Egg (b). The optical properties of glass and gel have been implemented in GEANT4 simulations. The PMT simulations include the charge response correction, quantum and collection efficiencies. Each point scales with the probability of photon of certain wavelength and zenith angle being converted to photoelectrons.

It is important to verify the simulations using measurements in the lab. Figure 4 shows the setup in the lab for measuring the quantum efficiency of D-Egg in a freezer. Five LEDs (340, 365, 470, 520, 572 nm) are used as light sources. A fraction of the photons are split from the beam and goes to a small (monitor) PMT that has well-known gain. The ratio of reflection over transmission for the beam splitter is measured for each run. One could estimate the number of photons reaching the big PMT by scaling the number of photons observed via the small PMT.

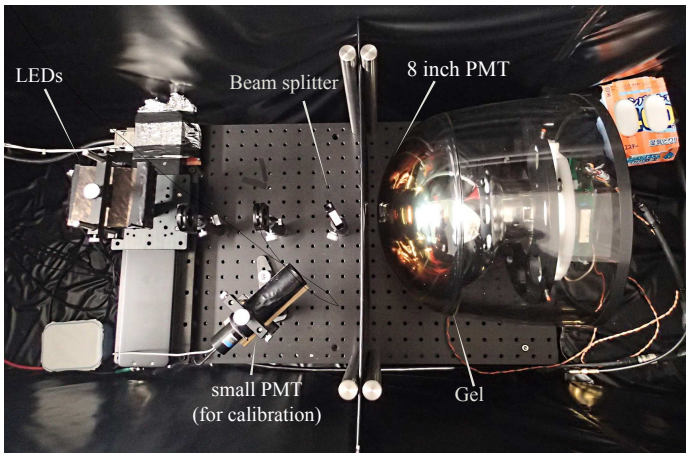

Figure 4: Lab setup for measuring quantum efficiency of D-Egg (with glass and gel) in the freezer. There are five LEDs contained in the wooden box on the left. The position of the LEDs are shifted using an automatic base so that the measurements will not be disturbed when the freezer is closed.

The quantum efficiency of the bare PMT was measured first and is about 90% of the Hamamatsu result due to the absence of the charge response correction. With taking into account the

glass and gel, D-Egg has a wavelength acceptance at 350 nm of nearly 26%, which is 13% higher than that of the current IceCube DOM. A comparison between lab measurements and simulations for D-Egg is shown in Figure 5.

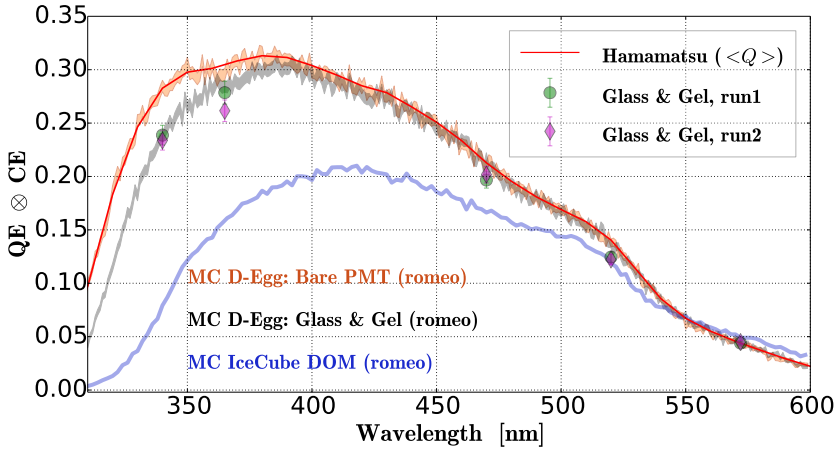

Figure 5: Comparisons of quantum efficiency measured in lab and simulations. The simulations are based on GEANT4 and romeo. Bare-PMT simulation is compared with Hamamatsu measurements which have been corrected for charge response. The blue curve shows the simulated efficiency when photons hit the centre of the photocathode of an IceCube DOM.

It has been demonstrated that D-Egg has great advantages on angular sensitivity and UV photon-detections. In the next section, the importance and improvement of using D-Egg is shown by looking at physics events using muon simulations.

3. The physics case of using D-Egg

Atmospheric muons are a tricky background for neutrino searches and it is vital to identify them. The improvements of angular and UV photon sensitivity using D-Egg ultimately provide additional information on physics processes in the ice, which are useful for rejecting muon backgrounds and reconstructing the event geometry. In this section, first an example of muon event is shown to illustrate the importance of having the up-looking PMT, followed by a discussion of how the veto could be improved using D-Egg.

3.1 An example of a muon event

A down-going muon with zenith angle 50° is shown in Figure 6(a). The Monte Carlo energy of the muon is 4 TeV and 540 GeV is lost through bremsstrahlung. The energy loss was very close to the DOM ($\sim$ 20 m) and photons experience few scatterings. The emitted photons are in the forward direction of the track and a large fraction hit directly on top of the DOM 60, which is located at the bottom level on string 41. The muon only develops at a 'corner' of the IceCube detector and partly contained.

The larger the distance, the more scatterings the photons go through so that the zenith angles become more homogeneous. Due to the short distance, the average number of scatterings for photons arriving on DOM 59 and 60 is about 5, which means these photons nearly do not change

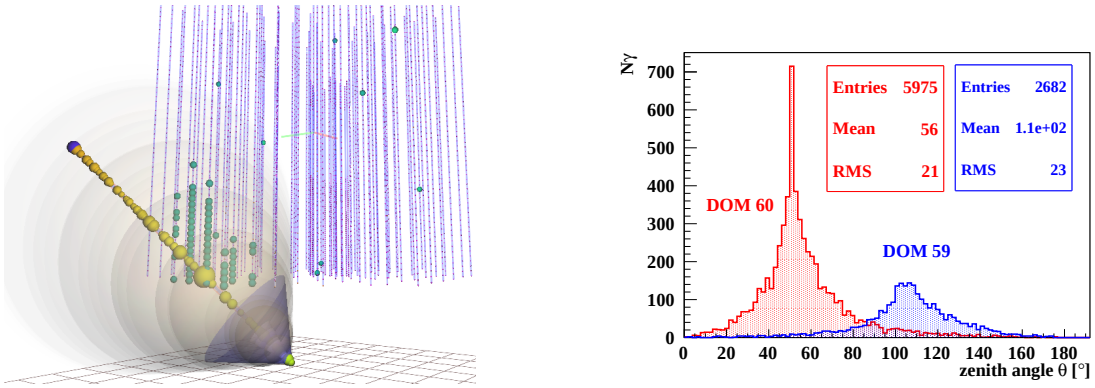

(a) (b)

Figure 6: (a) The example event that has DOMs close to an energy loss of 540 GeV through bremsstrahlung. DOM 59 and 60 are on string 41 with DOM 59 above DOM 60. Photons undergo ~ 5 scatterings and a huge fraction of them arrive on the top of DOM 60 (zenith angle smaller than 90°). (b) Distribution of zenith angle for photons when arriving on DOM 59 and 60. The angles are results of post-scatterings.

the direction of propagations. The distribution of zenith angle for each photon arriving on DOM 59 and 60 is shown in Figure 6(b). As expected DOM 60 receives majority of photons from the top and DOM 59 receives most photons from the bottom of the detector.

Photons hitting the top of the DOMs with $\theta = 50°$ have low probability of being detected by the IceCube DOM (Figure 3(a)). The number of photons which hit the DOMs as a function of the in-ice depth is shown in Figure 7 (left). The simulation was done by tracing each Cherenkov photon using GEANT4. Once the photons arrive at the DOMs, they are passed on to the detector simulation of IceCube DOM and D-Egg in parallel. The distribution of photoelectrons is shown in Figure 7 (right) for both D-Egg and IceCube DOM.

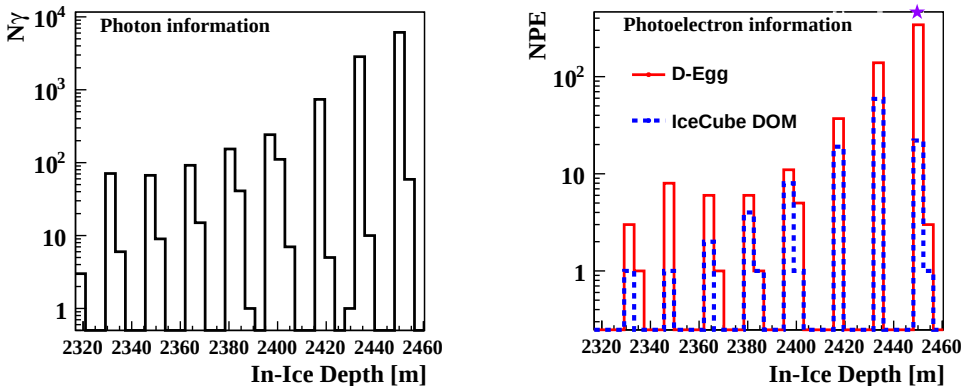

Figure 7: Left: The photon profile as the muon travels through the ice. The event happened close to the bottom layer of the ice. Only photons that arrive on the DOMs are counted. Right: The photoelectron profile as detected by D-Egg and IceCube DOM. 'NPE' stands for number of photoelectrons. The gaps between the depths are due to the distance intervals between DOMs on the strings.

The number of photoelectrons generated in DOM 60 is highly suppressed in the case of the IceCube DOM. The depth of DOM 60 is marked as a star. It is evident from Figure 7 that the photon

profile of this event can only be reproduced by using the photoelectron information provided by D-Egg. The photoelectron map from the IceCube DOM is inaccurate, which could have serious impacts on the interpretation of the zenith angle and the energy of the event. More studies regarding this issue have been planed in the future with dedicated simulation samples.

3.2 Potential for improving self-veto

One of the popular methods to reject muon backgrounds is to count the number of photoelectrons on the outer layer of DOMs. In such way neutrinos that have vertex inside the detector are selected. The background muons come from the atmosphere and in principle generate Cherenkov photons hitting the top of the DOMs, which is not ideal for the down-looking PMTs. However, photons are scattered in the ice and eventually the angular distributions become more isotropic unless the DOMs are close to the interaction points and direct light reaches the DOM. To understand how D-Egg could help for self-veto [8], single-muon events are simulated with energies from 100 GeV to 10 TeV.

Typically for the current IceCube the ice in the holes has different optical properties compared with the ice between the strings [9]. The scattering length is much shorter than that in the bulk ice due to the drilling process. However, for the Gen2 upgrade more precautions [1] will be made and one expects much clearer ice in the holes. Therefore for simulations included in this study, the hole ice is considered as the same with the bulk ice. Vertical muons with $\theta < 40^\circ$ are selected. Figure 8 shows the distribution of zenith angles of the photons that hit the DOMs for all the selected 1052 events.

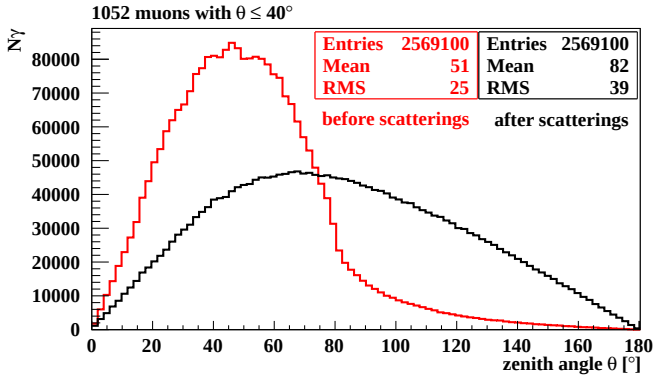

Figure 8: Distribution of zenith angles of the photons that arrive on the surface of the DOMs. The red curve shows the angles at emission. The black curve shows the angles after photons travel in the ice and scatter. The results are the sum of 1052 down-going muons.

After multiple scatterings, the number of photons that are down-going are still higher than those up-going. The ratio is $\sim 1.5:1$. We then select a set of through-going muon tracks, which are the majority of the background. Events penetrating the detector instrumentation volume by more than 950 m are included. The photon profile is shown in Figure 9 (left).

The total number of photoelectrons of D-Egg is more than 3 times the NPE value of the IceCube DOM for down-going muons (Figure 9 right). This shows the potential of decreasing the veto volume to gain more effective area for the neutrino searches.

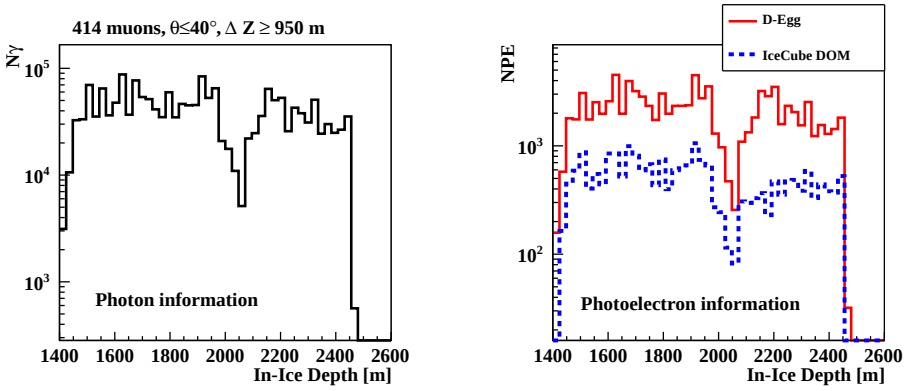

Figure 9: Left: Photon profile for the 414 down-going muons that went through the detector volume vertically. Only photons that arrive on the DOMs are counted. Right: Photoelectron profile of the 414 events detected by D-Egg and IceCube DOM. The dip in the middle is due to dust layer of the ice where the absorption length of photons are small.

4. Summary

The D-Egg has been introduced. A DOM with more UV-transparent glass and two PMTs improves the angular sensitivity and the acceptance of Cherenkov photons. By using signal and timing information from two PMTs, we expect it will be possible to reconstruct the event zenith angle and energy with smaller uncertainty and also to increase the effective area of down-going neutrino search.

Acknowledgments

The authors would like to thank Satoshi Shimizu from Nippon Marine Enterprises, for his great input on the glass design and mechanical tests.

References

[1] M. G. Aartsen *et al.* (**IceCube-Gen2** Collaboration), IceCube-Gen2: A Vision for the Future of Neutrino Astronomy in Antarctica, (2014)

[2] M. G. Aartsen *et al.* (**IceCube-PINGU** Collaboration), Letter of Intent: The Precision IceCube Next Generation Upgrade (PINGU) (2014)

[3] S. Agostinelli *et al.* (**GEANT4** Collaboration), Nucl. Instrum. & Meth. **A506** 250 (2003)

[4] R. Abbasi *et al.* (**IceCube** Collaboration), Nucl. Instrum. & Meth. **A618** 139 (2010)

[5] M. G. Aartsen *et al.* (**IceCube-Gen2** Collaboration), Generation 2 IceCube Digital Optical Module and DAQ, these proceedings, PoS(ICRC2015)1148 (2015)

[6] Hamamatsu Photonics K.K., Photomultiplier Tubes: Basics and Applications, third edition (2006)

[7] M. G. Aartsen *et al.* (**IceCube** Collaboration), Astropar. Phys. **35** 10 (2012)

[8] M. G. Aartsen *et al.* (**IceCube** Collaboration), Science **342** 1242856 (2013)

[9] M. G. Aartsen *et al.* (**IceCube** Collaboration), Nucl. Instrum. & Meth. **A711** 73 (2013)

PROCEEDINGS OF SCIENCE

PINGU Camera System to Study Properties of the Antarctic Ice

The IceCube-Gen2 Collaboration[1],

[1] *http://icecube.wisc.edu/collaboration/authors/icrc15_gen2*

E-mail: debanjan.tifr@gmail.com

IceCube is the world's largest neutrino detector located at the geographic South Pole, that utilizes more than 5000 optical sensors to observe Cherenkov light from neutrino interactions. A hot water drill was used to melt holes in the ultra-pure Antarctic ice, in which strings of optical sensors were deployed at a depth of 1500 m to 2500 m. The recent discovery of high energy neutrinos consistent with being of astrophysical origin, as well as precision measurements of neutrino oscillation parameters and competitive searches for dark matter, have demonstrated the great potential for ice-based neutrino telescopes. Extensions to the IceCube detector are under active consideration, including the PINGU multi-megaton neutrino detector with GeV threshold. Ice properties, including the refrozen ice from the optical sensor deployment, represent a major source of uncertainty for event reconstruction in IceCube. A camera system integrated with optical sensor modules could be tremendously beneficial for the interpretation of calibration measurements and to better understand ice properties. We describe a preliminary design of an on-board camera system and its impact on ice property measurements and geometry calibration.

Corresponding authors: D. Bose[1]*, M. Jeong[1], W. Kang[1], J. Kim[1], M. Kim[1], C. Rott[1]

[1]*Department of Physics, Sungkyunkwan University, Suwon 440-746, South Korea*

The 34th International Cosmic Ray Conference,
30 July- 6 August, 2015
The Hague, The Netherlands

*Speaker.

1. Introduction

IceCube, the world's largest neutrino telescope, utilizes the ultra-pure Antarctic ice at the geographic south pole as a detector medium. The recent discovery of high energy astrophysical neutrinos [1] by IceCube as well as a variety of other high impact results in the fields of astrophysics and particle physics have proven the success of the detector concept. Extensions to the IceCube detector, in form of a multi-megaton precision neutrino detector with an energy threshold of about a GeV, known as the Precision IceCube Next Generation Upgrade (PINGU) [2], and a high-energy neutrino detector optimised for observing TeV to PeV neutrinos, known as IceCube-Gen2 [3], are being considered. The extensions will reuse the very reliable design of IceCube's digital optical models (DOMs). Several improvements are considered, among them is an on-board camera system to survey the ice surrounding the optical sensors. In this proceedings we focus on the camera system for PINGU, which could be a key to reduce systematic uncertainties on light propagation in the ice and aid in achieving the primary physics goals of measuring the neutrino mass hierarchy and searching for dark matter.

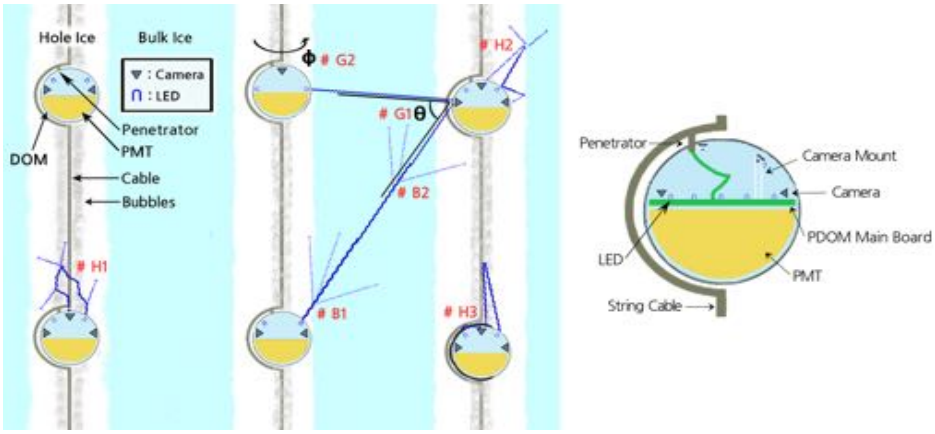

Figure 1: Left: Schematic drawing to illustrate potential camera measurements: (#H1) Hole ice survey. (#H2) Mapping of hole shape. (#H3) Cable position and orientation. (#B1) Light transmission and scattering at hole ice - bulk ice interface. (#B2) Light attenuation and scattering in the bulk ice. (#G1) Orientation of camera DOM. (#G2) DOM geometry. **Right:** Potential camera positions in the DOM. Details of the measurements are described in Table 1 and text.

Like IceCube, PINGU would detect neutrinos via Cherenkov light emission from secondary particles generated when a neutrino interacts in the deep Antarctic ice. Reconstruction of neutrino induced events depend strongly on the accurate modeling of the light propagation in the ice. A multitude of calibration devices including LED flashers, retrievable laser systems in the drill holes, two bright calibration light sources called the Standard Candles and a special device camera, have resulted in detailed understanding of the ice. The LED flashers, which are twelve radially outward pointing 405 nm LEDs on each DOM, are indispensable for the most advanced models of ice properties, as they provide calibration points through-out the detector. Fits to their data have resulted in the most advanced ice model [4]. The present calibration system however has several short comings, in particular little is known about the individual environment surrounding each DOM. The

Objective	Measurement	Requirements for Camera System		
		Resolution	Sensitivity	Orientation
#H1 Hole ice survey	Diffusion from bubbles and impurities	5 MP	0.1 lux	up
#H2 Hole ice mapping	Scattering on hole /bulk ice interface	1 MP	0.1 lux	sidewise
#H3 Cable position	Shadow and reflections of cable	1 MP	0.1 lux	up
#B1 Hole/bulk interface	Scattering / light transition	5 MP	0.001 lux	sidewise
#B2 Scattering and absorption lengths	Light attenuation and scattering halo	5 MP	0.001 lux	sidewise
#G1 PDOM orientation	LEDs from adjacent string PDOMs	1 MP	0.001 lux	sidewise
#G2 PDOM geometry	Triangulate positions, PDOM distances via separation angle	5 MP	0.001 lux	sidewise

Table 1: Objectives of the camera system are listed in the first column and measurements in the second column. Requirements for the camera system to carry out those measurements are given in columns 3-5, based on preliminary calculations. Orientation describes if the camera would be facing sidewise or up. Camera resolution in megapixels (MP) and sensitivities are estimated, in order to detect scattered light from bright LEDs (2 cd) located in PDOMs on the same or adjacent string. Objectives are grouped by hole ice studies (#H1, #H2 & #H3), light propagation in the bulk ice (#B1 & #B2), and geometry calibration measurements (#G1 & #G2).

refrozen ice in the drill hole is not very well understood and there is good reason to expect that the environment of each DOM could be significantly different. A low cost, high resolution on-board camera system paired with a bright LED for illumination deployed on each PINGU DOM (PDOM) could tremendously improve our understanding of the refrozen ice in the drill hole. It could yield qualitative information valuable in interpreting other calibration measurements, such as the LED flashers, and provide quantitative measurements of the ice properties.

A camera system inside two glass spheres at the bottom of IceCube string 80 (the last deployed string) provides a precedent for the proposed system. The camera observed the formation of bubbles at the centre of the drill hole (referred to as bubble column) during the refreezing of the ice from the outside inward [5]. The bubble column shows significantly reduced scattering length. Impurities settling on the surface of glass sphere of the camera were observed. However, information about the ice and drill hole provided by the camera is limited to a small region where it is located.

2. Objectives and Goals

The main goal of the camera system is to study the properties of the refrozen ice, determine the location and orientation of the PDOMs within the drill hole and survey the ice environment. A variety of measurements could be performed, each of which comes with its own requirements on camera positioning, sensitivity, field of view (FOV), resolution, and illumination options. We describe the suite of potential measurements qualitatively and derive basic requirements for the camera system to perform them.

(1) The camera system could monitor the freeze-in process of the strings of PDOMs deployed after melting holes using a hot water drill [6]. Little is known about the refreezing process. For

the measurement the camera would be operated at $0°C$, and would preferentially be facing up or sidewise. A high-resolution color camera could best identify impurities and monitor the freeze-in dynamics. Triboluminescence or the formation of cracks could potentially be observed. For PINGU it has been proposed to degas drill water in an effort to reduce or eliminate the formation of bubbles. The camera system could provide immediate feedback about water quality and the effectiveness of degassing, including depth dependence of bubble formation.

(2) Surveying the completely refrozen drill hole is one of the highest priorities of the camera system. If present, the system would survey and characterize the bubble column and identify contaminants. The PDOM position (x-y) within the drill hole can be determined, as well as the relative location of the bubble column, which could lead to a non uniform photon acceptance by PMT. For the hole ice measurement it is most effective to have the camera pointing up and to have a LED for illumination located adjacent to it on the same PDOM.

(3) Another objective is to study properties of the untouched or pristine ice (referred as 'bulk ice') between holes, and how light transmission is affected at the hole ice - bulk ice intersection. The observation of a halo of scattered light from a LED on an adjacent string could be used to study scattering, while the observation of the LED itself could be used to study attenuation. A high-resolution, high-sensitivity black and white camera would be most desirable for this purpose.

(4) A camera system could also assist geometry measurements. By observing a LED, on the adjacent upper PDOM, the relative orientation (around the z-axis) of the PDOM with an upward facing camera can be determined. The orientation of a PDOM on an adjacent string could also be determined through the observation of one or more LEDs on it, this would require a high resolution camera that could resolve individual LEDs on an adjacent PDOM. From the light pattern in the captured image, one can determine relative orientation of the camera PDOM as well. Likewise, a camera system facing up would capture scattered light coming from LEDs in the neighbouring PDOM in the same string and studying the light pattern we can determine relative orientations between PDOMs and their positions inside the hole. The relative depth of PDOMs between adjacent strings could also be determined. All these information would improve the geometry calibration of the PINGU array, but would require precise alignment and placement of LEDs and cameras.

(5) Finally the camera system could be beneficial to survey the PDOM environment for anything unforeseen and also provide a way to check for any dynamic effects, which are not expected after freeze-in.

Nearly all measurements benefit from a large FOV, making fisheye lenses the preferred option. Further, PINGU's hexagonal deployment pattern makes in necessary for sidewise facing cameras to have a FOV of $60°$ to have at least one adjacent string visible. Cameras should preferably have high resolution and good light sensitivity to observe LEDs on adjacent strings.

A schematic diagram of PDOMs in the hole ice along with probable camera positions are shown in the Figure 1. A summary of objectives, measurements and requirements based on some preliminary calculations are given in the Table 1.

3. Camera Design and Interface

The camera system would consist of one or more upward or sidewise facing cameras along with one or multiple bright LEDs with a narrow beam angle ($\sim 20°$) as light sources. The camera system

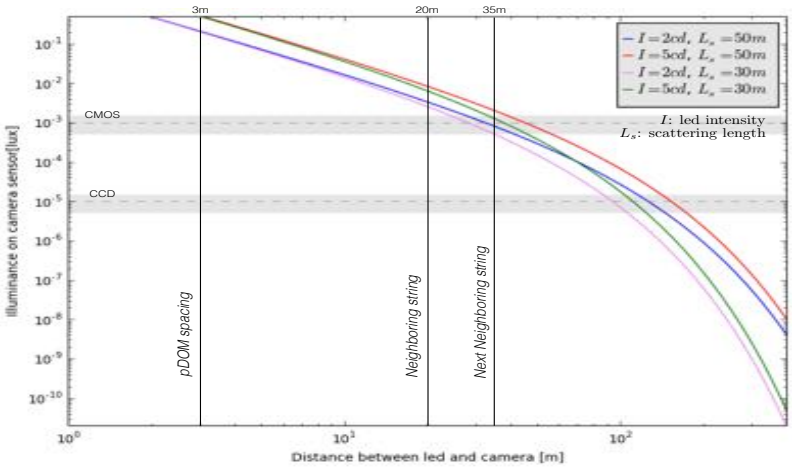

Figure 2: The minimum illumination required to observe an LED located in the neighboring PDOM in the same string and at adjacent string are shown. The grey shaded area show the illumination for a CMOS camera with at 1 s exposure time and CCD camera sensitivities as specified by the manufacturer for an exposure time 1/60 s.

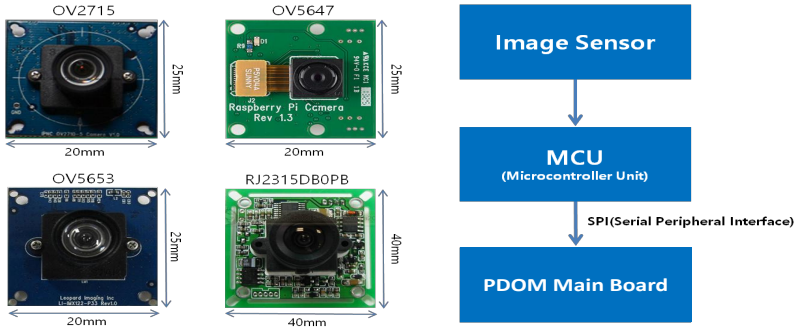

Figure 3: Left : Camera modules currently being tested include CMOS sensors OV2715, OV5647 & OV5653 and CCD sensors RJ2315DB0PB. **Right :** Block diagram for the camera interface.

would be either mounted on the PDOM main board or attached to the penetrator of the pressure sphere for easy assembly. As shown in Figure 3, the camera module would be mounted on a small ($\sim$ 40mm$\times$40mm) Printed Circuit Board along with a MCU (Micro Controller Unit) for image processing and communicate with the mainboard via SPI (Serial Peripheral Interface).

The camera system would remain in power saving mode during physics data taking and only be activated for calibration runs. The targeted power consumption per the camera system during operations is less than 1 W as the total power available per quad (4 PDOMs connected together) is $\sim$2.5 W. While PDOMs (PMT) will be off during camera operations it is desirable to have multiple cameras and LEDs active to minimize time for calibration measurements. Following image capture, uncompressed images would be transferred to the PDOM mainboard and then through the IceCube coaxial cable at 40kB/s per PDOM to the surface, where they would be saved for offline analysis.

4. System requirements

Various CMOS and CCD camera modules are considered as candidates for the camera system. Currently we are studying three CMOS cameras & one CCD camera (see Figure 3). All the cameras have manufacturer specified operation temperatures down to -30°C. A lens with wide field

of view can be mounted on the camera sensor. One of the requirements for the camera system is that it has a low power consumption, which favours CMOS cameras ($\sim$ 0.3 W). Further CMOS sensors are inexpensive and have high resolution. CCD cameras on the other hand have significantly higher sensitivities, but also consume more power ($\sim$ 1.0 W) and have a lower resolution. The candidate CMOS and CCD cameras have resolutions of 2 MP-5 MP, and 0.3 MP, respectively.

To minimise detector downtimes for calibration measurements, a camera with higher light sensitivity is preferred. However, some measurements might require high resolution (if not limited by image distortion in the glass sphere) and power constraints might favor the CMOS camera. For the moment we consider both CCD and CMOS cameras as candidates.

Longer exposure times with the CMOS camera might achieve similar sensitivities to CCD cameras. CMOS cameras are expected to be operated in their most sensitive settings if noise levels are sufficiently low. The light sensitivity of a digital camera can be set through the ISO (International Standards Organization) number (i.e. higher number corresponds to higher sensitivity). Figure 2 shows the required illumination at the camera to see a typical bright LED ($\sim$ 2-3 candela) as a function of distance. The required illuminance to observe a LED on the neighbouring DOM in the same string and in the adjacent string are around 0.1 lux and 0.001 lux respectively.

5. Camera measurements at the lab

We describe the camera performance measurements that will be our basis for the camera selection. We have setup measurements to compare and characterize: (1) camera noise, (2) light sensitivity, and (3) camera resolution and image distortion due to the glass sphere. Currently we have surveyed one CMOS camera (OV5647) to develop the series of tests that will be used for camera selection. Our current sample camera has 5 million pixels (2592×1944) and is currently operated through a Raspberry Pi for convenience. We obtained raw images in Bayer format. A Bayer filter is a RGB (Red, Green & Blue) color filter array on a square grid of photosensors. Each primary color red, green & blue has 8 bits, which means counts will go in saturation at 255 counts.

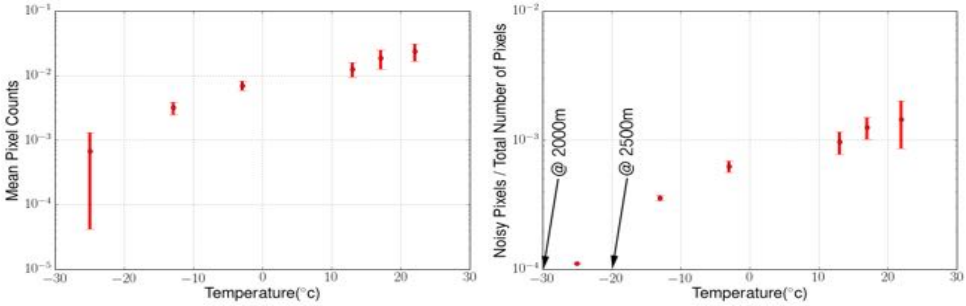

Figure 4: Left: Mean noise count per pixel as function of temperature for OV5647 for ISO 800 and 6s exposure. **Right:** The number of noisy pixels vs temperatures. Temperatures at depths 2000 m and 2500 m are indicated with arrows.

Camera Noise : A low brightness camera measurement might be limited by intrinsic detector noise, hence we characterise noise and stability under the expected conditions in the deep ice. We measured dark noise at room temperature in a dark box and at low temperatures in a freezer. Images were captured with exposure times of up to 6 seconds and for ISO 100, 400, and 800. Camera noise

increases with exposure time and sensitivity setting (ISO value). At room temperature about $\sim 1\%$ of pixels are noisy, showing one or more counts. The number of noisy pixels (both fixed pattern and random) and average count per pixel decreases significantly with temperature (see Figure 4). In the deep ice at 2500 m ($-20°C$) to 1500 m ($-45°C$) noise is expected to be sufficiently low.

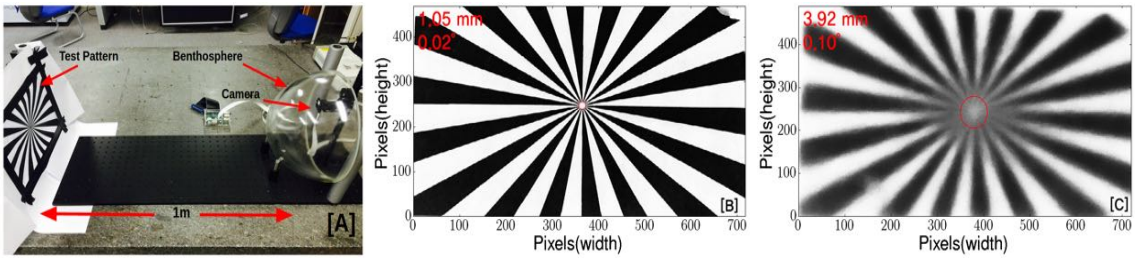

Figure 5: [A] Setup to study image distortion due to the Benthosphere. Image without [B] and with [C] Benthosphere. Red circles indicate the region where line patterns cannot be distinguished.

Image Resolution and Distortion: As the camera would be located inside the PDOMs pressure glass sphere (Benthosphere), images are bound to be distorted. We measure image resolution under normal conditions and through the Benthosphere. As the resolution measurement is subjective, we are investigating different independent ways to measure it. As an example we show a test pattern measurement shown in Figure 5. In the test pattern black and white lines originate in the center and radiate outward. We captured images of the test pattern at 1 m distance from the camera with and without the Benthosphere. The relative effect of image distortion can clearly be seen in image [C] in Figure 5. The line pattern cannot be distinguished inside the red circles in plots [B] & [C]. As the camera under test has a FOV of 60°, by measuring the diameter of the circle we can determine the resolution. We find the resolution of the camera without the Benthosphere to be $\sim$1.05 mm (0.024°) and with $\sim$3.92 mm (0.10°) at 1 m distance. The Benthosphere reduces the resolution by a factor of 4. Optical gels or optimised positioning could reduce this effect. Further we note that due to refraction in ice the angular resolution will improve by $n_{ice}/n_{air} \simeq 1.3$ and a camera FOV of 60° will be reduced to 45°.

Sensitivity of the camera: To study camera sensitivity, we illuminate the camera sensor uniformly (homogeneous within 5%) as shown in Figure 6. The camera is operated in different sensitivity settings defined by the product of analog and digital gain. For OV5647 gains are auto adjusted if the camera is near saturation. To increase the cameras dynamic range counts show a logarithmic behaviour for large exposure times and illuminations. A linear behaviour can be seen for low pixel count rates as shown in Figure 6. The pixel count rates determined at room temperature for 1 s exposure are 158 ± 12 counts/lux, 78.4 ± 5.0 counts/lux, and 20.6 ± 0.5 counts/lux for ISO800, 400, and 100, respectively. We verified that count rates are independent of temperature, with -25°C being the lowest measured temperature so far. We compare the observed rates, S, with the camera dark noise, N, to determine its sensitivity. We define the sensitivity as S/N$\sim$10. At -25°C the N=0.001 counts, which results in a sensitivity of 6×10^{-5} lux at ISO800 and 1 s exposure. If we require at least one pixel count an intensity of 0.006 lux is found. As seen in figure 2, the required luminance to see a bright LED ($\sim$ 2 cd) in the neighboring string at 20 m distance is 0.001 lux. Hence, LEDs on adjacent strings will be observable with few seconds exposure times.

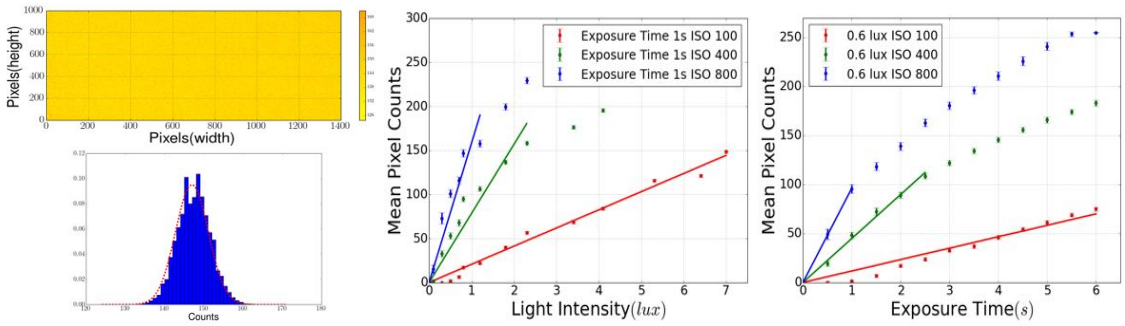

Figure 6: Pixel counts for uniformly illuminated sensor (left). Mean pixel counts for different camera sensitivities as function of the light intensity (middle) and exposure time (right).

6. Conclusions

Low-cost high resolution cameras integrated with the optical module design for IceCube upgrades would be tremendously helpful in understanding the ice environment of the sensors. The systems could survey the refrozen ice in the drill hole, aid geometry measurements, and study ice properties. Cameras could assist the effort to help reduce uncertainties on detection and light propagation in the ice and hence help achieve PINGUs and IceCube-Gen2 physics objectives faster and even benefit IceCube analyses. We have set up a framework to study cameras under conditions, similar to those encountered in the ice, and reported results for camera candidate OV5647. Under idealised conditions the camera is found to be sufficient to carry out the proposed measurements. We have started ray-tracing simulations with GEANT4 to better determine camera system requirements and will comprehensively compare different candidate modules. We are designing a prototype for integration tests. In the future we will also consider stereoscopic camera pairs and expand tests to include B&W cameras, that could be illuminated with RGB LEDs to compose color images.

References

[1] IceCube Collaboration, *Phys. Rev. Lett.* **113**, 101101, (2014) ; IceCube Collaboration, *Science* **342**, 1242856, (2013).

[2] IceCube-Gen2 Collaboration, *K. Clark et al.*, *These proceedings paper*, **1174**, (2015) ; IceCube-PINGU Collaboration, *M. Aartsen et al.*, [arXiv:1401.2046].

[3] IceCube-Gen2 Collaboration, *E. Blaufuss et al.*, *These proceedings paper*, **1146**, (2015) ; IceCube-Gen2 Collaboration, *M. Aartsen et al.*, [arXiv:1412.5106].

[4] IceCube Collaboration, *Nuclear Instruments and Methods* **A711**, 73-89, (2013).

[5] Per Olof Hulth, *Results from the IceCube video camera system at 2455 meters ice depth*, *Very Large Volume Neutrino Telescope Workshop*, **325**, (2013).

[6] Francis Halzen and Spencer R. Klein, *Review of Scientific Instruments* **81**, 081101, (2010).

PROCEEDINGS OF SCIENCE

The IceCube-Gen2 High Energy Array

The IceCube-Gen2 Collaboration[†]

[†] *http://icecube.wisc.edu/collaboration/authors/icrc15_gen2*

E-mail: blaufuss@icecube.umd.edu

Given recent observations of an astrophysical flux of neutrinos by the IceCube neutrino observatory, design studies for a next generation Antarctic neutrino observatory are well underway. The IceCube-Gen2 high-energy array will instrument a $\sim 10\,\mathrm{km}^3$ volume of clear glacial ice at the South Pole to deliver substantially larger astrophysical neutrino samples of all neutrino flavors. This detector would support a rich physics program, including a search for point sources, a detailed spectral and flavor characterization of the astrophysical neutrinos, searches for cosmogenic neutrinos, studies of cosmic rays, and searches for signatures of beyond-the-standard-model neutrino physics. This contribution highlights the detector sensitivity and geometry optimization studies performed during the design process. Astrophysical neutrino sensitivity can be increased by the addition of an extensive surface detector to identify and reject atmospheric backgrounds originating from the southern hemisphere. This large detector, in combination with the existing IceCube neutrino observatory and the rest of the IceCube-Gen2 facility will be the flagship experiment of the new field of neutrino astronomy.

Corresponding authors: E. Blaufuss[*1], C. Kopper[2], C. Haack[3],

[1] *Department of Physics, University of Maryland, College Park, MD, USA*

[2] *Department of Physics, CCIS 4-181, University of Alberta, Edmonton, Alberta T6G 2E1, Canada*

[3] *III. Physikalisches Institut, RWTH Aachen University, D-52056 Aachen, Germany*

The 34th International Cosmic Ray Conference,
30 July- 6 August, 2015
The Hague, The Netherlands

[*]Speaker.

1. Introduction

High-energy neutrinos are unique in their ability to probe the extreme universe. Neutrinos reach the Earth from the edge of the universe without absorption or deflection by magnetic fields. They can escape from the deepest regions of cosmic accelerators where the highest energy cosmic rays are created. While these properties give them advantages over other astrophysical messengers such as photons and charged particles, their weak interactions make neutrinos very difficult to detect.

Detectors searching for these astrophysical neutrinos are built by instrumenting large natural liquid water or ice reservoirs to detect Cherenkov emission from the charged particles produced when the neutrinos interact with matter in or near the detector. The deep ice of the Antarctic glacier is host to IceCube [1], the first kilometer-scale neutrino observatory, which has recently reported an observed astrophysical neutrino signal [2, 3, 4, 5]. Proposed next-generation deep-water-based detectors include KM3NeT [6] in the Mediterranean sea and GVD [7] in Lake Baikal, both providing a complementary view of the sky to IceCube.

For an underground detector such as IceCube, the primary background is downward-directed muons created in cosmic-ray interactions in the Earth's atmosphere. These atmospheric muons trigger IceCube at a rate of ~ 3 kHz. Atmospheric neutrinos are collected at a rate of ~ 300 per day, have a mean energy of ~ 1 TeV and form an isotropic background in searches for astrophysical neutrinos. At energies in excess of ~ 100 TeV, the flux of atmospheric neutrinos is small, and upward-directed events of higher energy are likely of astrophysical origin.

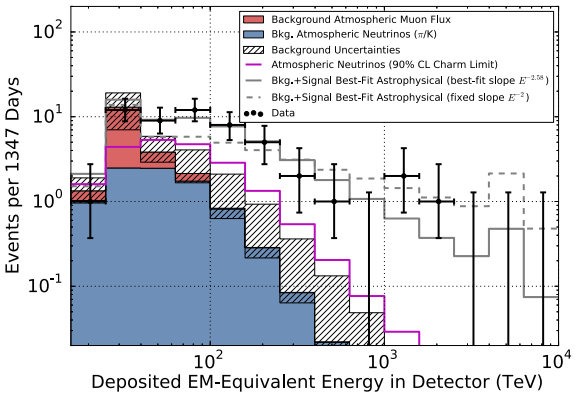

Figure 1: Deposited energies of contained events observed in 4 years of data in comparison to predictions. The hashed region shows uncertainties on the sum of all backgrounds. Muons (red) are computed from simulation to overcome statistical limitations in our background measurement and scaled to match the total measured background rate. Atmospheric neutrinos and uncertainties thereon are derived from models of both the π, K and charm components of the atmospheric spectrum that have been fitted to the observed data [2].

A robust method to identify neutrino events is to distinguish events that start inside the detector from those which enter from the outside, which can be done for neutrino events originating from the entire sky. A search using this veto technique has been successfully applied to 4 years of data from the IceCube detector [2, 8]. The 54 events found with deposited energies ranging from 30 TeV to 2 PeV clearly reflect a significant observation of astrophysical neutrinos. The deposited energy distribution for this sample, along with expected backgrounds and fits to signal hypotheses, is shown in Figure 1. An independent analysis of the spectrum of upward going muons arising from neutrinos passing through the Earth has confirmed the existence of the astrophysical component [9].

These modest sample sizes of astrophysical neutrinos represent the "first light" in the field of high-energy neutrino astronomy. With the present statistics, these astrophysical neutrino samples appear consistent with an isotropic, diffuse flux of neutrinos equally distributed between the three neutrino flavors. Additionally, all searches for individual galactic and extragalactic source candidates [10, 11, 12] have so far only resulted in upper limits.

The effectiveness of IceCube as a tool for neutrino astronomy over the next decade is constrained by the limited numbers of astrophysical neutrinos measured in the cubic kilometer array. In this paper we present a vision for the next-generation IceCube neutrino observatory, the *IceCube-Gen2* high energy array, which is an expanded array of light-sensing modules that instrument a $\sim 10\,\mathrm{km}^3$ volume for detection of high-energy neutrinos [13]. With its unprecedented sensitivity and improved angular resolution, this instrument will explore extreme energies (PeV-scale) and will collect high-statistics samples of astrophysical neutrinos of all flavors, enabling detailed spectral studies, significant point source detections and new discoveries.

2. Science Motivation

The observation of astrophysical neutrinos has raised as many questions as it has answered. These include searches for the origin of these events, a full characterization of the flux, spectrum and flavor composition of the neutrinos, searches for neutrinos arising from the GZK process, searches for signals in coordination with other observatories and messenger particles, and improved measurements of the cosmic ray flux that drives our primary backgrounds. A detector with a significant increase in instrumented volume would aim to answer these questions.

With no indication of a steady point source in the current data, IceCube is increasingly sensitive to rare transient events, where observation of a multiplet of events in a short time can yield a significant detection. Sensitivity gains to transient events grow quickly in a larger detector. A next-generation neutrino observatory with 5 times the point-source sensitivity of IceCube and otherwise similar detector performance is predicted to have an increased sensitivity to transient source densities and rates by about two orders of magnitude [14].

While spectral and flavor composition of the observed astrophysical neutrino events are consistent with a single power law and equal distributions between all neutrino flavors, better measurement of these quantities from an increased sample size would begin to probe the internals of the cosmic accelerators that generate these events. The neutrino production mechanisms ($p-p$, $p-\gamma$ interactions, or neutron decay) and details of magnetic fields in the source region all leave their imprint [13, 15] on the observed event sample. Additionally, galactic and extra-galactic components could be resolved independently.

Multi-messenger astronomy, the combination of observations of cosmic rays, neutrinos, photons of all wavelengths, and, in the near future, gravitational waves will represent a powerful opportunity to decipher the physical processes that govern the non-thermal universe. With its improved sensitivity, *IceCube-Gen2* will be a unique instrument to complement the next generation of telescopes. Neutrinos play a central role in multi-messenger astronomy, as they are an unambiguous signature for the acceleration and interaction of protons and nuclei. IceCube already has a long-standing coordinated observation programs with several instruments [16, 17, 18, 19].

The surface array IceTop [20] has proved to be a valuable component of IceCube. Accordingly, the Gen2 high-energy array would include a surface detector near the top of each deployed string. With a spacing of ∼250 m, such a surface array will provide a high-resolution measurement of the primary spectrum from 10 PeV to above one EeV. Most importantly, with the larger aspect ratio of the *IceCube-Gen2* high-energy array the acceptance for coincident events seen by both the surface array and the deep array increases by a factor of 40, from 0.26 km^{2}sr to $\sim$ 10 km^{2}sr. The ratio of the signal of ∼TeV muons in the deep detector to the size of the surface shower will allow an unprecedented measurement of the evolution of the primary composition in the region where a transition from galactic to extragalactic cosmic rays is predicted [21].

Astrophysical neutrinos at high energies are separable from atmospheric neutrinos by searching for other particles produced in the extended air shower that gives rise to these backgrounds. If high-energy neutrinos were produced in atmospheric air showers, they would likely be accompanied in the in-ice detector by muons produced in the parent air shower from which they originate. For 1 PeV down-going atmospheric neutrinos, where the expectation is a few events per year, this atmospheric in-ice self-veto would reject more than 99.9% of them by observing an accompanying muon in the deep detector in coincidence with the neutrino [22, 23]. Additionally, a surface array can also act as a veto for cosmic-ray and atmospheric neutrino backgrounds to high-energy neutrino searches in the deep detector. While IceTop provides a veto that covers only about 3% of the southern sky, the larger aspect ratio of the high-energy array would provide veto coverage to approximately 20% of the southern sky. Strategies are under study to extend the surface array beyond the footprint of the array [24, 25].

3. Design of a Gen2 High Energy Array

IceCube-Gen2 would build upon the existing IceCube detector infrastructure, and would take advantage of the very long absorption lengths found in the glacial ice at the South Pole to add additional instrumentation with significantly larger string separation distances [26]. Building this larger instrument would be achieved with a comparable number of strings used in the existing IceCube detector, and would target neutrino energies above $\sim$ 50 TeV with high efficiency.

While detailed studies toward a final design are ongoing, several design considerations are clear and understood. A detector sensitive to high-energy astrophysical muon, electron and tau neutrino flavors requires the correct combination of instrumented volume and projected surface area in all directions. This optimization is done by selecting larger string spacings, which increase the energy threshold as the instrumented volume increases, and by the geometrical arrangement of the deployed strings, which can trade detector instrumented volume for detector cross-sectional area. Detection of neutrino-induced muon track events will scale with the detector cross-sectional area, while the neutrino shower events produced by electron and tau flavors and neutral current interactions will scale with instrumented volume. Angular reconstruction performance, energy resolution and veto efficiency to astrophysical events are key metrics in the design study.

The most important aspect of a larger instrument in the glacial ice are the optical properties of the ice, in particular, the absorption length for Cherenkov photons. Typical absorption lengths are between 50 m and 200 m in the upper half of the detector, and often exceed 200 m in the lower half. Although the optical properties vary with the layered structure of the ice, the average absorption and

scattering lengths dictate the distance by which one can space strings of sensors without impacting the uniform response of the detector. Early studies indicate that spacings of $\sim 240 - 300\,\mathrm{m}$ are acceptable while maintaining high efficiency to astrophysical neutrinos.

The optical properties of the glacial ice prevent us from using optical modules at depths much shallower than the current instrumented range used by IceCube (with instrumented depths between 1450m and 2450m). Measurements of the depth dependence of the absorptivity of the Antarctic ice, Fig. 2, indicate that we will be able to extend the strings by $\sim 250\,\mathrm{m}$, leading to an increase in the geometric area for horizontal track events and therefore a 25% increase in effective area for such events.

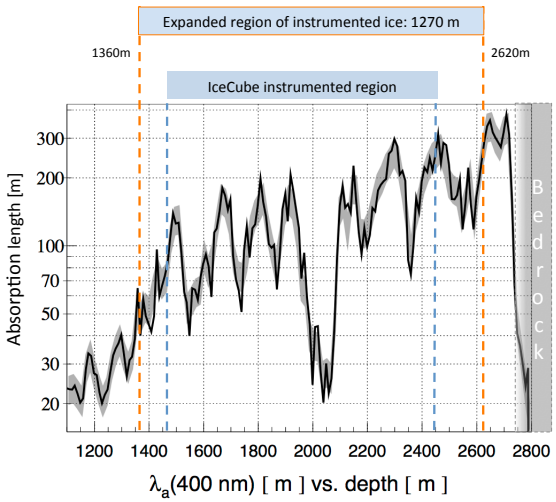

Figure 2: Absorption length in the glacial ice versus depth [26]. Note the layer of high dust concentration starting at about 2000m depth. The ice above and below that layer is very clear. The current instrumented depth range used in IceCube and an extended string length, adding about 260 m to each string are indicated. Note that not all simulations shown in this report have been performed with the extended string length.

To investigate the sensitivity of a larger detector, several benchmark geometries have been evaluated in software simulations, and are shown in Figure 3. These benchmark geometries use a non-regular grid pattern to avoid symmetries that deteriorate acceptance and resolution for muon tracks. They are compared to the IceCube detector in its completed 86 string configuration, and are used to scale sensitivities to a $10\,\mathrm{km}^3$ instrument. The projected areas of some of these geometries considered are compared to IceCube-86 in Figure 4. As the detector volume grows in these geometries, the exposed area increases and reaches up to $\sim 10\,\mathrm{km}^2$ area, substantially larger than the IceCube area.

For point source searches, which rely on muon tracks produced by charged current interactions of muon neutrinos in or near the instrumented volume, the sensitivity increases with the projected cross sectional area relative to source direction. At the energies of interest for astrophysical neutrino searches, these muons have ranges that routinely exceed 10 km, greatly extending the sensitivity of these searches. Point source sensitivities will scale approximately with the square-root of the increase in cross sectional area and linearly with the improvement in angular resolution. In scenarios where the atmospheric backgrounds are negligible (e.g. short transients or searches for sources of very high-energy neutrinos), sensitivities are expected to scale nearly linearly with cross sectional area.

These benchmark geometries have been used to study the potential gains in point source sensitivity. Improvements in track angular resolution and overall point source sensitivity will be presented at the conference.

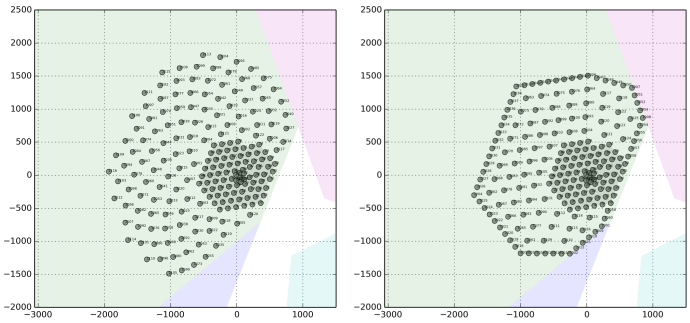

Figure 3: Example benchmark detector string layouts under study. Each expands about IceCube by adding 120 strings constrained to the South Pole "Dark Sector" (shaded in light green). For the left panel, uniform string spacing of $\sim 240\,\mathrm{m}$ is shown, and benchmark samples for $\sim 200\,\mathrm{m}$ and $\sim 300\,\mathrm{m}$ are also considered. The instrumented volumes are $6.0\,\mathrm{km}^3$, $8.0\,\mathrm{km}^3$, and $11.9\,\mathrm{km}^3$ respectively. The panel on the right represents a string layout with a denser edge weighting, where edge strings are spaced at $\sim 125\,\mathrm{m}$, while interior strings are spaced at $\sim 240\,\mathrm{m}$, with an instrumented volume of $6.2\,\mathrm{km}^3$.

A search for electron or tau neutrino interactions depends on observation of an electromagnetic or hadronic cascade resulting from the interaction of the neutrino with nucleons inside the instrumented volume. These neutrinos generally interact with nucleons in the ice via deep-inelastic scattering processes, but at $E_\nu \sim 6.3\,\mathrm{PeV}$ the resonant formation of an on-shell W^--boson, the so-called Glashow resonance [27], enhances the the cross-section for electron-antineutrinos. The resonance would be observable mostly as a peak in the cascade energy spectrum, and serves as a key tag for neutrino flavor in a larger detector. Benchmark detectors show increased rates proportional to the volume gains, with factor of $\sim$10 gains in observable Glashow resonance events. Given the similar event signatures for tau neutrinos, the same event rate gains in the larger detector are also found for tau neutrino events [13].

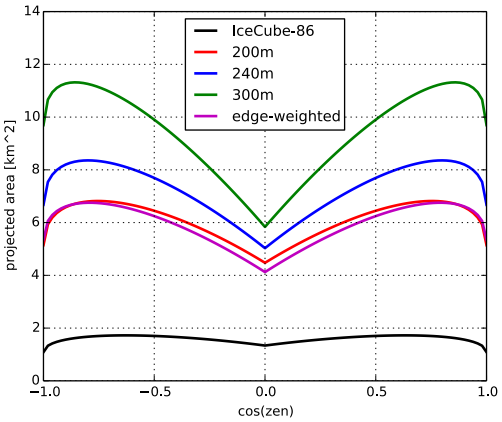

Figure 4: Instrumented area as a function of IceCube zenith angle for all benchmark configurations. To determine the geometric area, the detector volume containing all optical modules has been extended by 60 m on all sides. The figure legend also shows the instrumented volume of each detector, again with an extension of 60 m at the sides, top and bottom.

4. Realization

The proposed *IceCube-Gen2* high-energy array is envisioned to be the major element of a planned large-scale enhancement to the IceCube facility at the South Pole station. Members of the *IceCube-Gen2* Collaboration are working to develop proposals in the US and elsewhere that will

include this next generation IceCube high-energy neutrino detector and the PINGU sub-array [28] that targets precision measurements of the atmospheric oscillation parameters and the determination of the neutrino mass hierarchy. The facility's reach may further be enhanced by exploiting the air-shower measurement and vetoing capabilities of an extended surface array [24, 25] and potentially a radio-pulse neutrino detector to achieve improved sensitivity to neutrinos in the 10^{16}-10^{20} eV energy range, including GZK neutrinos.

A key for the successful scientific operation of IceCube has been the excellent reliability of the Digital Optical Modules (DOMs), hot-water drilling, DOM deployment operations [29] and data systems [30], which have resulted in stable data taking at more than 99% uptime. The instrumentation and drilling systems for *IceCube-Gen2* closely follow the demonstrated IceCube technologies, with targeted improvements for overall performance and new capabilities. While the *IceCube-Gen2* baseline DOM [31] keeps the robust structural elements of the IceCube DOM, a modern, more powerful set of electronic components are included into the design. In addition, DOM designs that utilize two large PMTs per DOM [32], multiple small PMTs per DOM [33], or wavelength-shifting and light-guiding techniques [34] are also being studied. The Enhanced Hot Water Drill design focuses on a modular system that will operate with higher efficiency and require less maintenance in routine operation. Both the instrumentation design (DOM, cable and readout) and deployment (EHWD) are shared with the PINGU low-energy array as part of the *IceCube-Gen2* infrastructure, providing significant reductions in cost and enhancing flexibility.

References

[1] Ahrens, J., et al., *Astropart.Phys.* **20** (2004)

[2] IceCube Coll., *Observation of Astrophysical Neutrinos in Four Years of IceCube Data*, PoS(ICRC2015) 1081, *These proceedings*

[3] IceCube Coll., *Update of a Combined Analysis of the High-Energy Cosmic Neutrino Flux at the IceCube Detector*, PoS(ICRC2015) 1066, *These proceedings*

[4] IceCube Coll., *A measurement of the diffuse astrophysical muon neutrino flux using multiple years of IceCube data*, PoS(ICRC2015) 1079, *These proceedings*

[5] IceCube Coll., *High energy astrophysical neutrino flux characteristics for neutrino-induced cascades using IC79 and IC86-string IceCube configurations*, PoS(ICRC2015) 1109, *These proceedings*

[6] Margiotta, A., *JINST* **9** (2014) C04020

[7] Avrorin, A.D, et al., *Nucl.Instrum.Meth.* **A742** (2014) 82

[8] Aarsten, M.G. et al., *Phys.Rev.Lett.* **113** (2014) 101101

[9] Aarsten, M.G. et al., *Submitted to Phys.Rev.Lett.*

[10] Aartsen, M.G. et al., *Astrophys.J.* **779** (2013) 132

[11] Adrian-Martinez, S. et al., *Astrophys.J.* **786** (2014) L5

[12] IceCube Coll., *Results of neutrino point source searches with 2008-2014 IceCube data above 10 TeV*, PoS(ICRC2015) 1047, *These proceedings*

[13] Aartsen, M.G. et al., *IceCube-Gen2: A Vision for the Future of Neutrino Astronomy in Antarctica*, [arxiv:1412.5106]

[14] Ahlers, Markus and Halzen, Francis, *Pinpointing Extragalactic Neutrino Sources in Light of Recent IceCube Observations*, [arxiv:1406.2160]

[15] Kashti, Tamar and Waxman, Eli, *Phys.Rev.Lett* **95** (2005) 181101

[16] IceCube Coll., *The Online Follow-Up Framework for Neutrino-Triggered Alerts from IceCube*, PoS(ICRC2015) 1069, *These proceedings*

[17] IceCube Coll., *Neutrino-triggered target-of-opportunity programs in IceCube*, PoS(ICRC2015) 1052, *These proceedings*

[18] IceCube Coll. et al., *Correlation between the UHECRs measured by the Pierre Auger Observatory and Telescope Array and neutrino candidate events from IceCube*, PoS(ICRC2015) 1082, *These proceedings*

[19] M. Santander et al., *Searching for TeV gamma-ray emission associated with IceCube high-energy neutrinos using VERITAS*, PoS(ICRC2015) 785, *These proceedings*

[20] Aartsen, M.G. et al., *Phys.Rev* **D88** (2013) 042004

[21] IceCube Coll., *Cosmic Ray Science Potential for an Extended Surface array at the IceCube Observatory*, PoS(ICRC2015) 694, *These proceedings*

[22] Schönert, Stefan and Gaisser, Thomas K. and Resconi, Elisa and Schulz, Olaf, *Phys.Rev.* **D79** (2009) 043009

[23] Gaisser, Thomas K. and Jero, Kyle and Karle, Albrecht and van Santen, Jakob, *Phys.Rev.* **D90** (2014) 023009

[24] IceCube Coll., *Simulation Studies for a Surface Veto Array to Identify Astrophysical Neutrinos at the South Pole*, PoS(ICRC2015) 1070, *These proceedings*

[25] IceCube Coll., *Motivations and Techniques of a Surface Detector to Veto Air Showers for Neutrino Astronomy with IceCube at the Southern Sky*, PoS(ICRC2015) 1156, *These proceedings*

[26] Aartsen, M.G. et al., *Nucl. Instr. Meth.* **A711** (2013) 73

[27] Glashow, Sheldon L, *Phys.Rev.* **118** (1960) 316

[28] IceCube Coll., *Status of the PINGU Detector* PoS(ICRC2015) 1174, *These proceedings*

[29] Abbasi, R. et al., *Nucl.Instrum.Meth.* **A618** (2010) 139

[30] Abbasi, R. et al.,*Nucl.Instrum.Meth.* **A601** 294

[31] IceCube Coll., *Generation 2 IceCube Digital Optical Module and DAQ*, PoS(ICRC2015) 1148, *These proceedings*

[32] IceCube Coll., *A dual-PMT optical module (D-Egg) for IceCube-Gen2*, PoS(ICRC2015) 1137, *These proceedings*

[33] IceCube Coll., *Multi-PMT optical modules for IceCube-Gen2*, PoS(ICRC2015) 1147, *These proceedings*

[34] D.Hebecker et al., *Progress on the Development of a Wavelength-shifting Optical Module*, PoS(ICRC2015) 1134, *These proceedings*

PROCEEDINGS OF SCIENCE

Multi-PMT optical modules for IceCube-Gen2

The IceCube-Gen2 Collaboration[1],

[1] *http://icecube.wisc.edu/collaboration/authors/icrc15_gen2*

E-mail: lew.classen@physik.uni-erlangen.de

Following the first observation of astrophysical high-energy neutrinos by IceCube, planning for a next-generation neutrino detector at the South Pole is under way, which will significantly expand IceCube's sensitivity both towards high and low neutrino energies. In addition to upgrading the proven IceCube design, new optical sensor concepts are explored which have the potential to substantially enhance the performance of IceCube-Gen2. One concept is the multi-PMT optical module which, in contrast to the "conventional" layout with a single 10-inch photomultiplier (PMT), features 24 3-inch PMTs inside a pressure vessel. This design results in several advantages such as increased effective area, improved angular acceptance and better directional sensitivity. The layout is based on the proven design of the KM3NeT optical module which is now being adapted and enhanced for the use in the deep ice. We present the current state of the hardware developments as well as first simulations investigating the impact of multi-PMT modules on detector performance.

Corresponding authors: Lew Classen*[1], Alexander Kappes[1],

[1] *ECAP, University of Erlangen-Nuremberg, Erlangen, Germany*

The 34th International Cosmic Ray Conference,
30 July- 6 August, 2015
The Hague, The Netherlands

*Speaker.

1. Multi-PMT concept

Currently operating large volume neutrino telescopes, namely IceCube [1], ANTARES [2] and BAIKAL [3], are composed of optical modules with a single large photomultiplier tube (PMT). The IceCube DOM, for instance, consists of a 13-inch glass sphere housing a 10-inch Hamamatsu R7081-2 PMT [4] a μ-metal cage and digitization electronics [5]. In contrast, a multi-PMT optical module, first developed for the KM3NeT neutrino telescope, houses an array of several small PMTs and their read-out electronics [6]. One of the main drivers for the development was the reduction of the number of costly and risky underwater connectors present in the ANTARES design. However, the approach has a number of other attractive advantages compared to the conventional design at a similar overall price per photocathode area:

- **Increase of photocathode area**: The photocathode area of ten 3-inch PMTs roughly corresponds to that of one 10-inch tube. Thus a multi-PMT DOM containing several tens of 3-inch PMTs is equivalent to several conventional IceCube optical modules.
- **Superior photoelectron counting**: The number of photoelectrons can be more directly derived from the number of hit PMTs compared to the extraction from a multi-photoelectron signal waveform.
- **Improved angular acceptance**: With the distribution of the photocathode area across the total solid angle, a near homogeneous 4π coverage can be achieved (see Fig. 3).
- **Directional sensitivity**: The orientation of the hit PMT carries information on the direction of the incoming photon that can be used in the reconstruction.

The hardware functionality and physics capability of the multi-PMT concept have been demonstrated in-situ with the deployment and operation of KM3NeT prototypes in the Mediterranean [7]. As its properties give the multi-PMT module the potential to significantly enhance the performance of future neutrino detectors, it is, together with the WOM [8] and the D-Egg [9], one of the new optical sensor concepts under investigation for the IceCube-Gen2 project [10].

2. Prototype development for IceCube-Gen2: The mDOM

2.1 Hardware design

The adaptation of the multi-PMT layout for a deep-ice environment benefits from the research and development made for KM3NeT, in particular from the availability of suitable three-inch PMTs and corresponding low-power high voltage circuitry. However, the use in deep ice requires a major redesign of the pressure vessel. The constraints of using the currently available drilling technology and avoiding significant increase of costs limit the module diameter to approximately 14 inches ($\sim$ 356 mm) while the sensitive area of the module would benefit from an increase in diameter. As a trade-off, the form will slightly diverge from that of a perfect sphere in order to maximize the number of PMTs per module resulting in two 14-inch hemispheres with cylindrical extensions of a few centimeters (see Fig. 1). Given the dimensions of currently available PMT prototypes,

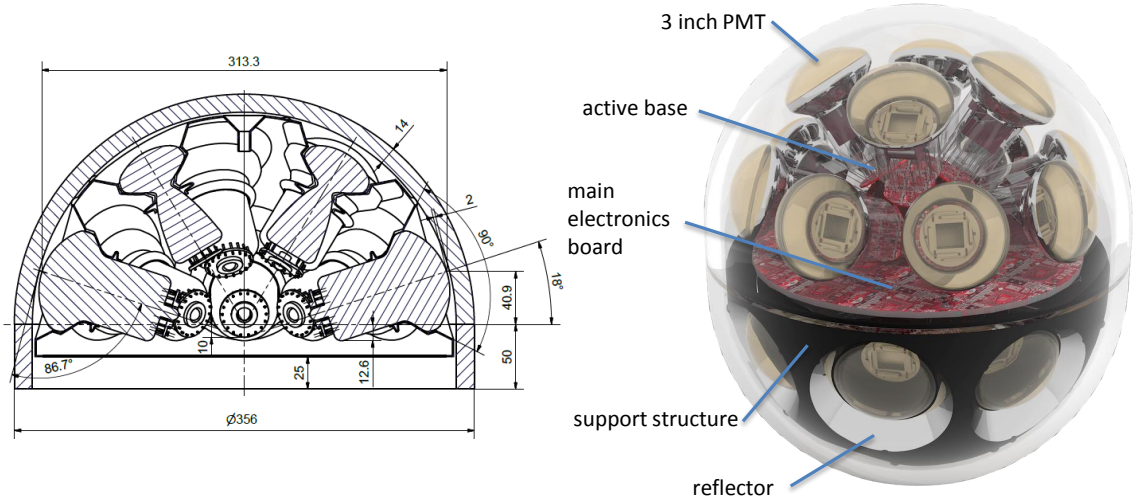

Figure 1: Left: Technical drawing of a mDOM hemisphere. Dimensions are given in mm. **Right:** Artist's impression of the planned mDOM highlighting the main components. The black holding structure in the bottom hemisphere is omitted in the upper hemisphere to better illustrate the internal components and arrangement.

each hemisphere will be able to house twelve 3-inch PMTs. A crucial requirement on the vessel stability is imposed by the in-ice ambient pressure. IceCube measurements indicate that during refreezing of the water column the vessel has to sustain a pressure of up to 700 bar ($\sim 10,000$ psi). As corresponding glass housings are currently not commercially available, negotiations with a glass manufacturer (Nautilus GmbH) are under way to develop a suitable design for the project. For positioning of the PMTs and auxiliary equipment inside the vessel a supporting structure has been designed. First prototypes were produced from polyamide (type PA 2200 [11]) using laser sintering by a commercial company. For mass production, alternative, more cost-effective production methods are also taken into consideration.

2.2 Photomultiplier tubes

At present two companies (Hamamatsu[1], ET Enterprises[2]) provide 3-inch PMTs[3] for KM3NeT which are also considered for the use in the IceCube-Gen2 module. These were optimized to fit predefined requirements (see [12]). An excerpt of the achieved performance is listed in Tab. 1. For details on test procedures see [13] and [14]. For prototyping, R12199-02 PMTs by Hamamatsu will be used. However, with its bigger photocathode diameter and shorter tube length, the type D792KFL PMT supplied by ET Enterprises is also well suited for the use in the project. Further

[1] http://www.hamamatsu.com/us/en/index.html

[2] www.et-enterprises.com

[3] The diameters of the originally available 3-inch PMTs ($\sim$ 76 mm) have been increased by the manufacturers: to 80 mm for the R12199-02 by Hamamatsu, and to 86 mm in the case of D792KFL by ET Enterprises.

candidate PMTs might become available from HZC[4] (producing 3-inch PMTs since mid-2013) and MELZ[5] (prototype presented in April 2015). However, the results of tests performed on initial HZC specimen do not meet with the KM3NeT requirements yet, especially concerning dark rate [15]. Technical modifications of PMT characteristics can be considered once specific requirements are defined for IceCube-Gen2, e.g. lower values are desirable for the dark rate in order to take full advantage of the low background environment in the deep glacial ice.

The utilization of hemispherical PMTs attached to the inner surface of a spherical pressure vessel with lower curvature results in significantly increased mean thickness of gel traversed by the photons arriving from high inclinations which leads to losses due to absorption and reflection. Furthermore, as thick gel layers are costly, in practice the holding structure would be constructed such that it shadows these photons thereby reducing the effective area. Therefore, reflectors in the form of hollow cone rings are used (see Fig. 1, right). These reflector rings, cut and formed from coated aluminum sheets (ALMECO V95100, [16]), redistribute the angular acceptance from high to low inclinations (see Fig. 2) thus increasing sensitivity of the PMTs in the central $\pm 50^\circ$ direction by about 30%.

The polarity of the high voltage applied to the PMT is a major decision. A PMT can be operated either with its photocathode at negative high voltage and the anode at ground potential (negative polarity) or, in the case of positive polarity, the cathode is grounded and the anode connected to positive high voltage. Both approaches come with their respective advantages and limitations: While the output of a PMT at negative polarity can be directly fed into read-out electronics, positive polarity demands galvanic separation of the anode (e.g. using a capacitor) which affects the quality of the output. On the other hand, a photocathode at high negative potential promotes increased and unstable dark rates. This effect is more pronounced if objects at ground potential are placed near the PMT, in particular near the photocathode area, like the metal reflectors in case of the mDOM.

Long-term measurements have shown that optical gel covering the photocathode area significantly improves the stability of the dark rate. Whether the gel is sufficiently effective for use of negative high voltage polarity in the mDOM without losing the advantage of low environmental background in IceCube is currently under investigation. Also under investigation is noise reduction via "HA coating" [17] as proposed by the PMT manufacturer. In this configuration, the outer surface of the PMT outside the photocathode area is coated with conductive paint connected to the photocathode potential and sealed with an insulation layer. Two specimen of such coated PMTs were acquired for performance tests. First measurement show a positive effect on the dark count rate and its stability.

quantum efficiency (at 404 nm)	$\sim 27\,\%$	**supply voltage**	$< 1400\,\mathrm{V}$
quantum efficiency (at 470 nm)	$\sim 22\,\%$	**dark rate (at 20°C)**	$0.2 - 1.5\,\mathrm{kHz}$
transit time spread	$FWHM < 5\,\mathrm{ns}$	**peak to valley ratio**	> 3

Table 1: Current performance examples of PMTs used for KM3NeT multi-PMT optical modules (selected from [6]). Some requirements have been updated in the course of the development. For original values see [12].

[4] http://www.hzcphotonics.com/en_index.html
[5] http://www.melz-feu.ru/

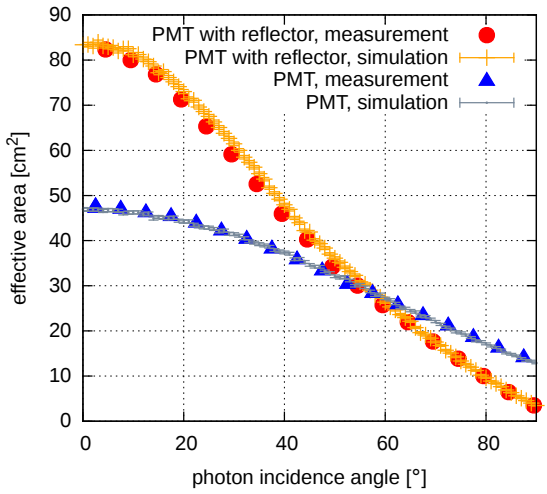

Figure 2: Angular acceptance of a single Hamamatsu R12199-02 PMT in different configurations. The effective area values were calculated normalizing the measured relative signal amplitudes to the geometrical photo-cathode area for perpendicular incidence. The measurement was performed for a bare PMT *(triangle)* and a reflector equipped PMT mounted on a holding structure *(circle)*. Effective areas from a Geant4 simulation of the two setups (*grey*: bare PMT, *orange*: PMT with reflector) are shown for comparison. Error bars indicate the statistical uncertainties. Simulation is described in section 3.1.

2.3 Electronics development

The baseline data acquisition aims at providing information equivalent to the current single PMT technology, enhanced by the pattern of the hit distribution across the PMTs. This leads to a dual digitization approach: On the one hand, the waveform from the sum of the individual PMT signals is digitized. It is unfolded into single photoelectron pulses using a corresponding template waveform. This information can be used to recover the original signal shape. On the other hand, the individual waveforms produced by the PMTs are converted to a time-over-threshold (ToT) step function at the base (via base-borne ASICs or discrete components). The ToT signals are sent to the main logic board, featuring an FPGA and a synchronized clock with a TDC unit, for digitization providing additional time-stamped ToT information for each PMT. Alternative approaches under investigation are extraction of multiple ToTs, local digitization at the base using very fast comparators or the measurement of the pulse maximum during the above-threshold state to discriminate between single high-amplitude signals and multiple low-amplitude pulses arriving in quick succession. Final decisions on the read-out technique will also consider the available data bandwidth of about 1 MBit/s and a total power budget of less than 4 W per optical module. A corresponding low-power active PMT base, including front-end readout electronics, is currently under development.

3. Simulation efforts

3.1 Angular acceptance

The angular acceptance properties of the module were investigated using a Geant4-based [18] Monte-Carlo simulation of the "effective sensitive area" as a function of photon incident angle and wavelength. The mDOM as modeled in Geant4 includes the glass vessel, a gel infill and reflective cones with their respective optical properties (refractive index, absorption length and scattering length) as well as a totally absorbing PMT holding structure. The PMT model consists of a solid glass bulb containing the photocathode. The rear of the photocathode half-ellipsoid is shielded against photons with a totally absorbing disc. The mDOM is placed in ice with the appropriate refractive index and infinite absorption and scattering length. In the current setup, photon propaga-

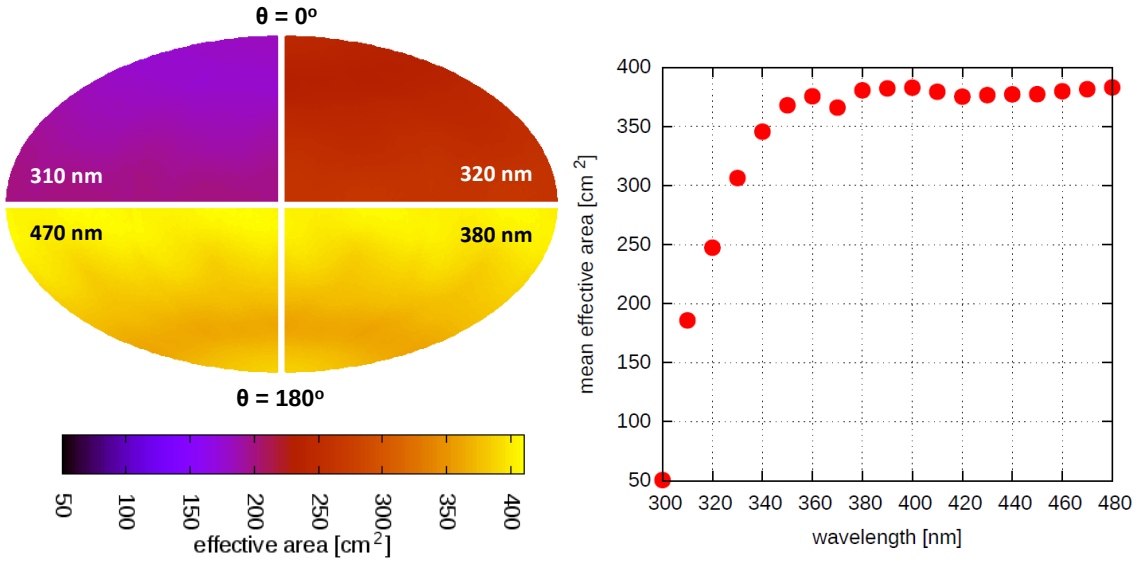

Figure 3: Left: Hammer projection of the mDOM photon acceptance represented as effective area as a function of direction of the incident photons in zenith angle (θ) and azimuth (ϕ). Values are shown for different original photon wavelengths obtained from a Monte-Carlo simulation based on Geant4. The module was oriented as shown in Fig. 1 with vertically down-going photons corresponding to $\theta = 0°$. Due to the symmetry in the orientation of the PMTs inside the module each of the shown quadrants is representative of the total solid angle for the respective wavelength. For model details see section 3.1 **Right:** Wavelength dependence of the mean mDOM effective area. Values were obtained averaging solid angle weighted Monte-Carlo results over 4π. Statistical errors are calculated to be smaller than data points.

tion stops at the surface of the photocathode where the photon is registered neglecting the effects of the inner structure of the PMT (such as back-scattering of photons). The impact of the PMT's quantum efficiency is not included. A plane uniformly radiating parallel optical photons in normal direction (λ between 300 and 470 nm, $N = 10^6$ per direction) is rotated around the module uniformly sampling the azimuth and zenith angles. The total fraction of photons reaching one of the photocathodes multiplied by the area of the radiator corresponds to the effective sensitive area of the module for a given direction equal to the normal of the plane. At the moment, the simulation was performed for R12199-02 type PMTs only. Results are shown in Fig. 3. The obtained distribution of the effective area features homogeneous coverage of the total solid angle. The dependence on the photon wavelength is dominated by the transmittance of the glass vessel. For means of comparison, a standard IceCube DOM was also simulated using the same approach showing an increase of the average effective area of the module by a factor of 2. To assess the validity of the model, it was also used to reproduce a lab measurement of the angular acceptance of a single PMT with and without a reflective cone (see Fig. 2). The glass vessel was removed and ice and gel were replaced by air to reflect lab conditions. Simulation and measurement do agree well, with maximum discrepancies below 5 %. Reasons for the remaining differences are under investigation.

3.2 mDOM detectors

In order to assess the impact of mDOMs on the performance of future high and low-energy detectors, a corresponding module was implemented in IceTray [19], the standard IceCube simulation framework. In this simulation, charged particles from the neutrino interaction are propagated with Geant4 which handles the energy loss and the production of Cherenkov radiation. Subsequently, the resulting Cherenkov photons are individually propagated through the ice taking into account the inhomogeneity of the ice properties (clsim[6] was used for photon propagation, ice properties modeling described in [20]). Photons arriving at the surface of an optical module are stored. Propagation inside the module is performed via a simple ray tracing code neglecting refraction. A hit is registered when a photon intersects a PMT represented by a flat thin disc featuring the angular acceptance of a PMT with reflector as measured in the lab. As a further refinement, a signal waveform generator based on measured PMT characteristics will be added.

At present, the simulation is a 40 string detector geometry featuring 22 m string spacing and a vertical distance of three meters between the mDOMs. The same setup was also simulated using single PMT optical modules. For means of assessing the gain achieved for low-energy (few GeV) neutrino events in such detectors the total number of PMT hits for both detectors was calculated yielding a factor of ~ 2 more hits for the mDOM detector which is in good agreement with the increase of effective area per optical module discussed in section 3.1. Simulations of high energy neutrino detectors and a potential future megaton-scale detector with sensitivity to events at and below the MeV range for proton decays and supernova neutrinos are in preparation.

4. Current project status and next steps

The design of the pressure vessels is being finalized and first specimen are expected to be available in late 2015. 3-inch PMTs from Hamamatsu are available and will be used in mDOM prototyping. A low-temperature (down to $-70\,^{\circ}\mathrm{C}$) test bench has been set up to measure PMT and optical module properties crucial for the use in the deep ice such as the dark rate and background form radioactive decays in the glass in conditions closer to final application. Work on the design of the PMT base incorporating a pre-amplifier and time-over-threshold signal generation is in progress and options for the summation electronics and integration into the IceCube-Gen2 DAQ are being investigated. Simulations currently undertaken address the properties of the module itself as well as the impact of the utilization of mDOMs on the performance of IceCube-Gen2 and a potential future megaton sub-GeV neutrino detector which are expected to benefit from the increased effective area and superior information on the recorded photons.

Acknowledgments

The low-power active PMT bases for the use in the mDOM project are developed by Andreas Bänisch, Jürgen Röber, Alexander Kölpin, and Stefan Lindner from the Institute for Electronics Engineering of the University of Erlangen-Nuremberg.

[6] C. Kopper, [https://github.com/claudiok/clsim]

References

[1] F. Halzen and S. R. Klein, *Rev. Sci. Instrum.* **81** (2010) 081101 [http://dx.doi.org/10.1063/1.3480478]

[2] **ANTARES** Collaboration, M. Ageron et al., *Nucl. Instrum. & Meth.* **A656** (2011) 11 [http://dx.doi.org/10.1016/j.nima.2011.06.103]

[3] **BAIKAL** Collaboration, I. A. Belolaptikov et al., *Astropart. Phys.* **7** (1997) 263

[4] **IceCube** Collaboration, R. Abbasi et al., *Nucl. Instrum. & Meth.* **A618** (2010) 139 [arXiv:1002.2442]

[5] **IceCube** Collaboration, R. Abbasi et al., *Nucl. Instrum. & Meth.* **A601** (2009) 294 [arXiv:0810.4930v2]

[6] **KM3NeT** Collaboration, R. Bruijn and D. van Eijk, PoS(ICRC2015)1157 these proceedings

[7] **KM3NeT** Collaboration, S. Adrian-Martinez et al., *Eur. Phys. J.* **9 C74** (2014) 3056 [arXiv:1405.0839]

[8] D. Hebecker et al., PoS(ICRC2015)1134 these proceedings

[9] **IceCube-Gen2** Collaboration, PoS(ICRC2015)1137 these proceedings

[10] **IceCube-Gen2** Collaboration, M. G. Aartsen et al., (2014) [arXiv:1412.5106]

[11] EOS GmbH, *Material data sheet - PA 2200*, [https://www.shapeways.com/rrstatic/material_docs/mds-strongflex.pdf]

[12] **KM3NeT** Collaboration, P. Bagley et al., *KM3NeT Technical Design Report* (2011) [http://www.km3net.org/TDR/TDRKM3NeT.pdf]

[13] S. Aiello et al., *Characterization of the 80-mm diameter Hamamatsu PMTs for the KM3NeT project* in *Proc. of VLVnT 2013*, *AIP Conf. Proc.* **1630** (2014) 118 [http://dx.doi.org/10.1063/1.4902786]

[14] G. Bourlis et al., *Characterization of the KM3NeT photomultipliers in the Hellenic Open University* in *Proc. of VLVnT 2013*, *AIP Conf. Proc.* **1630** (2014) 106 [http://dx.doi.org/10.1063/1.4902783]

[15] R. Bormuth et al., *Characterization of the ETEL and HZC 3-inch PMTs for the KM3NeT project* in *Proc. of VLVnT 2013*, *AIP Conf. Proc.* **1630** (2014) 114 [http://dx.doi.org/10.1063/1.4902785]

[16] Almeco Spa, *vega Lighting Applications*, [http://www.almecogroup.com/uploads/841-ALMECO_vega_ENG_L101_11_2013_mail.pdf]

[17] Hamamatsu Photonics, *Photomultiplier Tubes: Basics and Applications* (2007) [https://www.hamamatsu.com/resources/pdf/etd/PMT_handbook_v3aE.pdf]

[18] S. Agostinelli et al., *Nucl. Instrum. & Meth.* **A506** (2003) 250

[19] T. R. De Young, *IceTray: a software framework for IceCube*, in *Proc. of CHEP 2004* (2005) p. 463

[20] **IceCube** Collaboration, M. G. Aartsen et al., *Nucl. Instrum. & Meth.* **A711** (2013) 73 [arXiv:1301.5361]

[21] **IceCube-PINGU** Collaboration, M. G. Aartsen et al., (2014) [arXiv:1401.2046]

PROCEEDINGS OF SCIENCE

The IceCube Generation-2 Digital Optical Module and Data Acquisition System

The IceCube-Gen2 Collaboration†
†*http://icecube.wisc.edu/collaboration/authors/icrc15_gen2*
E-mail: michael.duvernois@icecube.wisc.edu

With recent exciting observations of astrophysical TeV- to PeV-energy neutrinos and new competitive measurements of GeV-energy atmospheric neutrino oscillations in the IceCube neutrino observatory at the South Pole, the design of a second generation Antarctic neutrino observatory, IceCube–Gen2, is underway. The design calls for two new instrumented volumes, one a denser in-fill array to extend the sensitivity of IceCube to energies low enough to gain sensitivity to the neutrino mass hierarchy, and one approximately ten times larger than IceCube, about 10 cubic kilometers in extent, to improve the sensitivity of IceCube to high energy astrophysical neutrinos and their sources. The detectors will share many common hardware elements and will leverage the successful hardware and software of the first generation experiment. They will feature updated data acquisition electronics using commercially available components and taking advantage of advances in embedded computing power. We describe the status of the modernized in-ice Digital Optical Module (DOM) and the supporting surface electronics and data acquisition components.

Corresponding authors: M. A. DuVernois[1]*, T. Anderson[2], K. Hanson[1], J. L. Kelley[1], P. Sandstrom[1], and K. Sulanke[3]

[1] *Dept. of Physics and Wisconsin IceCube Particle Astrophysics Center, University of Wisconsin, Madison, WI 53706, USA*

[2] *Dept. of Physics, Pennsylvania State University, University Park, PA 16802, USA*

[3] *DESY Zeuthen, Platanenallee 6, 15738, Zeuthen, Germany*

The 34th International Cosmic Ray Conference,
30 July- 6 August, 2015
The Hague, The Netherlands

*Speaker.

1. Introduction

With the recent observations of TeV astrophysical neutrinos and very competitive measurements of atmospheric neutrino oscillations, there is interest in adding onto the IceCube detector to increase its acceptance by a large factor. IceCube's Digital Optical Modules (DOMs) were quite successful and form the basis of the design for a new generation (Gen2) DOM, taking particular advantage in improvements in fast, low power digitizers and programmable logic while retaining the proven overall design of the first generation DOM and many of the remaining available parts. The Data Acquisition (DAQ) system consists of the hardware modules that read the DOM data after cable transmission, and aggregate that data onto Ethernet for online (software) triggers and filters that can request detailed readouts of the DOMs through the same hardware. The Gen2 surface hardware readout system will be backwards compatible with the original IceCube DOM readouts, but will be able to be deployed either indoors or outdoors at the top of the detector strings. Additionally, a major design goal will be a decreased physical footprint in the surface building.

PINGU and the High Energy Array extensions to IceCube have decidedly different physics goals, but will have a nearly uniform hardware implementation at the DOM level[2, 3]. Detector module spacing and triggering allow for the vastly different physics objectives. With the common design elements, an overall philosophy of Gen2 IceCube DOM and DAQ development is to keep as much commonality as possible, keep as much of the IceCube hardware heritage in place, but gain from electronics developments in the decade since the IceCube hardware design was frozen. Research and development for the Gen2 detector elements has been progressing over the last year and a half or so, and now has hardware samples of much of the detector signal chain, though in lab-only physical formats, and with some of the elements yet to be implemented. Near future development will continue with the goal of increased integration and the ability to have reasonable detector hardware in hand ahead of, and in support of, a funding proposal.

2. Digital Optical Modules

The IceCube DOM evolved from the earlier AMANDA analog optical module with primary goals of high-reliability, accurate waveform digitization, and flexibility in surface readout [1]. The primary design differences between first and second generation DOMs are highlighted in Fig. 1. The analog delay required for the first generation digitizer is eliminated, and there is an overall simplification and consolidation of the electronics, while the mechanicals remain very faithful to the original proven design.

High level requirements for the DOMs include a sampling rate of >160MSaps in order to adequately digitize the PMT pulse, data transmission rate of greater than 1 Mbps, absolute time discrimination on the order of 1–2ns, power consumption of <4W (IceCube actual) and ideally <2W per DOM, and dynamic range to cover from at least 1/25 of a single photoelectron (SPE) up to about 425 SPE for PINGU (perhaps higher for the high energy extension). The dynamic range available is being investigated including the possibility of dynamic pulse compression.

The overall system architecture of the Gen2 DOM is shown in Fig. 2. In all cases, we show the baseline hardware design in this paper; however, there are alternate technologies, chip selections, and firmware paths under investigation with final trade studies to take place through system

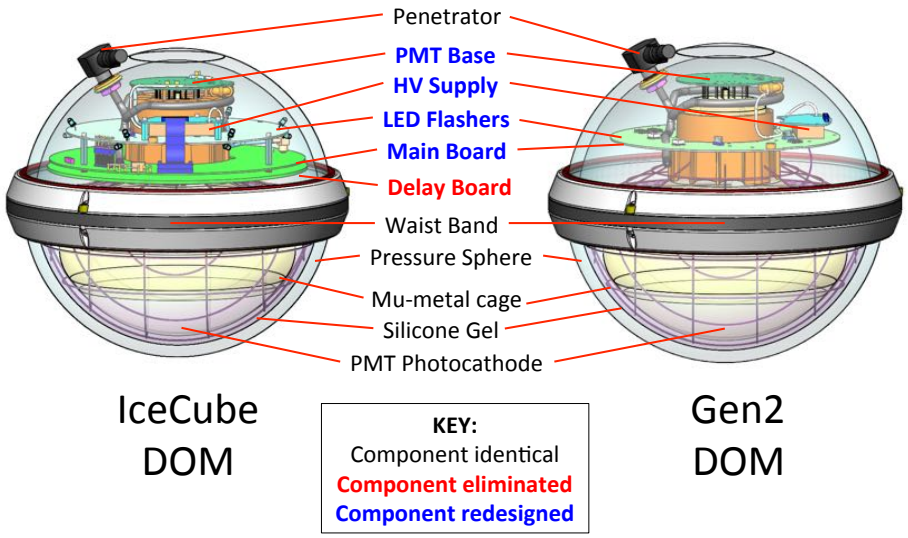

Figure 1: A comparison between the current IceCube DOM (left) and the Gen2 DOM (right).

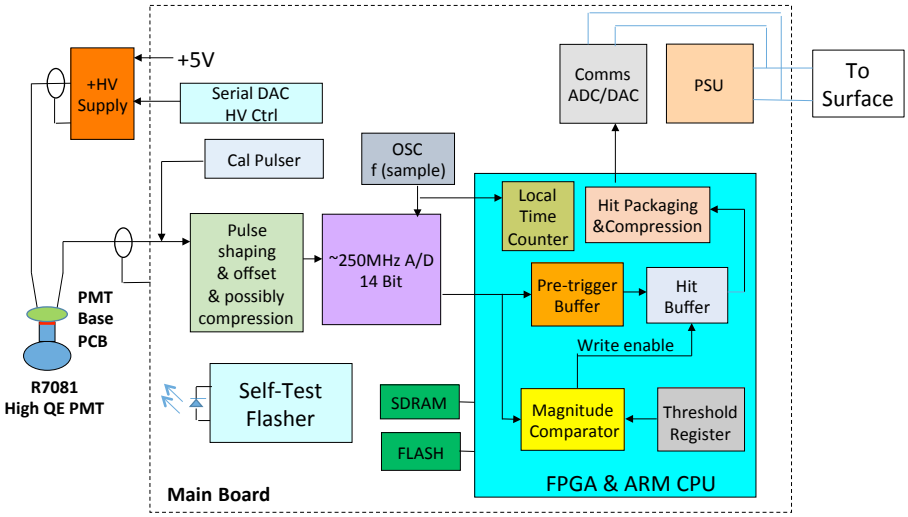

Figure 2: Block diagram of the of the Gen2 DOM mainboard.

and subsystem reviews. The 10" High Quantum Efficiency (HQE) photomultiplier tube (PMT) is readout through an analog front end that shapes the signal, performs anti-alias filtering, centers the unipolar PMT pulse into the bipolar ADC window, and drives the input of the digitizer. The PMT remains the same as used in IceCube ([6]), the Hamamatsu R7081-02. Alternate arrangements of smaller PMTs ([7]), dual PMTs with high transparency windows ([8]), or custom-constructed wavelength-shifting optical modules ([9]) are also under consideration, though they too would couple into a DAQ architecture similar to what is presented here.

The digitizer is an ADS4149 250MSaPS pipelined ADC drawing about 250mW of power while continuously sampling the analog waveform with 14 bit (11.2 ENOB) resolution. This dynamic range is somewhat smaller than the 1/25 SPE to 425 SPE high-level requirement listed above.

This tension is under investigation with possible solutions including dual channels (high and low gain or anode and deep dynode tap), analog signal compression, or a loosening of the requirements. This is a deadtime-free system with the local triggering based on the digital output of the ADC. The FPGA takes the continuous waveform data and allows flexible triggering based on a simple voltage threshold or a number of samples over threshold. For IceCube-Gen2 array use we plan compression and/or feature extraction of single, and perhaps multiple, photoelectron hits within the onboard programmable logic.

A second version of the Digitizer Daughter Card (DDC2, see Fig. 3) for lab testing has been produced and is being operated in concert with a commercial evaluation kit for the FPGA chosen for this design. The readout noise for the combined analog front end and digitizer is consistent with the specification sheet for the ADS4149 (see Fig. 4) with intrinsic RMS noise of just over one bit.

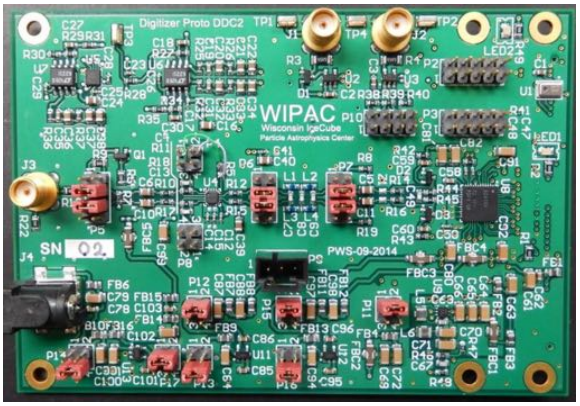

Figure 3: The prototype Digitizer Daughter Card (DDC2).

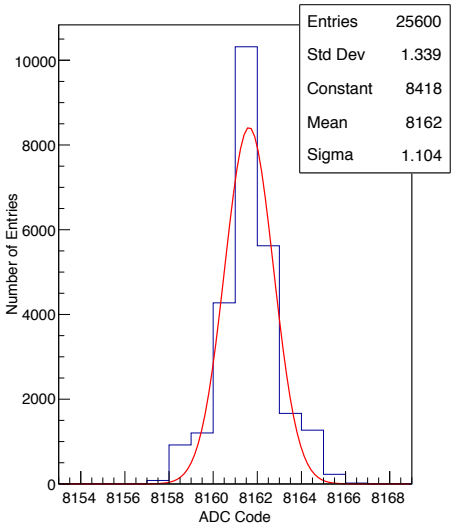

Figure 4: Baseline ADC readout in the DDC2 (terminated).

As an alternative to the commercial PMT high voltage supplies tested for and used in the IceCube DOM, we have designed a prototype custom high voltage supply based on the UMHV ultra-miniature HV supply from HVM Technology (see Fig. 5). Power consumption ranges from 90 to 180mW depending on output voltage ($75M\Omega$ load). Stability and ripple characteristics are still under investigation.

Communications and absolute system timing are conducted over a minimum of 1.5km (top of the array to the surface) up to a maximum of 3.5km (in IceCube, from 2.5km depth and across the array) of copper quads. The timing system (RAPCAL) is carried over from IceCube and consists of reciprocal transmission and reception of test pulses coordinated with GPS timing at the surface [1]. Communications consist of dedicated logic-controlled ADCs and DACs, and are discussed below.

Figure 6 shows a block diagram representation of the firmware which was developed to readout the DDC. The ADC-FPGA Interface module divides the incoming Double Data Rate (DDR) 250 MSaPS ADC data stream into four parallel Single Data Rate (SDR) streams, each running at 62.5 MSaPS. Dividing the data stream in such a way allows the design to easily meet all synchronous timing requirements, while making only modest tradeoffs in resource utilization and de-

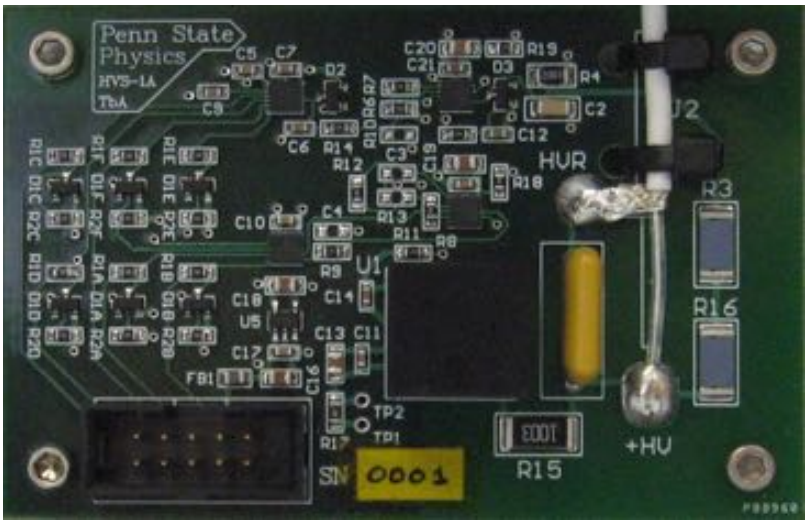

Figure 5: Prototype high voltage supply (HVS) daughterboard.

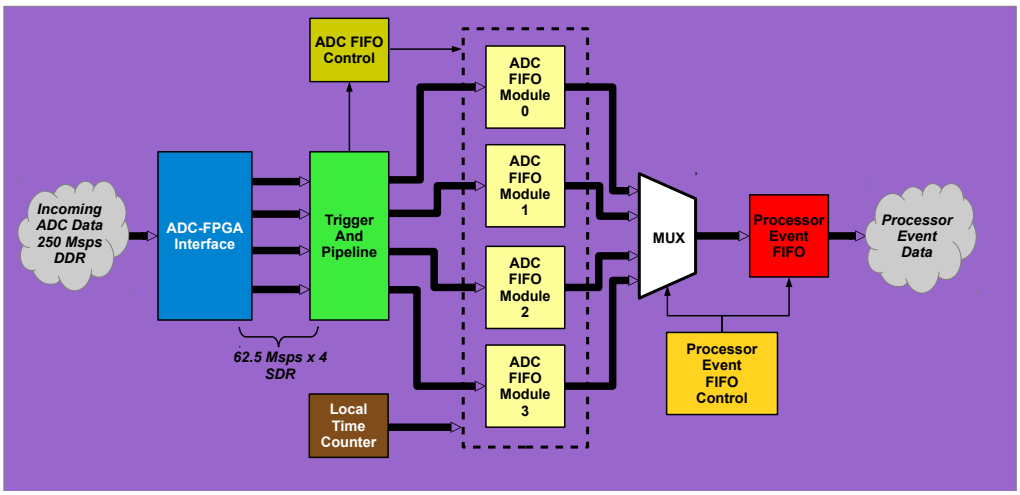

Figure 6: Block diagram for the DOM firmware.

sign complexity. The Trigger and Pipeline module examines the data stream for the occurrence of any of a number of user-programmable trigger conditions, signaling the ADC FIFO Control module to begin filling the ADC FIFOs with event data when the active trigger condition is satisfied. A 48-bit timestamp generated by the Local Time Counter module is also stored with each event. Data on the output side of the ADC FIFOs is sequentially re-ordered by the Processor Event FIFO Control module and presented to the FPGA's processor for formatting and transmission to the user.

The DOM design also allows for ancillary sensor systems (provided they are low average data rate) such as cameras for inspecting the refrozen hole ice near the detector, acoustic sensors for 3D-imaging of ice fracturing, or novel radio detector systems (*e.g.*, [4]). This general interface includes 5VDC, 100mW power and an SPI or I2C local communications protocol along with handling of data through the remainder of the DAQ.

The DOMs are to be permanently embedded into the South Pole glacial ice, so their long-

term reliability must be high. The IceCube DOMs had a better than 99% survival rate in the ice, with the small number of failures typically occurring during or shortly after deployment. We will follow the program of extensive design verification and testing at the component, subsystem, and system levels. Most passive components are of automotive or military reliability specification. For example, the high voltage modules have been deployed in about 100,000 night vision goggle units used worldwide in a wide range of environments. Whenever possible, proven components and processes will be used.

3. Data Acquisition (DAQ)

The readout of the DOMs consists of two layers: a hardware DOM communications board with power and timing, and the computers that construct the triggers, filter data, and archive events. We focus on the DOM communications hardware, which in IceCube consists of a PCI interface and communications card (DOR) hosted with other DOR cards in a DOMHub that also includes the downhole power supply, timing connection, and a networked single board computer. The Gen2 design is backwards compatible with IceCube to allow for the replacement of the DOR/DOMHubs in time for both power savings and a smaller footprint in the IceCube Laboratory (ICL).

The communications for the Gen2 design are handled with a Communications Daughter Card (CDC); see Fig. 7. The essential features of the communications channel are the arbitrary firmware definition of the in-channel encoding supported by protection circuitry, DC bias for DOM power, and general purpose ADCs and DACs bridging cable distance. Full duplex power consumption for this circuit is less than 200mW which is less than a sixth the power of a typical (AD9869) modem chipset. Multiple CDC boards would live on a carrier card (backplane) with shared power supplies (CDC and downhole DOM), GPS timing connection, and mechanical mounting. See Fig. 8 for a diagram with existing IceCube patch cable connectors matched up with the new CDCs.

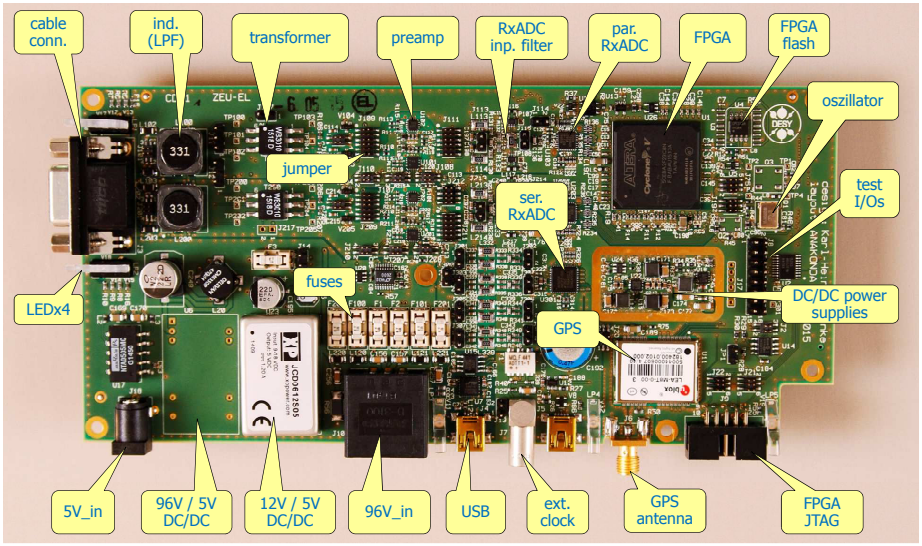

Figure 7: The Communications Daughter Card (CDC) prototype board.

In addition to compressing the physical layout of the DOM readout electronics which is important if $O(100)$ strings are added to the IceCube detector to avoid dramatic increases in counting

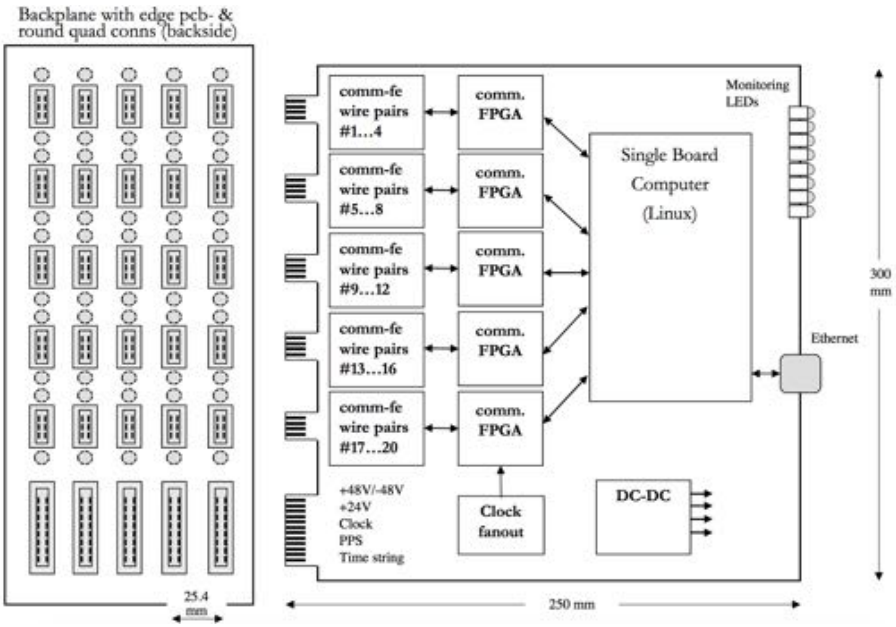

Figure 8: Readout architecture supporting a string of DOMs on a single card.

house space, strings at a significant distance from the counting house can be better managed with a String-Hub which resides outdoors (in an insulated vault) near the top of the string. For such remote installations, data transfer will be over fiber-based Ethernet and timing maintained through the use of the White Rabbit ([10]) protocol to the top of the string and RAPCAL down the string.

4. System Construction, Integration, and Deployment

The IceCube DOMs were built and tested at three distinct production facilities (DESY, Stockholm, and UW-Madison) ahead of shipment to the South Pole. All DOMs received extensive end-to-end testing including thermal stress and thermal soak in the Northern Hemisphere. DOMs will be transported in custom boxes that enable easy cable connections without removing the housing from the box. Final testing is performed before unpacking and preparations for deployment. Nonconforming materials are shipped back to the north for possible repairs.

Optical modules are deployed off of a custom Ericsson built cable consisting of cable quads, strength member, and outer jacketing. For the higher density PINGU strings, some differences in attachment method are foreseen. Fig. 9 shows a comparison of the mechanical string/cable to DOM mounting hardware. The mounting approach, with the string temporarily relaxed during DOM connection, also allows for the attachment of "special devices," non-DOM detector elements which might include, for example, direct dark matter detectors or ice optical propagation study devices (e.g., [5]).

5. Conclusions

Gen2 IceCube DOMs and DAQ components are well past the conceptual design stage and hardware is being prototyped and tested. These efforts aim to shorten the development time line

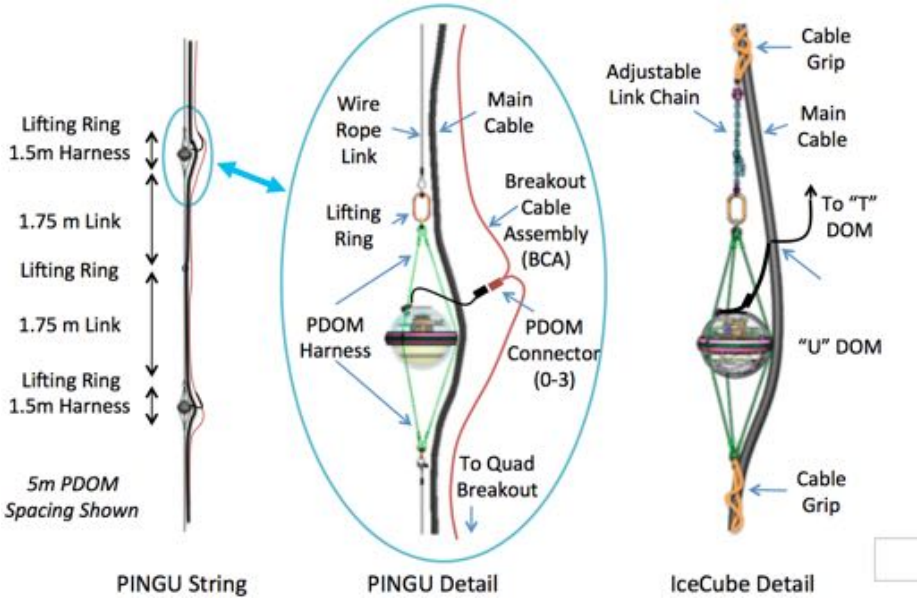

Figure 9: Current and planned DOM mounting strategies.

for both PINGU and the IceCube High Energy Array detector systems, leveraging prior successful developments while also taking advantage of more recent electronics developments.

References

[1] R. Abbasi *et al.* (IceCube Collaboration), Nucl. Instrum. Meth. A **601**, 294 (2009).

[2] M.G. Aartsen et al. (IceCube-PINGU Collaboration), Letter of Intent: The Precision IceCube Next Generation Upgrade (PINGU), arXiv:1401.2016.

[3] E. Blaufuss et al. (IceCube Gen2 Collaboration), The IceCube-Gen2 High Energy Array, Proc. of 34th ICRC, The Hague, 741 (2015).

[4] D. Bose et al. (IceCube Gen2 Collaboration), PINGU Camera System to Study Properties of the Antarctic Ice, Proc. of 34th ICRC, The Hague, 687 (2015).

[5] K. Krings et al. (IceCube Gen2 Collaboration), A Precision Optical Calibration Module for IceCube-Gen2, Proc. of 34th ICRC, The Hague, 184 (2015).

[6] R. Abbasi et al. (IceCube Collaboration), Nucl. Instrum. Meth. A **618**, 139-152 (2010).

[7] L. Classen et al. (IceCube Gen2 Collaboration), Multi-PMT optical modules for IceCube-Gen2, Proc. of 34th ICRC, The Hague, 743 (2015).

[8] L. Lu, H. Ijiri et al. (IceCube Collaboration), A dual-PMT optical module (D-Egg) forIceCube-Gen2, Proc. of 34th ICRC, The Hague, 474 (2015).

[9] M. Archinger et al. (IceCube Collaboration), Progress on the Development of a Wavelength-shifting Optical Module, Proc. of 34th ICRC, The Hague, 474 (2015).

[10] Open Hardware Repository/CERN. *http://www.ohwr.org/projects/white-rabbit*

PROCEEDINGS OF SCIENCE

Motivations and Techniques for a Surface Detector to Veto Air Showers for Neutrino Astronomy with IceCube in the Southern Sky

The IceCube-Gen2 Collaboration[†]**,**

[†] *http://icecube.wisc.edu/collaboration/authors/icrc15_gen2*

E-mail: jauffenb@icecube.wisc.edu

IceCube is currently the world's largest high-energy neutrino observatory, built at the geographic South Pole. For neutrino astronomy, a large sample of well-reconstructed astrophysical neutrinos of high purity is essential. The main backgrounds are muons and neutrinos, produced in cosmic-ray air showers in the Earth's atmosphere. The coincident detection of these air showers by the surface detector component IceTop is already used in IceCube neutrino analyses to veto atmospheric neutrinos and muons in the down-going region which at the South Pole corresponds to the southern sky. The successes and limitations of the IceTop array as an air shower veto motivate properties of future surface veto detectors to improve the performance of the next-generation neutrino telescope in Antarctica, *IceCube-Gen2*. The significance of this improvement depends on the features of the astrophysical neutrino spectrum. Here, we summarize different physics cases that motivate a surface veto and the motivation for different detection technologies based on first simulations and measurements.

Corresponding authors: J. Auffenberg[*1]

[1] *RWTH Aachen University, Aachen, Germany.*

The 34th International Cosmic Ray Conference,
30 July- 6 August, 2015
The Hague, The Netherlands

[*]Speaker.

1. Introduction

The IceCube observatory [1] consists of 5160 photomultipliers deployed in depths between 1450 m and 2450 m into the Antarctic ice cap (deep detector, see Figure 1). IceCube reconstructs the trajectory of charged leptons produced during high-energy neutrino interactions in the surrounding ice via the emitted Cherenkov light. Recently published results show that IceCube has

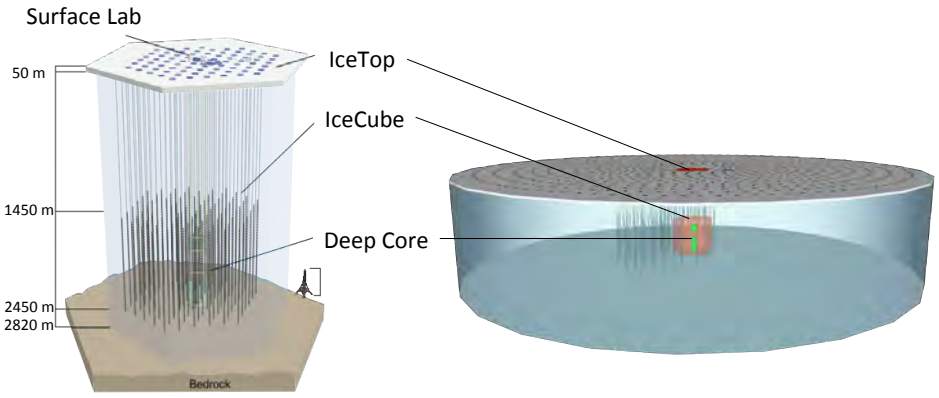

Figure 1: Artists view of IceCube and the IceCube-Gen2 detector with an extended surface array.

measured an astrophysical neutrino flux with high significance, however, no evidence for a point source has been found yet [2]. Above about 100 TeV neutrino primary energy, the measured diffuse flux dominates the background of cosmic-ray-induced neutrinos and muons. One main task for the next-generation detector, *IceCube-Gen2*, will be the detection and high-quality reconstruction of a sufficient number of neutrinos for astronomical observations and a measurement of their spectrum with high precision (see also [3]).

The main backgrounds for extraterrestrial neutrinos are cosmic-ray induced particles produced in the atmosphere. One way to suppress some of these backgrounds is to select particles coming from the northern hemisphere, as charged particles are absorbed by the Earth. Thus only neutrinos (both astrophysical and atmospheric) reach the detector. In the southern hemisphere, the cosmic-ray-induced muon background dominates the neutrinos detected in IceCube because high-energy muons penetrate the several km overburden of ice above the detector. However, the corresponding cosmic-ray-induced air showers can be detected with a dedicated air shower array at the surface [4]. Such a surface detector can be used to veto the cosmic-ray-induced muons reaching the deep detector and is to some extent able to suppress even the atmospheric neutrino background. In fact, IceTop, an array of instrumented ice tanks located above IceCube, is already used in several analyses to suppress the atmospheric background, thereby increasing the sensitivity of IceCube for astrophysical neutrinos in the down-going region [5, 6, 7]. Another well-established way to distinguish the cosmic-ray-induced background from astrophysical neutrinos is to use the outer optical modules of the deep detector as veto [8]. Figure 2 shows the zenith distribution vs the energy deposit of the events in the deep detector found with this technique in four years of IceCube data using such a veto [2]. The corresponding event selection has two main features.

First, it selects about 3.5 times more events with a dominating hadronic or electromagnetic cascade than events with a clear single muon track because most of the neutrino interactions do not produce elongated tracks. Second, IceCube does not detect any neutrinos with high light deposit in the up-going region (upper right corner of Figure 2), due to the neutrino cross section that grows with increasing energy. This shows that the detection of very high energy astrophysical neutrinos is limited to events that are down-going.

A veto at the surface of IceCube follows the idea to select starting events, but uses a surface detector to identify cosmic-ray-induced signals. As a result, one can also detect events that started in the volume between the deep detector and the surface array.

The advantages of detecting with a surface veto more high-energy astrophysical neutrinos containing a larger fraction of high-energy ν_μ-induced tracks are described in section 2. Here, we discuss different motivations for surface extensions that lead to different possible configurations. In addition, different technological approaches for a cosmic-ray veto on the surface are summarized in section 3.

2. Motivation for surface detectors as veto for cosmic rays for IceCube-Gen2

The idea for a surface veto is to rely on the construction of a hypothetical shower front based on the reconstruction of an event with the deep detector (see Figure 3). If one finds more than a certain number of hits in coincidence with the expected shower front in the surface detector, the event is vetoed as background for astrophysical neutrino detection.

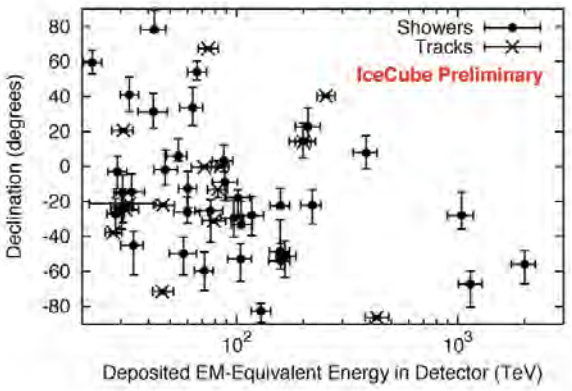

Figure 2: Zenith distribution vs. the energy deposit in the deep detector for the events found with the starting-event search after four years of data taking [2].

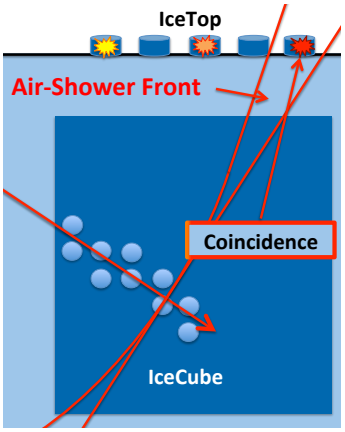

Figure 3: Schematic view of the IceTop veto strategy for the IceCube Observatory. If IceTop records hits consistent in time with a hypothetical shower front, the event is considered to be cosmic-ray-induced [9].

The general principle of such a surface veto is described in more detail in [9] with IceTop as an example. As mentioned in the introduction, IceCube-Gen2 extends the energy range of IceCube for the detection of astrophysical neutrinos and the identification of their sources [3]. In the following, the possible impact of a surface veto array on the measurement of different properties

of the astrophysical flux are discussed and estimated. Detailed simulations of surface veto arrays will quantify the impact on these measurements in the future.

2.1 Measurement of the properties of the diffuse spectrum

Depending on the still-uncertain details of the astrophysical flux, the detection of astrophysical neutrinos in different energy regions can be of particular interest. For very soft spectra, it can be interesting to focus on moderate energies of as low as a few TeV to measure possible features of the neutrino spectrum. For harder spectra, the high-energy neutrinos are interesting, to measure a possible cut-off or change of slope at PeV energies. In both cases, a larger number of astrophysical neutrinos is needed.

At energies above 100 TeV, neutrinos from the northern sky are more and more likely to be absorbed during propagation through the Earth. It is therefore crucial to detect high-energy neutrinos from the southern sky (down-going). Here, an extended surface veto can improve significantly the detection of uncontained ν_μ-induced muon tracks. Table 1 shows the number of up-going and down-going astrophysical ν_μ at energy thresholds of 1 TeV, 10 TeV, and 100 TeV neutrino energy. The numbers are based on Monte Carlo simulations. The injected flux was normalized to fit the observed astrophysical flux with 2 years of IceCube data [10]. The harder and steeper spectra account for the approximate uncertainty of the spectral index at the time. Up-going and horizontal ν_μ up to 5° above the horizon that interact in IceCube are not dominated by the background from muons that where produced in air showers. In the down-going region (0° - 85° declination) neutrino signatures in IceCube are several orders of magnitude fewer than penetrating muon tracks induced by cosmic rays. For example, for 100 TeV vertical astrophysical neutrinos the muon rate is about 5 orders of magnitude higher than the expected astrophysical ν_μ flux [7]. Here, an efficient surface veto detector would allow to obtain roughly the same number of ν_μ above 10 TeV neutrino primary energy from the down-going region as from the up-going region, and hence double the number of identifiable cosmic neutrinos almost independent from the spectral index. Due to the smaller observation region of $0° - 85°$ declination in the southern sky, the background from atmospheric neutrinos (ν_{Atmos} in table 1) is 30% lower. Also the atmospheric neutrino background is expected to be vetoed to some extent.

The total number of astrophysical ν_μ from the starting-event approach (Figure 2) and the number of astrophysical ν_μ from the southern sky after applying a surface veto can be compared. The starting event search sacrifices about 40% of the in-ice detector for astrophysical neutrino detection due to the in-ice veto approach. After applying a surface veto this is not necessary anymore for the southern sky. In addition the active volume, where an astrophysical neutrino is allowed to interact, gets enlarged by the surrounding ice, now covered by the surface veto. Thus, for vertical events we gain 1.5 km ice above the detector in addition to the 40% increase from removing the in-ice veto. Overall the volume for astrophysical ν_μ to interact and induce muon tracks increases by roughly a factor of 3.5 in the vertical direction. For the galactic center, a source candidate in the southern sky at 62° declination, the overall gain in volume is roughly a factor of 8 [11]. The expected increase of high-energy tracks induced by astrophysical ν_μ is similar and only slightly reduced due to absorption in the ice. These ν_μ induced tracks are the event type with the most accurate pointing [12].

	up-going			down-going		
	1 TeV	10 TeV	100 TeV	1 TeV	10 TeV	100 TeV
E^{-2}	110	44	11	80	44	18
$E^{-2.3}$	220	60	9	160	57	13
$E^{-2.7}$	740	110	7	590	100	10
ν_{Atmos}	15000	500	5	10500	350	5

Table 1: Number of astrophysical neutrinos expected from the northern and the southern sky above different energy thresholds in IceCube in one year. The estimated event numbers are based on Monte Carlo simulations. The normalization derives from the measured astrophysical flux. Up-going is defined to end 5° above the horizon, the region that is currently used in IceCube diffuse ν_μ analyses. The down-going region is defined from the vertical to 85° declination dominated by muons from air showers without a surface veto. ν_{Atmos} is the expected number of atmospheric neutrinos. No surface veto was applied to the ν_{Atmos}.

2.2 Identification of point sources

Coincident hits in IceTop are a well established parameter in IceCube point source analyses to increase the sensitivity in the very down-going region ($\theta < 25°$) [13]. In section 2.1 it was discussed that a surface veto could enable us to identify up to twice as many high-energy ν_μ-induced tracks compared to just the in-ice detector. They come with moderate energy resolution but sub-degree directional reconstruction [12]. The pointing of these highly significant neutrino events could be the key to identify sources of the astrophysical neutrino flux.

To first order the significance $\sigma = N_{\text{signal}}/\sqrt{N_{\text{signal}} + N_{\text{background}}}$ to identify a point source increases linearly with the number of signal events N_{signal} in case of background domination. The denominator can further be approximated to decrease with $\sqrt{N_{\text{background}}}$. The number of background events $N_{\text{background}}$ is proportional to ψ^2_{event}, were ψ_{event} is the angular uncertainty of the events. As a result, the significance of a point source search roughly increases linearly with the inverse of the angular uncertainty $\sigma \sim 1/\psi_{\text{event}}$. Both the reduction of the cosmic-ray-induced background by orders of magnitude in the southern sky and the detection of more high-energy well reconstructed events will help to identify point sources in the southern sky.

The detection of a large number of almost background-free astrophysical neutrinos with sub-degree pointing would enable us to produce a catalog of numerous sub-degree astrophysical neutrino directions. As due to absorption in the Earth most of the well-pointing high-energy events can not come from the northern hemisphere, such a catalog is particularly powerful for the southern sky. Assuming an isotropic distribution of sources in the sky, the total number of source candidates in the direction of the neutrino decreases again with the angular uncertainty $1/\psi^2_{\text{event}}$. Thus the sensitivity of our experiment increases roughly with $1/\psi$. This means that in first order one ν_μ with a more than ten times better pointing compared to ν_e contributes more than ten times more to the significance to a point source search. This catalog of sub-degree neutrino directions can be used for various types of multimessenger analyses. One example would be dedicated follow up searches with gamma ray telescopes in these directions with the goal to find correlating source types.

2.3 Detection of neutrinos with a cascade-like signature in IceCube

As already discussed in the introduction of this section, most of the neutrino signals in IceCube

are cascades. A large fraction of these cascades get produced by ν_e and ν_τ. Above about 1 PeV the separation of ν_e induced cascades and ν_{tau} induced signatures is possible [14]. In this case the ν_e and ν_{tau} signatures are particularly interesting for analyses of the neutrino flavor composition. Furthermore, for ν_τ with about 1 PeV energy, the majority of detected events will be down-going as otherwise they would be absorbed in the Earth. From adding a surface veto, even if only efficient at 1 PeV, most of the background without any containment cut would get removed. As a result one can expect the number of ν_τ to increase compared to the IceCube in-ice detector only. At 6.3 PeV the Glashow resonance, $\overline{\nu}_e + e^- \rightarrow W^-$ rapidly increases the interaction cross-section for $\overline{\nu}_e$. At these energies $\overline{\nu}_e$ could be of particular interest for an extended surface array as for ν_e the containment arguments are similar to those from ν_τ.

3. Hardware solutions for a surface veto

A detector consisting of a large number of detection modules has to be very efficient in different ways:

- Low energy threshold and high detection efficiency increase the sensitivity to the neutrino flux.
- The number of astrophysical neutrinos detected due to the veto increases linearly with the duty cycle of a surface veto detector (exposure).
- One gains additional detection volume with increasing zenith as discussed in section 2.1.
- The system should be easily deployable and operable at low cost.

3.1 Charged particle detection on the surface

The most obvious option for a surface veto are particle detectors that measure the Cherenkov or scintillation light produced by charged particles in an enclosed active volume like tanks or paddles. Results from first Monte Carlo simulations that are based on shower parameterizations underline the importance of the total collection area and sensitivity to both the electromagnetic and the muonic part of the shower [15]. First estimates of the veto efficiency of a particle detector on the surface, based on a geometry described in [11], show more than 99% veto efficiencies at ~ 20 PeV cosmic ray primary energy at $\cos(\theta) = 0.5$ (see Figure 4). To get higher veto efficiencies or lower passing rates for cosmic rays, a denser array could be considered (Figure 5). A detailed investigation of the event signatures and rates induced by cosmic-rays in the in-ice detector and subsequent comparison to those predicted from the astrophysical neutrino flux will show the potential of this geometry for astrophysical neutrino searches. Uncertainties due to particle density fluctuations in the air shower will need careful investigation.

3.2 Shower detection in the atmosphere

An alternative approach to cosmic ray shower particle detectors are detection systems that do not use a separated active volume as a calorimeter but the entire atmosphere above the detector. The radio emission of air showers in the atmosphere and the air Cherenkov emission or fluorescence light emission are examples of such signals.

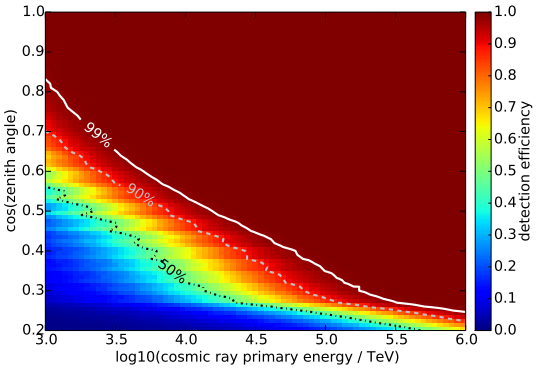

Figure 4: Veto efficiency as a function of zenith angle and cosmic ray primary energy for a surface detector as shown in Figure 1 right. The estimate is based on combined parameterizations of the lateral particle densities in air showers for muons and electrons.

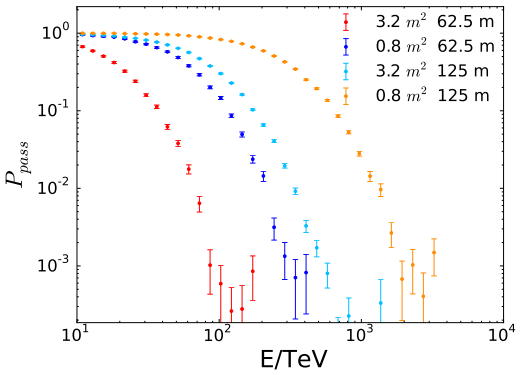

Figure 5: Passing fraction of quasi-vertical air showers ($< 25°$) from CORSIKA simulations. Array configurations that have a spacing of 62.5 m or 125 m and a scintillator surface area of 0.8 m^2 or 3.2 m^2 are shown.

The radio emission of air showers is a small signal in the regime of some MHz to several hundred MHz and can only be detected above the electromagnetic background at cosmic ray primary energies above 10 PeV. Therefore, this detection technique is currently not under further investigation for a veto detector [16].

The emission of Cherenkov light of cosmic-ray induced air showers is a rather strong signal compared to the night sky background. It can be detected down to much lower primary energies compared to other detection techniques. Assuming that an air Cherenkov detector has to work efficiently as a veto at about 100 TeV primary energy, only relatively small telescopes with apertures < 1 m are required. The detection efficiency for cosmic rays, and related, the density of detectors that are necessary for a veto detector, need to be investigated for air Cherenkov telescopes. Another challenge for air Cherenkov detectors at the South Pole are the environmental conditions. While extreme cold conditions can be simulated in laboratories, the influence of many other conditions of the Antarctic weather on the performance of such telescopes have to be investigated at the South Pole. For this purpose, a prototype telescope was developed that will be tested at the South Pole in the 2015/16 summer season [17]. The analyses of LIDAR observations at the South Pole show promising results concerning the estimated up-time of a telescope for air shower detection [18]. The data suggests an overall up-time as high as $20-25\%$ of the year might be possible (with $50\% \pm 10\%$ up-time during the austral winter).

4. Summary

We have shown that a surface detector optimized for vetoing muons that penetrate the in-ice detector of IceCube-Gen2 could significantly enhance the number of detectable astrophysical neutrinos. At energies above 10 TeV, a surface veto could enable IceCube-Gen2 to detect as many down-going astrophysical ν_μ as are currently detected as up-going. This ratio increases with the

energy threshold. Improvements in the measurement of different properties of the astrophysical neutrino flux were motivated. The detection of neutrinos with very good pointing on a very low background would increase the sensitivity of point source searches. Detectors based on particle detection in enclosed volumes are an obvious technology for surface air shower detectors. Alternative detection methods like air Cherenkov telescopes are under investigation. Detailed simulations will determine the impact of a surface detector to veto cosmic ray signals on the scientific goals of IceCube-Gen2.

References

[1] A. Achterberg et al. (IceCube Collaboration), Astropart. Phys., **26** (2006) 155-173, doi: 10.1016/j.astropartphys.2006.06.007.

[2] IceCube Coll., *Observation of Astrophysical Neutrinos in Four Years of IceCube Data*, PoS(ICRC2015)1081 these proceedings.

[3] IceCube Coll., *IceCube-Gen2 High Energy Array*, PoS(ICRC2015)1146 these proceedings.

[4] R. Abbasi et al. (IceCube Collaboration), Nucl. Inst. Meth. A, **700** (2013) 188-220, doi: 10.1016/j.nima.2012.10.067.

[5] IceCube Coll., *A search for extremely high energy neutrinos in 6 years of IceCube data*, PoS(ICRC2015)1064 these proceedings.

[6] IceCube Coll., *Results of neutrino point source searches with 2008-2014 IceCube data above 10 TeV*, PoS(ICRC2015)1047 these proceedings.

[7] IceCube Coll., *IceTop as Veto for IceCube*, PoS(ICRC2015)1086 these proceedings.

[8] S. Schönert, T. K. Gaisser, E. Resconi, and O. Schulz, Phys. Rev. D **79**, 043009 (2009), doi: 10.1103/PhysRevD.79.043009.

[9] IceCube Coll., *IceTop as a veto in astrophysical neutrino searches for IceCube*, paper 0373 ICRC 2013 proceedings, http://arxiv.org/pdf/1309.7010.pdf.

[10] M. G. Aartsen et. al. (IceCube Collaboration), Science **342** (2013), doi: 10.1126/science.1242856.

[11] IceCube Coll., *IceVeto: An extension of IceTop to veto horizontal air showers*, paper 0374 ICRC 2013 proceedings, http://arxiv.org/pdf/1309.7010.pdf.

[12] M. G. Aartsen et. al., JINST **9** (2014), P03009, doi: 10.1088/1748-0221/9/03/P03009.

[13] M. G. Aartsen et. al. (IceCube Collaboration), ApJ **779** 132 (2013), doi: 10.1088/0004-637X/779/2/132.

[14] IceCube Coll., *A Search for Astrophysical Tau Neutrinos in Three Years of IceCube Data*, PoS(ICRC2015)1071 these proceedings.

[15] IceCube Coll., *Simulation Studies for a Surface Veto Array to Identify Astrophysical Neutrinos at the South Pole*, PoS(ICRC2015)1070 these proceedings.

[16] J. Auffenberg et. al., *A radio air shower surface detector as an extension for IceCube and IceTop*, paper 0293 ICRC 2007 proceedings, http://arxiv.org/abs/0708.3331.

[17] J. Auffenberg et. al., *Design Study of an Air Cherenkov Telescope for Efficient Air-Shower Detection at 100 TeV at the South Pole on Top of IceCube*, PoS(ICRC2015)1155 these proceedings.

[18] S. Benzvi et. al., *An Estimate of the Live Time of Optical Measurements of Air Showers at the South Pole*, PoS(ICRC2015)568 these proceedings.

PROCEEDINGS OF SCIENCE

Status of the PINGU Detector

The IceCube-Gen2 Collaboration[1],

[1] *http://icecube.wisc.edu/collaboration/authors/icrc15_gen2*

E-mail: kclark@physics.utoronto.ca

The unknown neutrino mass ordering is one of the most interesting open questions in particle physics today, and is one of the focuses of the neutrino physics community. The measurement of a relatively large mixing angle between the first and third neutrino states makes it possible to consider several methods to measure the ordering. One such method uses atmospheric neutrinos with a large water Cerenkov detector to make the determination. A proposed expansion of the IceCube/DeepCore detector called PINGU is made up of additional strings of optical sensors (similar to those already deployed in the IceCube detector) which will be located in the ice at the centre of IceCube. The spacing between these sensors would be smaller than those of the existing DeepCore detector (both vertically and horizontally) and this increased density would lower the neutrino detection threshold substantially below 10 GeV. The physical nature of the detector as well as the methods used to make this measurement are presented.

Corresponding authors: Kenneth Clark*[1]

[1] *Department of Physics, 60 St. George Street, Toronto, ON, Canada, M5S 1A7*

The 34th International Cosmic Ray Conference,
30 July- 6 August, 2015
The Hague, The Netherlands

*Speaker.

1. Introduction

Neutrino oscillations have been detected in a wide variety of sources such as reactors, the atmosphere and the Sun [1]. The combination of the results from these diverse experiments presents a consistent model for neutrino oscillations. This is summarized by the PMNS matrix [2] in which the entries represent the probability that each mass eigenstate will be detected as a particular flavour eigenstate. Currently the differences in mass between the eigenstates is known, but the ordering is not. The two possibilities are the case in which the third mass eigenstate (ν_3) is the heaviest (the "normal" hierarchy) or that in which it is lightest (the "inverted" hierarchy). The distinction between these two situations is discernible using atmospheric neutrinos using an appropriate detector [3, 4].

The proposed PINGU detector adds optical sensors to the existing IceCube/DeepCore array in the South Pole ice, thereby leveraging the success of the established infrastructure. The IceCube detector consists of 86 strings each with 60 optical sensors deployed between depths of 1450 and 2450 m below the surface of the ice cap. Here, 78 strings are installed at an average horizontal spacing of 125 m with sensors at an average vertical spacing of 17 m. These 4680 optical sensors are augmented with an additional 8 strings deployed in the centre of the array with horizontal spacing ranging from 40 to 70 m and a vertical spacing of 7 m (called DeepCore) which lowers the energy threshold for neutrino detection from roughly 100 to 10 GeV [5]. The PINGU detector would further lower this threshold while increasing the sample size at all energies.

1.1 Neutrino Studies

The accepted framework describing neutrino oscillations has been described in detail elsewhere [1] and will only be summarized here. The existence of oscillations defines a probability that a neutrino traveling in one flavour eigenstate will interact as another eigenstate. In the simplified two neutrino scenario, a neutrino with energy E_ν having traveled a distance L in eigenstate α will interact as eigenstate β as shown in Equation 1.1.

$$P(\nu_\alpha \rightarrow \nu_\beta) = sin^2(2\theta)sin^2\left(\Delta m^2 \frac{L}{4E_\nu}\right) \tag{1.1}$$

It is clear from Equation 1.1 that in the two neutrino scenario, the oscillation probability depends on the ratio of the length traveled and the energy of the neutrino as well as the mixing angle between the two states. This relationship is the same in the more complex scenarios involving three (or more) flavours of neutrinos, and proves to be an ideal parameterization with which to characterize the oscillations. IceCube analyses presented here have assumed a three flavour scenario which introduces three mixing angles, two mass-squared differences and one complex phase to this equation.

2. IceCube/DeepCore

The IceCube/DeepCore detector has successfully investigated the neutrino oscillation parameters and has the goal of reducing the potential phase space available for these values. In particular, recent results [8] have examined the disappearance of atmospheric muon-type neutrinos as they

travel through the Earth. A sample of approximately three years of data with IceCube/DeepCore has shown that the neutrino oscillation parameters (in particular Δm^2_{32} and $sin^2\theta_{23}$) can be determined with an accuracy approaching that of dedicated oscillation experiments. The scale of the measured effect is shown in the left plot of Figure 1.

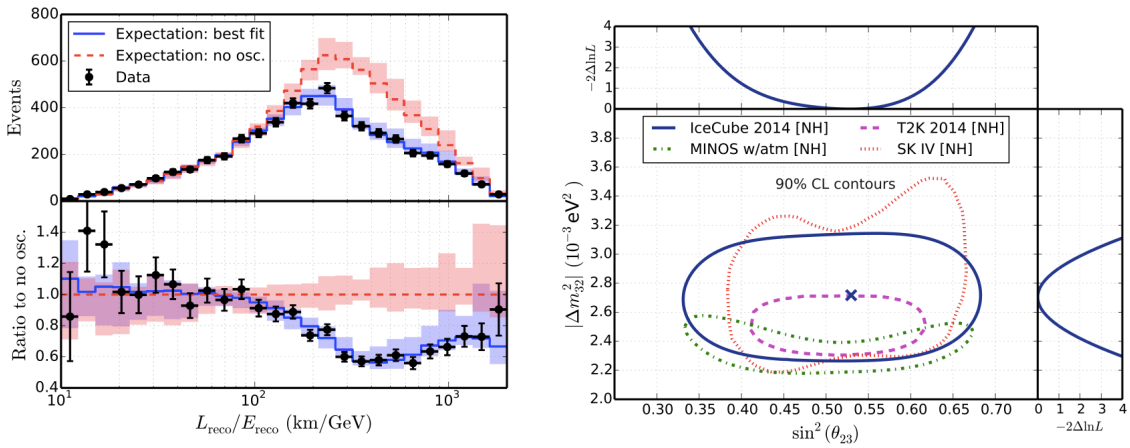

Figure 1: DeepCore analysis results from [8]. The left plot shows the reconstructed L/E distribution of events. The top portion of the left plot illustrates the best fit to the data as well as the expectation with no neutrino oscillations. The bottom portion of the left plot shows the ratio of the data and the best fit to the no-oscillation hypothesis. The bands shown are the estimated systematic uncertainties. The right plot shows the 90% confidence contours resulting from the best fit for $sin^2\theta_{23}$ and Δm^2_{32} compared to results from dedicated oscillation experiments. Shown above and to the right of the plot are the likelihood profiles of the parameters. In this plot it is assumed that the normal hierarchy is true.

As an additional test of the analysis framework, the analysis shows no significant deviation from the "no oscillation model" (shown in red in the left plot of Figure 1) in the low L/E region. Neutrinos in this region have a very short path length through the ice or are at very high energy, neither of which will show the effects of neutrino oscillations.

In order to determine the best fit values of the oscillation parameters, a maximum likelihood analysis is used which includes nuisance parameters accounting for the systematic uncertainties. The full three-flavour scenario for neutrino oscillations is used to determine the best fit values of θ_{23} and Δm^2_{32}. The 90% confidence contours for these parameters are shown in the right plot of Figure 1. As seen, the results from IceCube/DeepCore are now approaching levels of accuracy which were previously only attainable using dedicated oscillation experiments and indicate the potential of future measurements with a large-scale Cerenkov detector like PINGU.

3. PINGU

The PINGU detector will further lower the IceCube array energy threshold by adding another 40 strings with 96 DOMs per string. Following an extensive optimization process, the chosen geometry has a 22 m average horizontal spacing between strings and 3 m vertical spacing between modules. The new PINGU strings will be co-located with DeepCore extension at the bottom of the array in the centre of the IceCube strings, as shown in Figure 2. The effect of lowering the neutrino

detection energy threshold is shown in the "effective area" curve for the PINGU detector in Figure 3.

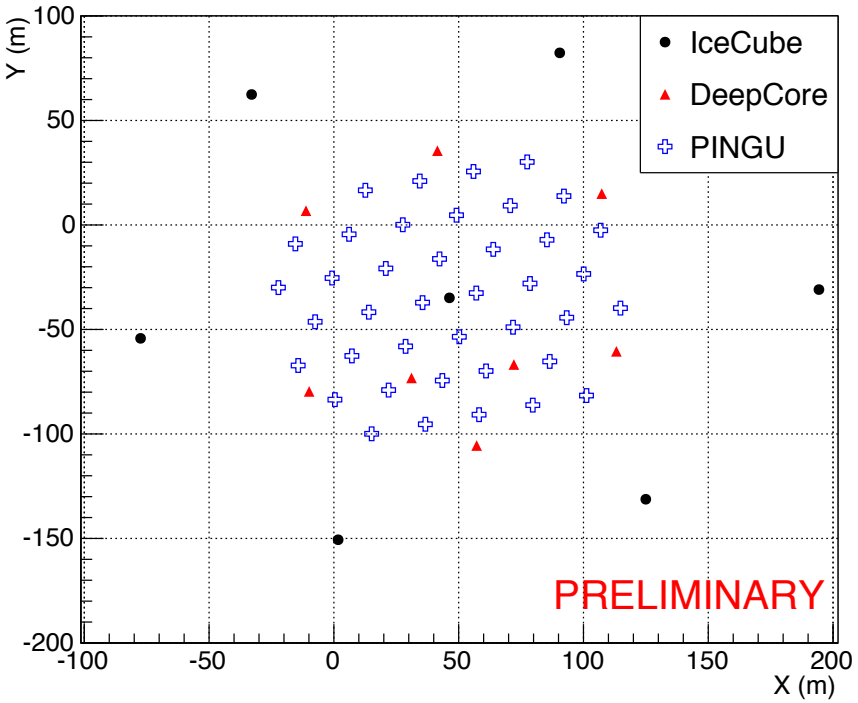

Figure 2: A top view of the optimized PINGU geometry showing the position of IceCube strings (black circles), DeepCore strings (red triangles) and planned PINGU strings (blue crosses) .

The positioning of the PINGU detector within the DeepCore fiducial volume allows the existing IceCube strings to be used to veto background muons that enter the PINGU volume. These incoming events, which produce light outside of the PINGU strings, will be removed from the signal event sample using tools which have been used successfully in the DeepCore analyses [5]. The additional PINGU DOMs also improve the reconstruction resolution by collecting more of the Cerenkov photons produced in each event. The mean resolution ($[E_{true} - E_{reco}]/E_{true}$) in the primary region of interest for PINGU (approximately 5 to 15 GeV) has been decreased to roughly 30% at 5 GeV and is better at higher energies. In addition, the angular resolution also improves with the detection of additional photons, which in turn improves the determination of the neutrino path length.

The effective area of the PINGU detector is obtained using simulated data. This calculated value represents the equivalent area in which all neutrinos incident on the Earth would be observed. Of particular note in these plots is the energy range over which the effective area extends. As shown, significant sensitivity to all neutrino flavours is maintained down to at least 5 GeV, with a sharp reduction at lower energies. It is this lowered energy limit (compared to the IceCube limit, on the order of 100 GeV, or the DeepCore limit, on the order of 10 GeV) which is of benefit to the planned

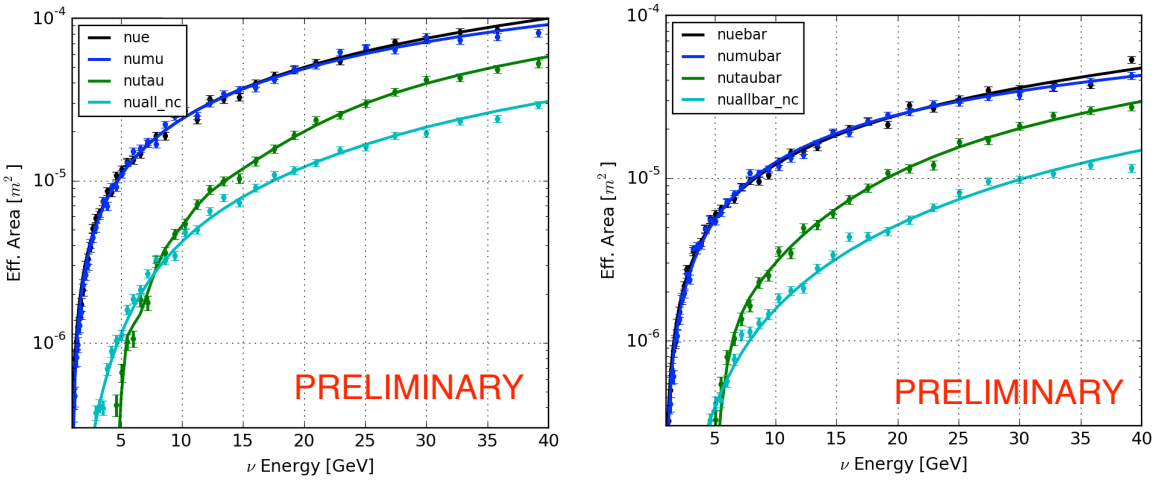

Figure 3: The effective area of the PINGU detector for all neutrino (antineutrino) flavours, left (right). In this plot, nue represents the area for electron-type neutrinos, numu represents muon-type neutrinos, nutau represents tau-type neutrinos, and nuall_nc represents neutral current neutrinos of all flavours.

future neutrino oscillation analyses.

4. PINGU Physics

4.1 Neutrino Mass Ordering

The primary goal of the PINGU detector is the determination of the neutrino mass ordering (hierarchy), an open question which has persisted for many years [1]. In the current status of the study of neutrino oscillations, many parameters are known, which aids in the determination of the ordering.

As neutrinos pass through the Earth, the flavour oscillations are described by the MSW effect [6], which results in a resonant enhancement of the probability of the $\nu_\mu \rightarrow \nu_e$ oscillation if the mass ordering is "normal" (ν_3 is heaviest) and $\bar{\nu}_\mu \rightarrow \bar{\nu}_e$ if the ordering is "inverted" (ν_3 is lightest). The increase in the oscillation probability is highly dependent on both the energy and the linear electron density along the path of the neutrino, a combination of the density profile of the Earth and the path length of the neutrino. The range of incoming zenith angles available to the PINGU detector therefore provides a wide range of oscillation probabilities.

In addition to the MSW effect, the neutrino oscillations also experience a parametric enhancement of their oscillations in specific circumstances [7]. This enhancement affects neutrinos passing through the mantle just outside of the outer core which have an energy of roughly 6 GeV. Parametric oscillation provides about one third of PINGU's sensitivity to the neutrino mass ordering.

These oscillation probability changes are dependent on the nature of the hierarchy and the neutrino (ν or $\bar{\nu}$) so that $P(\nu_\mu \rightarrow \nu_\mu)_{NH} = P(\bar{\nu}_\mu \rightarrow \bar{\nu}_\mu)_{IH}$. Since IceCube/DeepCore and PINGU are unable to distinguish between neutrinos and anti-neutrinos, the changes are visible only in the sum of these probabilities (e.g. $[P(\nu_\mu \rightarrow \nu_\mu)_{NH} + P(\bar{\nu}_\mu \rightarrow \bar{\nu}_\mu)_{NH}]$) which can be used to create a representative event sample for both "normal" and "inverted" hierarchy distributions. These can

then be subtracted to show the difference in the number of events expected, and separated into "track-like" ($\nu_\mu CC$) and "cascade-like" ($\nu_e, \nu_\tau\ CC, \nu_{all}\ NC$) events using the particle identification (PID) developed for use with the reconstructions used in PINGU. The results of these plots are shown in Figure 4.

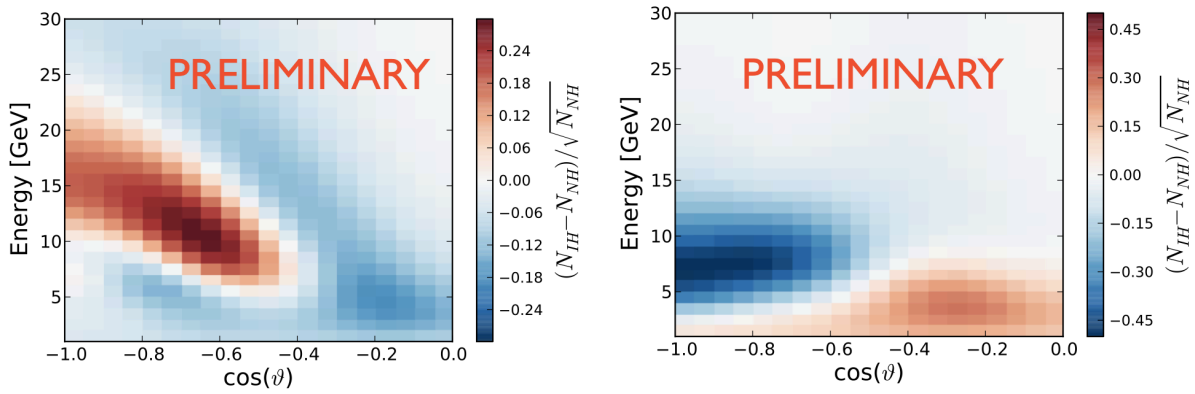

Figure 4: The scaled difference in the annual counts for the PINGU detector are shown for events identified as track-like (left) and cascade-like (right) during the reconstruction process.

The determination of the hierarchy then relies on the shape of the event distributions as shown in Figure 4. Refinements in the analysis have enhanced the sensitivity, while a more accurate noise model and a more complete set of systematic errors have partially offset this gain. The primary analysis method is now a likelihood ratio study which accounts for many of the predicted systematics, broadly separated into oscillation, flux and detector systematics. Figure 5 shows the results of extracting the neutrino mass ordering with PINGU with only statistical uncertainties (dashed lines) and with all systematics included (solid lines). As seen in Figure 5, the 3σ threshold in this analysis is reached with just over three years of data regardless of the hierarchy, although it will be slightly sooner if the true hierarchy is normal.

4.2 Neutrino Oscillation Parameters

In addition to determining the true value of the neutrino mass hierarchy, the neutrino oscillation parameters (and in particular the atmospheric parameters θ_{23} and Δm^2_{32}) can also be studied using the lowered energy threshold provided by the PINGU detector. The oscillation parameters can be extracted from the likelihood-based analysis discussed in the previous section. The preliminary expectations of this analysis are shown in Figure 6. The expected improved sensitivity to lower mass WIMPs in the PINGU detector is also shown.

4.3 Dark Matter

In addition to studying neutrinos and their oscillations, PINGU can also search for astrophysical sources which produce neutrinos and use them as messengers. Of particular interest to the physics community is the search for dark matter. The IceCube detector and the DeepCore extension have carried out these dark matter searches, producing world-leading results as shown in the right plot of Figure 6.

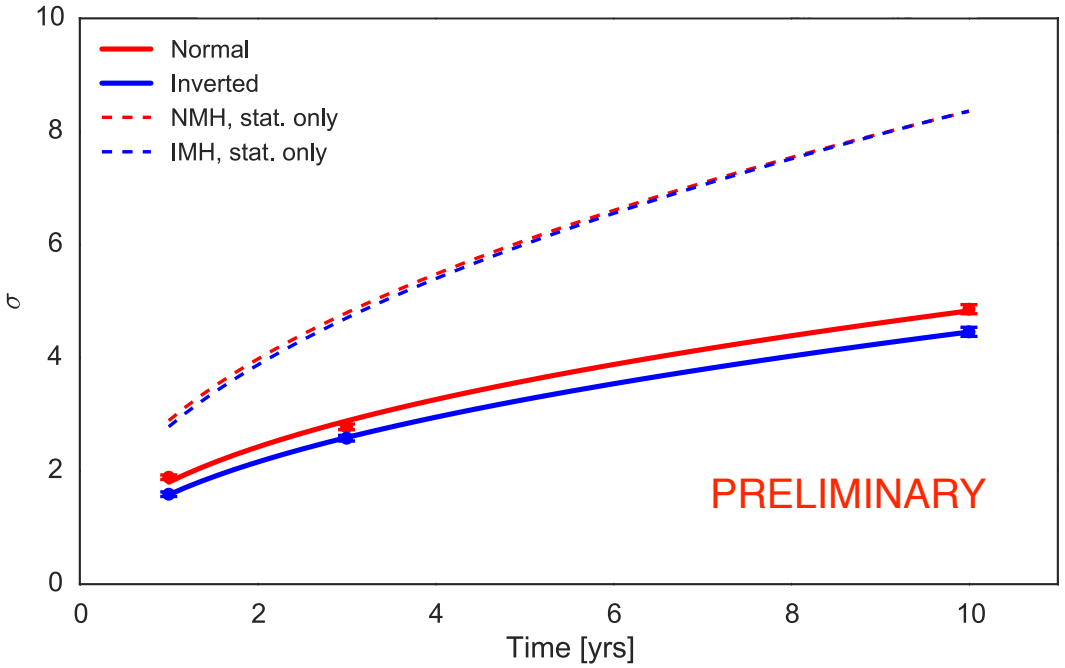

Figure 5: The evolution of the significance for determining the neutrino mass hierarchy with the PINGU detector shown by years of data taking.

The dark matter analysis has been carried out at several stages during construction of the IceCube/DeepCore array. The red curve in Figure 6 labelled IC79 represents the incomplete IceCube detector with only 79 strings, while the curve in black represents the results using the full PINGU detector (which includes the DeepCore extension). The blue bands indicate the range expected from anticipated improvements to the analysis methods.

The increased density of photodetectors in the ice will aid the results curve in two primary ways. The first is that the energy threshold of the detector will be lowered, making available more neutrinos at low energies. This lowering will change the sensitive phase space for the PINGU detector to include much lower energy events. The second way the results will be changed is that the reconstructions will be improved, as discussed previously. Improving the reconstruction for the dark matter analysis makes a significant difference, since the pointing accuracy of the detector can be used to distinguish signal from background, particularly for the analysis of solar WIMP annihilations.

5. Summary

The IceCube array, with its low energy extension, have shown that the execution of precision particle physics is achievable in the Antarctic ice at the South Pole. The planned PINGU sub-array holds the potential to further lower the neutrino detection energy threshold, making it possible to study the physics of the neutrino mass ordering and access low-mass dark matter. The optimization

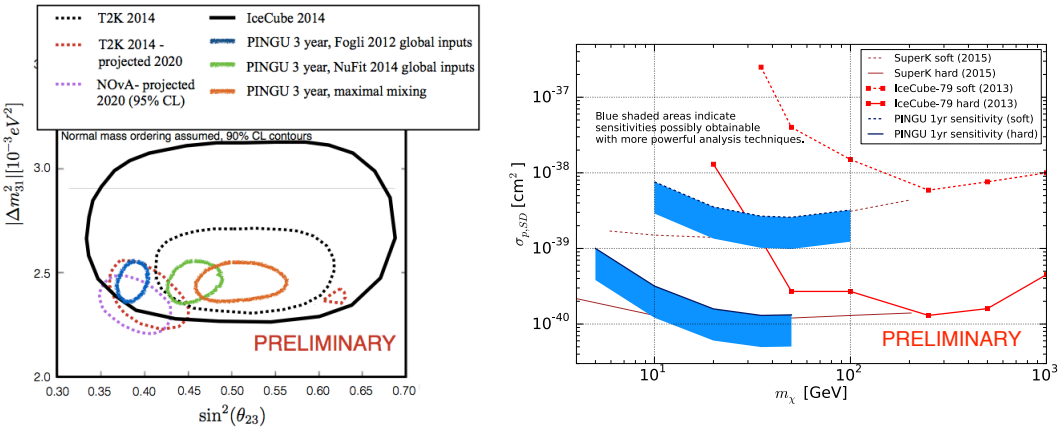

Figure 6: Additional physics results using the PINGU detector. The sensitivity to the oscillation parameters is shown in the right plot with the PINGU projected sensitivity. The left plot shows the dark matter exclusion limit results for SuperK, IceCube and the projected results for PINGU.

studies of PINGU are now nearing completion and the collaboration has started planning for the next stage of the project.

References

[1] J. Beringer et al, *Review of Particle Physics*, *Phys. Rev. D* **86** (2012) 010001

[2] Z. Maki, M. Nakagawa, and S. Sakata, *Remarks on the unified model of elementary particles*, *Prog. Theor. Phys.* **28** (1962) 870

[3] O. Mena, I. Mocioiu, and S. Razzaque, *Neutrino mass hierarchy extraction using atmospheric neutrinos in ice*,*Phys. Rev. D* **78** (2008) 093003

[4] E. Kh. Akhmedov, S. Razzaque, and A. Yu. Smirnov, *Mass hierarchy, 2-3 mixing and CP-phase with huge atmospheric neutrino detectors*,*Journal of High Energy Physics* **82** (2013)

[5] The IceCube/DeepCore Collaboration, *The design and performance of IceCube DeepCore*, *Astroparticle Physics* **35** (2012) 615

[6] L. Wolfenstein, *Neutrino Oscillations in Matter*, *Phys. Rev. D* **17** (1978) 2369; S. P. Mikheyev and A. Yu. Smirnov *Resonance enhancement of oscillations in matter and solar neutrino spectroscopy*, *Sov. J. Nucl. Phys.* **42** (1985) 913

[7] E. Kh. Akhmedov, *Parametric resonance of neutrino oscillations and passage of solar and atmospheric neutrinos through the Earth*, *Nuclear Physics B* **538** (1999) 25

[8] The IceCube/DeepCore Collaboration, *Determining neutrino oscillation parameters from atmospheric muon neutrino disappearance with three years of IceCube DeepCore data*, *Phys. Rev. D* **91** (2015) 072004